Title
Solar Radiation and Near-Earth Asteroids: Thermophysical Modeling and New Measurements of the Yarkovsky Effect

Author
Nugent, Carolyn Rosemary

Publication Date
2013

Peer reviewed|Thesis/dissertation

University of California
Los Angeles

Solar Radiation and Near-Earth Asteroids: Thermophysical Modeling and New Measurements of the Yarkovsky Effect

A dissertation submitted in partial satisfaction
of the requirements for the degree
Doctor of Philosophy in Geophysics and Space Physics

by

Carolyn Rosemary Nugent

2013

Abstract of the Dissertation

Solar Radiation and Near-Earth Asteroids: Thermophysical Modeling and New Measurements of the Yarkovsky Effect

by

Carolyn Rosemary Nugent

Doctor of Philosophy in Geophysics and Space Physics

University of California, Los Angeles, 2013

Professor Jean-Luc Margot, Chair

This dissertation examines the influence of solar radiation on near-Earth asteroids (NEAs); it investigates thermal properties and examines changes to orbits caused by the process of anisotropic re-radiation of sunlight called the Yarkovsky effect.

For the first portion of this dissertation, we used geometric albedos (p_V) and diameters derived from the Wide-Field Infrared Survey Explorer (WISE), as well as geometric albedos and diameters from the literature, to produce more accurate diurnal Yarkovsky drift predictions for 540 NEAs out of the current sample of $\sim$ 8800 known objects. These predictions are intended to assist observers, and should enable future Yarkovsky detections.

The second portion of this dissertation introduces a new method for detecting the Yarkovsky drift. We identified and quantified semi-major axis drifts in NEAs by performing orbital fits to optical and radar astrometry of all numbered NEAs. We discuss on a subset of 54 NEAs that exhibit some of the most reliable and strongest drift rates. Our selection criteria include a *Yarkovsky sensitivity* metric that quantifies the detectability of semi-major axis drift in any given data set, a signal-to-noise metric, and orbital coverage requirements. In 42 cases, the observed drifts ($\sim 10^{-3}$ AU/Myr) agree well with numerical estimates of Yarkovsky drifts. This agreement suggests that the Yarkovsky effect is the dominant non-gravitational process

affecting these orbits, and allows us to derive constraints on asteroid physical properties. We define the *Yarkovsky efficiency* f_Y as the ratio of the change in orbital energy to incident solar radiation energy, and we find that typical Yarkovsky efficiencies are $\sim 10^{-5}$.

The final portion of this dissertation describes the development of and results from a detailed thermal model of potentially hazardous asteroid (29075) 1950 DA. This model combines radar-derived shape models of the object and fourteen 12 μm observations by the WISE spacecraft. The observations were taken at a single phase angle, and this thermophysical model constrains K to less than 0.01 W m^{-1} K^{-1}. By running Monte Carlo simulations that varied diameter and thermal conductivity over a reasonable range of values, thermal inertia was constrained to be less than $\Gamma = 110$ J m^{-2} s$^{-0.5}$ K^{-1}. This value is consistent with other measurements of thermal conductivity and inertia for near-Earth asteroids.

This dissertation represents a new and original contribution to the study of NEAs. We increased the number of published predicted Yarkovsky drifts by an order of magnitude, increased the number of Yarkovsky detections by a factor of four, and developed new code to derive thermophysical parameters of asteroids that in turn drive their susceptibility to the Yarkovsky drift.

The dissertation of Carolyn Rosemary Nugent is approved.

Edward L. Wright

Christopher T. Russell

Kevin D. McKeegan

Amy K. Mainzer

Jean-Luc Margot, Committee Chair

University of California, Los Angeles

2013

Thanks.

Table of Contents

List of Figures

List of Tables

Vita

2003-2005	Researcher, Tom Solomon Lab, Bucknell University.
2004-2006	Researcher, Eric Weeks Lab, Emory University
2006	B.S. Physics, Bucknell University
2008	AAAS Mass Media Fellow, The Oregonian
2009	M.S. Geophysics and Space Physics, UCLA
2011	Collegium of University Teaching Fellows, UCLA

Publications and Presentations

Nugent, C. R., Quarles, W., and Solomon, T., (2003). Chaotic Advection and Reaction-Advection-Diffusion Systems: Chemical Pattern Formation in a Blinking Vortex Flow. *Division of Fluid Dynamics of the American Physical Society* #AM.004

Nugent, C. R., Quarles, W. M., and Solomon, T. H. (2004). Experimental Studies of Pattern Formation in a Reaction-Advection-Diffusion System. *Physical Review Letters* 93, 218301

Nugent. C. R., Paoletti, M., and Solomon, T., (2005). Reaction Patterns in a Blinking Vortex Flow. *Division of Fluid Dynamics of the American Physical Society*, #AH.00012

Nugent, C. R., Patel, H., Saldana, J., and Weeks, E. R., (2006). Observed Effects of Confinement on Colloidal Glasses. *American Physical Society March Meeting*, #G34.000007

Paoletti, M. S., Nugent C. R., and Solomon, T. H. (2006). Synchronization of Oscillating Reactions in an Extended Fluid System. *Physical Review Letters* 96, 124101

Nugent, C. R., Edmond, K. V., Patel, H. N., Weeks, E. R. (2007). Colloidal Glass Transition Observed in Confinement. *Physical Review Letters* 99, 025702

Nugent, C. R., Spilker, L. J., Edgington, S. G., Russell, C. T., Pilorz, S. H., Altobelli, N., and Gutipati, M. (2007). Investigating the Composition of Saturn's Rings Using Cassini CIRS Data. *American Geophysical Union, Fall Meeting*, #P43B-1293

Nugent, C. R., Spilker, L. J., Edgington, S. G., Pilorz, S., Leyrat, C., Altobelli, N., Russell, C. T., (2008). *American Geophysical Union, Fall Meeting*, #P13A-1299

Edmond, K. V., Nugent C. R., and Weeks, E. R. (2010). Local influence of boundary conditions on a confined supercooled colloidal liquid. *Europhysics Journal, Special Topics* 189, 83-93

Nugent, C. R., Margot, J. L., Russell, C. T., Nolan, M. C., Magri, C., Giorgini, J. D. (2010). SHAPE Modeling of (4) Vesta for Dawn Mission Support and SHAPE Inversion Validation. *41st Lunar and Planetary Science Conference*, #1533

Edmond, K. V, Nugent, C. R., and Weeks, E. R. (2012). Influence of confinement on dynamical heterogeneities in dense colloidal samples. *Physical Review Letters E* 85, 041401

Nugent, C. R., Margot, J. L. Chesley S. R., and Vokrouhlický, D., (2012). Detection of

Semi-Major Axis Drifts in 54 Near-Earth Asteroids: New Measurements of the Yarkovsky Effect. *The Astronomical Journal* 144, 60

Nugent, C. R., Mainzer, A, Masiero, J., Grav, T. and Bauer, J., (2012). The Yarkovsky Drift's Influence on NEAs: Trends and Predictions with NEOWISE Measurements. *The Astronomical Journal*, 144, 75

Grav, T., Mainzer, A., Bauer, J., Masiero, J. and Nugent, C. R., (2012). WISE/NEOWISE Observations of the Jovian Trojan Population: Taxonomy. *The Astrophysical Journal*, (Accepted)

Mainzer, A., Grav, T., Bauer, J. McMillan, R. S., Giorgini, J., Spahr, T., Cutri, R. M., Tholen, D. J., Jedicke, R., Walker R., Wright, E., and Nugent, C. R. (2012). Characterizing Subpopulations within the Near Earth Objects with NEOWISE: Preliminary Results. *The Astrophysical Journal*, 752, 110.

Nugent, C. R., Margot, J. L., Chesley, S. R., and Vokrouhlický, D., (2012). Detection of Semi-Major Axis Drifts in 55 Near-Earth Asteroids. *American Astronomical Society, DDA meeting #43*, #7.03

Nugent, C. R., Mainzer, A., Masiero, J., Grav, T., Bauer, J. (2012). The Yarkovsky Drift's Influence on NEAs: Trends and Predictions with NEOWISE Measurements. *Division of Planetary Sciences Annual Meeting*, #218.10

CHAPTER 1

Introduction

Near-Earth asteroids (NEAs) are of interest to a wide range of individuals. The general population finds them compelling, due to the potential risk of Earth impact (Harris, 2008). They are also of interest to meteoriticists, as spectral evidence indicates NEAs are likely the source of some meteorites (Burbine et al., 2002). NEAs' proximity to Earth makes them attractive mission targets (Farquhar et al., 2002), and a current exploration focus of NASA. NEAs have also altered the course of biological evolution on Earth (Alvarez et al., 1980; Hildebrand et al., 1991). Furthermore, as remnants from the formation of the protoplanetary nebula, asteroids recorded the history of our solar system and are of interest to astronomers who seek to understand how the solar system evolved (Morbidelli et al., 2002, 2005). This dissertation focuses on the relationship between solar radiation and these interesting objects. Solar radiation incident on these bodies causes temperature variations across the surface, which can then power a small propulsive force known as the Yarkovsky effect.

At first glance, the notion that photons can significantly alter the orbits of asteroids may seem improbable. Although there are several radiation forces that act on asteroids, the Yarkovsky effect is the largest by far. This effect describes the small acceleration that is imparted to an asteroid when its spin causes its maximum thermal emission to be in a different direction than the maximum incident radiation from the sun.

Studies of the Yarkovsky effect have led to significant advances in our knowledge of asteroid dynamics. It has illuminated how main belt asteroids are transported into near-Earth space (Bottke et al., 2002b), and sheds light on the structure of asteroid families (Bottke et al., 2006). The Yarkovsky effect has a significant influence on the orbits of NEAs, and

it must be properly accounted for to make the most accurate trajectory predictions, including those of potentially hazardous asteroids (Giorgini et al., 2002; Chesley, 2006; Giorgini et al., 2008; Milani et al., 2009). As the strength of the Yarkovsky effect depends on physical properties such as density, thermal conductivity, and heat capacity, a measurement of Yarkovsky-induced acceleration can shed light on these hard-to-measure properties (Chesley et al., 2003). Finally, studies that employ the orbits of asteroids to measure quantities such as the oblateness of the Sun, or that test general relativity require careful accounting of the Yarkovsky drift (Margot & Giorgini, 2009a).

This dissertation presents Yarkovsky drift predictions as well as a novel technique for measuring the Yarkovsky drift. This new technique allowed for 42 Yarkovsky drift detections, increasing the number of measurements of this force by an order of magnitude. Additionally, the Yarkovsky predictions given in this dissertation highlight those NEAs likely to have high drifts, helping the observing community pinpoint interesting objects to observe. Finally, in this dissertation we explore the surface thermal environment that powers the Yarkovsky effect by combining space-based infrared observations of the NEA (29075) 1950 DA with a radar-derived shape model of that object. This represents one of the first times that infrared observations have been combined with such detailed shape models. The constraints placed upon the NEA's thermophysical parameters have allowed us to derive a more accurate prediction of the degree to which the Yarkovsky drift would influence its orbit (and other NEAs like it for which thermophysical properties can be determined).

1.1 Observational Data

Since the discovery of (1) Ceres by Giuseppe Piazzi in 1801, asteroids have been a highly observed class of objects. The initial trickle of discoveries became a flood in the early 19th century with the advent of photography. Whereas between 1871 and 1890 an average of 7 to 12 asteroids were discovered worldwide each year, a single astronomer, Joel H. Metcalf, was able to use pioneering photographic techniques to discover 41 between 1905 and 1914

(Peebles, 2000). In fact, asteroid observations became so commonplace that they often interfered with other observations, leading Weiss of Vienna to dub them "those vermin of the sky" (Seares, 1930). Even dedicated asteroid observers recognized the high computational expense associated with each discovery. In 1912 Metcalf commented, "Formerly, the discovery of a new member of the solar system was applauded as a contribution to knowledge. Lately it has been considered almost a crime." (Peebles, 2000)

World War II virtually extinguished asteroid research for nearly three decades, but by the late 1960's there was a resurgence of interest. Charles Kowal recalled that during this time, "...young astronomers wanted to learn about the asteroids (perhaps to the chagrin of their professors)...Most of all, they learned that the asteroids were quite exciting!" (Peebles, 2000).

The 1980 association of an asteroid impact with the Cretaceous-Tertiary (dinosaur) extinction event brought attention to the threat posed by asteroids (Alvarez et al., 1980). This was substantiated by the discovery of the 180 km diameter Chicxulub Crater in the Yucatán Peninsula, which is thought to be the site of the impact described by Alvarez et al. (1980).

Interest in small bodies as impactors was renewed when comet Shoemaker-Levy 9 impacted Jupiter in 1991 (Chapman, 1993; Levy et al., 1995). This represented the first time a major impact event could be witnessed by astronomers, and renewed interest in sky surveys that could identify possible impact threats to Earth. Such surveys include PanSTARRS, the Catalina Sky Survey, Spacewatch, the Near-Earth Asteroid Tracking Program, and the Lincoln Near Earth Asteroid Research Program (Larson, 2007; McMillan, 2007; Pravdo et al., 1999; Stokes et al., 2000).

1.1.1 Ground-based Telescopes

A large portion of current asteroid knowledge derives from earth-based optical and radar observations. Earth-based optical astronomy can be relatively low-cost and can cover large areas of sky. Effective computer algorithms can sift through large volumes of data, allowing

for several thousand asteroids to be observed each night (Jedicke et al., 2002; Larson, 2007; McMillan, 2007; Pravdo et al., 1999; Stokes et al., 2000; Kubica et al., 2007; Kaiser, 2004). Unfortunately, optical astronomy is blind to the portion of the sky that is close to the sun, and dependent on good weather.

Whereas optical astronomy passively collects light from the sky, radar astronomy actively emits a strong beam of radio waves at a target and collects the reflected return. The reliance on radio wavelengths results in radar astronomy being immune to both bad weather and daylight. However, radar astronomy requires large amounts of power, and only one object (or multiple system) can be observed at a time. Observing is limited to the 2-arcminute field of view of Arecibo Observatory (Gordon, 1964) or the NASA Deep Space Network 70 m antenna located in Goldstone, California (Renzetti et al., 1988), the world's only telescopes equipped to make these measurements.

The object also must be large enough, or close enough, to generate a detectable reflected signal. Emitted power from a telescope drops off as $\frac{1}{r^2}$, where r is the distance between the telescope and the object. A portion of the emitted radiation is reflected from the object, and again decreases in power as $\frac{1}{r^2}$. The net result is that the reflected power received is $\frac{1}{r^4}$ smaller than the power transmitted. Radar, then, can only view small objects if they are close to earth.

1.1.2 Space Telescopes and the WISE mission

Space-based telescopes offer several advantages over ground-based telescopes. Clouds and other atmospheric factors that can compromise observations are eliminated, and telescopes can be placed in orbits other than the Earth's, allowing for observing geometries that cannot be duplicated on the ground.

A position outside the Earth's atmosphere offers a particular advantage to infrared telescopes, as the warm atmosphere can add noise to infrared observations taken on the ground. This dissertation employs data gathered by the WISE spacecraft, an infrared telescope

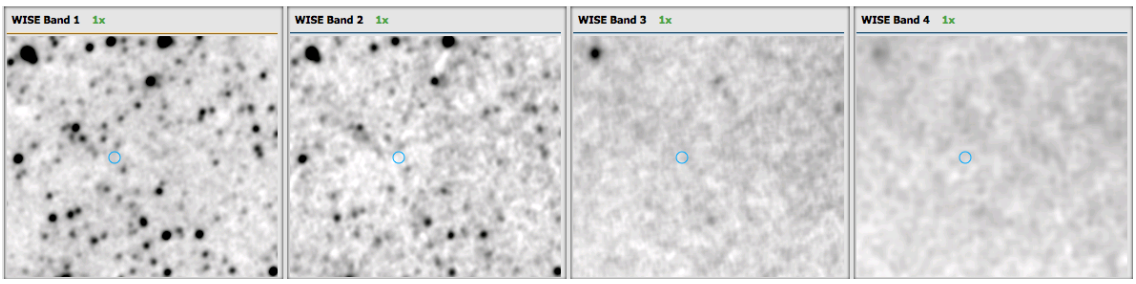

Figure 1.1 Co-added images from the WISE spacecraft. These images are stacked, so inertially stable (on the timescale of the observations) sources (like stars) are apparent, while moving objects (such as NEA 1950 DA, within blue circle) are not visible. Stars (dark objects) are highly visible in bands 1 and 2 (3.4 and 4.6 μm), but are largely absent in bands 3 and 4 (12 and 22 μm). This illustrates one of the advantages of surveying asteroids in infrared wavelengths. Image from the NASA/IPAC Infrared Science Archive WISE IRSA Catalog.

launched into space on December 14th, 2009.

Over the course of its mission, the WISE spacecraft observed over 158,000 minor planets using four infrared wavelength bands (3.4, 4.6, 12 and 22 μm) (Wright et al., 2010; Mainzer et al., 2011a). The data produced by this spacecraft are ideal for studying minor planets, and the enhancements to data processing that allowed for asteroid data to be extracted is collectively known as NEOWISE.

One advantage of this dataset was WISE's sun-synchronous, polar orbit around the Earth. This surveyed all areas of the sky, producing a dataset that was essentially equally sensitive to asteroids with low and high inclination (Mainzer et al., 2011b). The four infrared wavelengths were observed simultaneously using beam splitters, eliminating uncertainty in the time between measurements in the different bands. Therefore, there is no uncertainty in magnitude introduced from potential changing projected area between the different band measurements.

Additionally, infrared observations offer special advantages for asteroid observations. First, the dark, low albedo objects that are dim and difficult to observe in optical wavelengths glow bright in the infrared. Second, hot, bright stars that can obscure observations in the visual wavelengths are dim in infrared wavelengths. The density of astrophysical

background sources such as stars and galaxies is approximately a factor of 100 lower at thermal infrared wavelengths than at visible to near-infrared wavelengths (Figure 1.1). Finally, the combination of optical observations and thermal infrared observations can break the degeneracy between albedo and size, allowing for diameter measurements. Accordingly, the NEOWISE dataset yielded a catalog of effective spherical diameters accurate to within $\sim \pm 10\%$ and albedos accurate to within $\pm 25\%$ of their values (e.g. an albedo of 0.10 can be determined to within 0.02, Mainzer et al. (2011c)) using the Near-Earth Asteroid Thermal Model (NEATM) developed by Harris (1998).

On average, the spacecraft observed each asteroid between 10-12 times, spanning a ~ 36 hour period. In addition, WISE observed thousands of asteroids over two epochs separated by months, providing some additional information on rotational state. An example of a NEOWISE image is given in Figure 1.2.

Detailed documentation of the NEOWISE data extraction process can be found in the WISE All-Sky Release Explanatory Supplement (Cutri et al., 2012). An overview of this process is given here. Solar System objects were detected in WISE scan data by the WISE Moving Object Pipeline System (WMOPS), which was modeled after the Pan-STARRS Moving Object Pipeline System. This system was designed to quickly detect objects to allow for later follow-up by ground based observers, and therefore reported candidate detections within a maximum 10 days after their initial detection on board the spacecraft (though usually within a few days).

WMOPS worked to link together moving targets with a signal to noise ratio (SNR) above 4σ. These detections were identified by the WPRO routine, which identified the band with the brightest detection for a source, then searched the other three bands for detections at that location. These detections were centered within a 50-70 arcsecond annulus, and a series of point-spread functions were fit to the brightness profile until a best fit was found. Broadly, SNR is the ratio of the brightness of the object relative to the noise; for bright sources detected in band W3, the dominant source of noise arises from the zodiacal background.

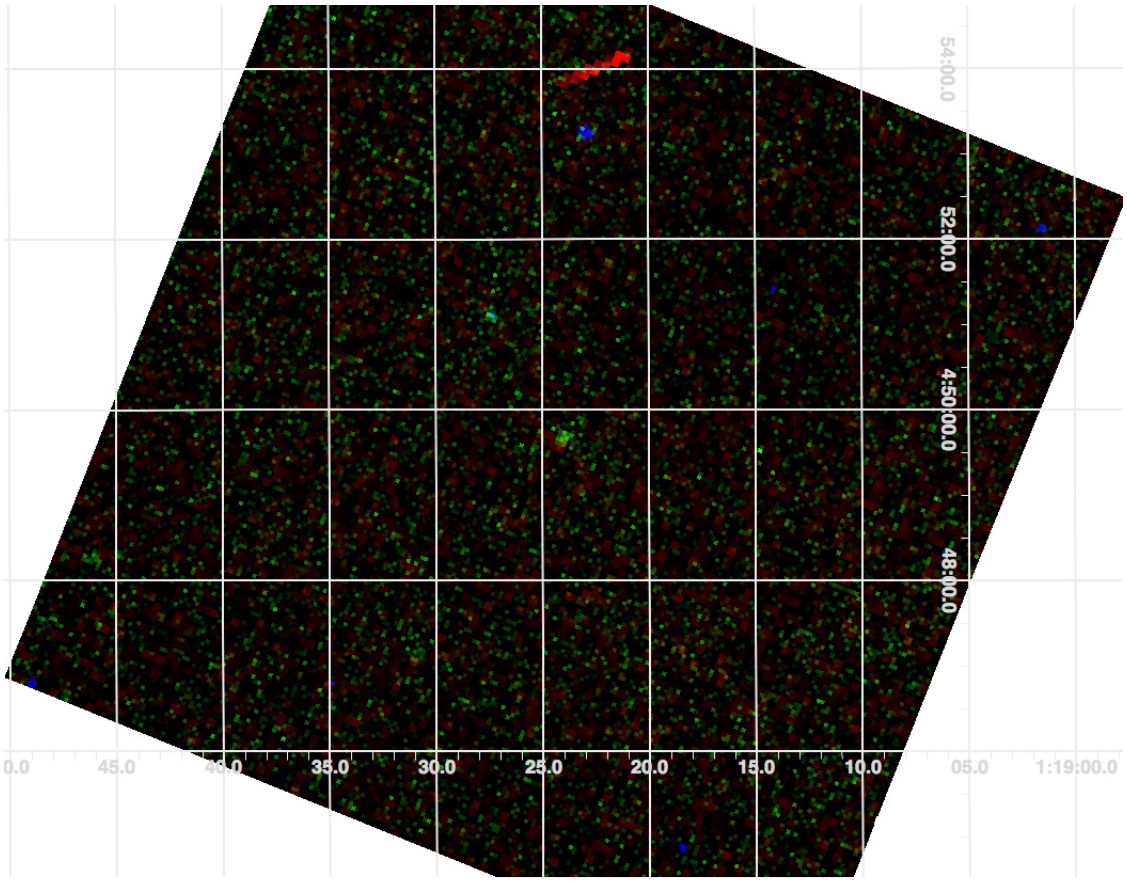

Figure 1.2 Overlay of 3 bands of WISE observations: W2 (blue), W3 (green), and W4 (red). Horizontal axis is R.A., vertical axis Dec. Visible in the center is 1950 DA, an asteroid that is thermophysically modeled in this dissertation. Note that this object was most strongly detected in band W3 (green). Also visible are a few stars in W2 (blue) and a cosmic ray (red streak, top).

1.2 Orbit determination software

It wasn't long after the discovery of Ceres that mathematicians devoted themselves to deriving orbital elements from astrometric observations. Positions of an object are measured in degrees of Right Ascension (RA) and Declination (Dec) by comparing the relative position of the object to several reference stars, which are presumed to have well-known positions. The accuracy of reference star positions varies across different star catalogs, or collections of reference star locations. That issue aside, typical astrometric uncertainties for asteroid measurements from modern-day observers are usually in the range of 0.2 and 1.0 arcseconds

(one arcsecond is 60^{-2} of a degree) (Ostro & Giorgini, 2003), and are limited to measuring the object's position in the plane of the sky.

Radar astrometry provides a measurement of range (distance from observer) and velocity of an object orthogonal to the plane of the sky. Range is determined by measuring the time between when a signal is emitted and when its reflected echo is returned. Velocity of the object relative to the observer can be determined from the reflected signal's Doppler shift. Both can be measured to high precision; at best, uncertainties in range can be on the order of 10 meters, and uncertainties in velocity can be on the order of 1 mm s^{-1}. This high precision measurement can vastly improve orbit determinations; on average, predictions that incorporate radar data have pointing errors 310 times smaller than predictions that only employ optical observations (Ostro & Giorgini, 2003).

However, the accuracy of an optical observation depends strongly on the reference star catalog used to identify an asteroid's position. Chesley et al. (2010) identified systematic biases in the commonly used United States Naval Observatory (USNO) star catalog, versions A1.0, A2.0, and B1.0, but found the UCAC (USNO CDD Astrograph Catalog) and the Tycho catalogs to be free of biases. Using this information, Chesley et al. were able to produce an algorithm that can remove star catalog biases from large portions of astrometry stored by the Minor Planet Center, a worldwide clearinghouse of small body observations (http://www.minorplanetcenter.net/). This algorithm was applied to the astrometric data used in this dissertation.

A number of groups have incorporated orbit determination algorithms into well-tested software packages, some of which are publicly available. Research involving asteroid orbits generally employs either the JPL Ephemeris Service (the engine behind the online Horizons service at http://ssd.jpl.nasa.gov/?horizons), or the OrbFit software package, which is developed and maintained by Andrea Milani and the OrbFit consortium and can be freely downloaded (http://newton.dm.unipi.it/). OrbFit is also the engine behind the NEODys and AstDys websites (Chesley & Milani, 1999). This dissertation employs the OrbFit software.

1.3 Radiation effects

The study of radiation forces on asteroid orbits has recently transformed from a theoretical field to an experimental one, with detections of the Yarkovsky effect (Chesley et al., 2003; Vokrouhlický et al., 2008; Nugent et al., 2012a). Although not the only radiation force that acts on asteroid orbits, the Yarkovsky effect is believed to be significantly and consistently larger than the Poynting-Robertson and albedo effects (Vokrouhlický et al., 2001) for sizes of asteroids in this study, and therefore the only one considered here.

Theoretical roots of the Yarkovsky effect stretch back to the beginning of the 20th century to a pamphlet written by Ivan Osipovich Yarkovsky. At the time, his idea was largely ignored. It might have been lost to science if not for the exceptional memory of Ernst J. Öpik, who recalled the work in a 1951 paper (Bottke et al., 2006).

The effect that Yarkovsky first described is today termed the diurnal Yarkovsky effect, to distinguish it from the seasonal Yarkovsky effect, which will be described later. The diurnal effect is related to a phenomenon familiar to anyone who has been outside on a hot summer's day. Although the Earth receives the most radiation when sun is directly overhead, the hottest part of the day is felt several hours later. The thermal inertia of the surrounding ground and air is responsible for this delay between the time of maximum incoming radiation and the time of maximum temperature. As the day progresses, the ground and air lose thermal energy via infrared radiation and other processes, cooling the area.

A similar process occurs on asteroids and spacecraft. A given surface point on those objects observes maximum incident radiation at local noon, but thermal inertia causes the time of maximum emitted radiation (usually in the infrared wavelengths) to occur some time later. Each arriving and departing photon has an associated momentum $p = E/c$, where E is the photon's energy and c is the speed of light. Since the body is rotating, the incident radiation is emitted in a different direction than the later emitted radiation, and the body experiences a very small net acceleration.

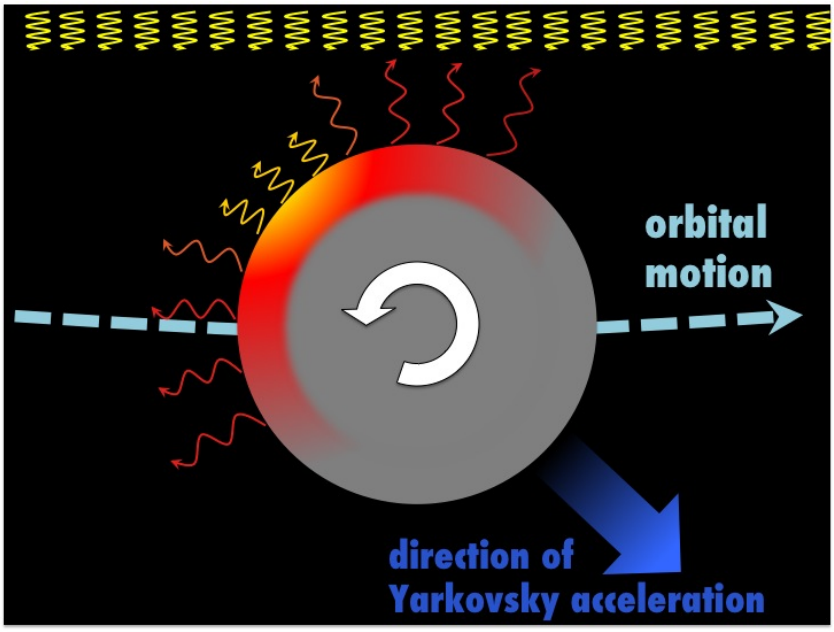

Figure 1.3 Illustration of the diurnal component of the Yarkovsky effect. A cross-section of a prograde rotating asteroid shows maximum emitted radiation emitting at a different surface location than maximum incident radiation. The Yarkovsky acceleration is opposite the direction of maximum emitted radiation, and has a component in the direction of the body's orbital motion.

If the body has a prograde spin, the net acceleration has a component aligned with the motion of the body's orbit, nudging the body away from the sun. Similarly, a body with a retrograde spin will feel an acceleration with a component antialigned with its velocity, shifting it towards the sun (see Figure 1.3). For example, the "Pioneer Anomaly", a small acceleration of spacecraft Pioneer 10 and 11 towards the sun, was recently attributed to anisotropic heat radiation (Turyshev et al., 2011).

The seasonal Yarkovsky effect was discovered thanks to the LAGEOS I satellite (Bottke et al., 2006), a brass sphere covered with retro-reflectors. LAGEOS I is an orbiting laser reflector, facilitating highly accurate distance measurements between stations on Earth. The high accuracy of this technique also allowed for the satellite's orbit to be precisely measured, leading to the discovery that its orbit was decaying by 1.1 mm/day (Rubincam, 1995).

Rubincam (1995) discovered the cause of the decay, and termed it "Yarkovsky thermal

drag". Later the term "seasonal effect" was adopted, referring to the relevant time scale of one orbit. In this case, it is the object's northern and southern hemispheres that experience the delay between maximal incident radiation and emitted radiation.

It is important to note that both the seasonal and diurnal Yarkovsky "effects" are, in fact, two end cases of the same phenomena. The diurnal Yarkovsky effect is strongest when the body's obliquity (the angle between the spin axis and the orbit plane) is 180° or 0° (when the seasonal Yarkovsky effect has no impact), and has no impact when the obliquity is 90° (when the seasonal Yarkovsky effect is the strongest.) At any given time, the Yarkovsky acceleration on an object will be a combination of both the seasonal and diurnal effects. Vokrouhlický et al. (2000) calculated the diurnal and seasonal components of the Yarkovsky effect for several objects, and in all cases the seasonal component was significantly smaller. Even in the case of (1566) Icarus, which has an obliquity equal to 103°, the diurnal component for this object was more than twice the magnitude of the seasonal component over a range of likely thermal conductivities.

Heat transport is at the heart of the Yarkovsky effect. Any theoretical derivation of the Yarkovsky effect begins with assumptions of how heat is transported through the body. Spitale & Greenberg (2001), took an intuitive numerical approach, where the volume of an asteroid was divided into cells. The cells were uniformly spaced in longitude, ϕ, and latitude, θ, and spacing in the radial direction varied, allowing for the cells with the largest temperature fluctuations (those near the surface) to be thinner than those with smaller temperature fluctuations.

At a given time $t_0 + \Delta t$ the temperature of each cell was determined via

$$T(t_0 + \Delta t) = T(t_0) + \Delta t \left.\frac{\partial T}{\partial t}\right|_{t_0} + O(\Delta t^2) \tag{1.1}$$

During each timestep Δt, the thermal wave travels a distance

$$l \sim \sqrt{\frac{K \Delta t}{\rho C_p}} \tag{1.2}$$

where K is the thermal conductivity, ρ is the surface density, and C_p is the specific heat at constant pressure. This expression requires that the timesteps be chosen so that l is never larger than the smallest cell.

For each cell, the heat traveling across all boundaries must balance with the cell's internal energy. This results in an expression for $\partial T/\partial t$ in Equation 1.1,

$$\rho V C_p \frac{\partial T}{\partial t} = \oint \mathbf{J}(t) \cdot d\mathbf{s} \tag{1.3}$$

which is integrated over the surface of each cell. V is the volume of the cell, $\mathbf{J}$ is the heat flux, and $d\mathbf{s}$ is the vector element of each surface area.

Take A_{ij} to be the area, and J_{ij} to be the heat flux over a cell face (i, j). If the cells are small enough so that the heat flux is uniform over each face, the total heat flow is

$$\oint \mathbf{J}(t_0) \cdot d\mathbf{s} = J_{r+}A_{r+} + J_{r-}A_{r-} + J_{\theta+}A_{\theta+} + J_{\theta-}A_{\theta-} + J_{\phi+}A_{\phi+} + J_{\phi-}A_{\phi-} \tag{1.4}$$

where + and - represent the opposite sides of a face oriented in r, θ, or ϕ.

Cell faces that adjoin another cell transport heat via conduction, so

$$J_{ij} = k(\nabla T)_{ij} \cdot \hat{\mathbf{s}}_{ij} \tag{1.5}$$

where $(\nabla T)_{ij}$ is the temperature gradient. The gradient across a face at coordinates (r, θ, ϕ) is equal to (for example),

$$(\nabla T)_{r+} = \frac{T(r + \Delta r, \theta, \phi) - T(r, \theta, \phi)}{\Delta r} \tag{1.6}$$

A cell face on the surface has a heat flux governed by impinging solar radiation and emitted thermal radiation, so that

$$J_{surface} = (1 - A)S_{\odot}(\hat{\mathbf{n}} \cdot \hat{\mathbf{r}}) - \epsilon\sigma T^4 \tag{1.7}$$

where A is the bond albedo, $S_\odot$ is the solar flux at the asteroid's surface, $\hat{\mathbf{n}}$ is a vector normal to the face, $\hat{\mathbf{r}}$ is a unit vector in the direction of the sun, ϵ is the surface thermal emissivity, and σ is the Stefan-Boltzmann constant.

The net radiative reaction force, $\mathbf{F}$, is given by a sum of the force per unit area $\mathbf{f}$ acting on each surface cell i.

$$\mathbf{F} = \sum_{i=1}^{n} \mathbf{f}_i A_i. \tag{1.8}$$

Spitale and Greenberg then assumed that emitted radiation followed Lambert's law, so that power radiated into unit solid angle was

$$I(\zeta) = \beta \cos(\zeta), \tag{1.9}$$

where ζ is zenith angle, and β is a normalization factor that satisfies the following integral taken over the outward hemisphere

$$\int I(\zeta) d\Omega = \epsilon_i \sigma T_i^4 A_i \tag{1.10}$$

Finally, the net Yarkovsky force is given by,

$$\mathbf{F} = \sum_{i=1}^{n} \frac{2}{3} \frac{\epsilon_i \sigma T_i^4}{c} \hat{\mathbf{n}}_i A_i \tag{1.11}$$

There have been few direct measurements of the Yarkovsky drift. Chesley et al. (2003) used radar ranging to make the first direct detection. They measured the rate of change of (6489) Golevka's semi-major axis (da/dt) to be of order 10^{-4} AU/Myr. A magnitude da/dt of 10^{-3} AU/Myr Yarkovsky drift was associated with asteroid 1992 BF by linking modern astrometry with observations from 1952 (Vokrouhlický et al., 2008). The third and fourth chapters of this dissertation describe an orbit-fitting method that was used to measure Yarkovsky drifts for 54 NEAs.

1.4 Thermophysical Modeling

Although asteroids have been studied for over two hundred years, values of the fundamental physical properties of many of the objects in this numerous class remain unknown. At present, thermophysical properties such as thermal inertia, regolith thickness, and surface particle size exist for only about two dozen asteroids (Delbó et al., 2007, 2009), plus the handful that have been visited by spacecraft (O'Rourke et al., 2011; Capaccioni et al., 2009; Gulkis et al., 2010; Coradini et al., 2011; Okada et al., 2006; Kitazato et al., 2008; Capria et al., 2011).

Measurements of thermophysical properties can reveal details about asteroid surface processes and dynamics. Low values of thermal conductivity, and therefore thermal inertia, are thought to be consistent with the presence of regolith (Scheeres et al., 2002), which could be indicative of an object's collisional history and is thought to set limits on the rotation rate. Estimating a body's thermal inertia is vital for predicting the Yarkovsky drift magnitude (Bottke et al., 2002b; Delbó et al., 2007; Nugent et al., 2012b; Masiero et al., 2012).

The final portion of this dissertation focuses on the development of a new, detailed thermophysical model that combines detailed radar-based shape measurements with WISE observations. It builds on a well-established foundation of asteroid thermophysical modeling created by groups such as Brown (1985); Lebofsky et al. (1986); Spencer et al. (1989); Tedesco et al. (2002); Lagerros (1996a,b, 1997, 1998); Delbó et al. (2007); Harris (1998); Müeller & Lagerros (1998); Müller (2002); Matter et al. (2011) and Horner et al. (2012). Several of these studies used a free parameter, η (known as the beaming parameter) to account for variations in emission with phase angle that are not modeled properly by a smooth surface (Lagerros, 1996a). An alternative to a beaming parameter is to model the surface as being covered by sub-facets forming regular craters, a method used by workers such as Hansen (1977); Emery et al. (1998); Wright (2007) and Delbó et al. (2007). These craters simulate realistic surface reflectivity and do not necessarily represent actual individual surface features.

The main goals for many of these previous studies was the accurate determination of

Table 1.1 Recently measured values of thermal inertia.

Object	Type	Γ (J m^{-2} s$^{-0.5}$ K^{-1})	Reference
(21) Lutetia	Main Belt	20-30	Coradini et al. (2011)
(41) Daphne	Main Belt	< 50	Matter et al. (2011)
(1580) Betulia	Near-Earth	~ 180	Harris et al. (2005)
(1173) Anchises	Jovian Trojan	25-100	Horner et al. (2012)
(2861) Steins	Main Belt	450-850	Gulkis et al. (2010)
(25143) Itokawa	Near-Earth	750	Müller et al. (2005)
(33342) 1998 WT24	Near-Earth	100-300	Harris et al. (2007)
(101955) 1999 RQ36	Near-Earth	600 ± 150	Emery et al. (2012)
(162173) 1999 JU3	Near-Earth	200-600	Müller et al. (2011)
(308635) 2005 YU55	Near-Earth	500-1500	Lim et al. (2012)
2002 NY40	Near-Earth	~ 100	Müller et al. (2004)

albedo and diameter. This process was advanced by the introduction of the Near-Earth Thermal Model (NEATM) by Harris (1998), a valuable tool that is widely used today. However, advances in computing and data availability have led several researchers to develop more detailed thermal models that supply information about thermal inertia, $\Gamma = \sqrt{K\rho C_p}$ and produce more accurate asteroid diameters, which feed into Yarkovsky predictions.

For example, Delbó et al. (2007) used a statistical method to determine the thermal inertia of a small sample of objects, and found that thermal inertia may be inversely proportional to asteroid diameter. Horner et al. (2012) used a thermophysical model to measure the thermal inertia of Jupiter trojan (1173) Anchises, as did Matter et al. (2011) for (41) Daphne. A recent paper by Rozitis & Green (2011) presented a new thermophysical model that explored representations of rough-surface beaming. Harris (2006) provides a summary table of measured thermal inertias of asteroids, which shows a trend of low ($\sim$ 10 J m^{-2} s$^{-0.5}$ K^{-1}) thermal inertias for main belt asteroids, and thermal inertias ranging between $\sim 350 - 150$ J m^{-2} s$^{-0.5}$ K^{-1} for NEAs. For comparison, lunar regolith has a measured thermal inertia of 50 J m^{-2} s$^{-0.5}$ K^{-1} (Delbó & Tanga, 2009). Thermal inertia values of 11 asteroids are given in Table 1.1.

Non-dimensional parameters are commonly used in thermophysical modeling, both for simplicity and ease of comparison between models. The characteristic length scale in these

problems is the skin depth, $l_s = \sqrt{\frac{K}{\rho C_p \omega}}$. Here K is the thermal conductivity, ρ is the density, C_p is the specific heat capacity, and ω is the rotational frequency of the object. Another useful parameter for describing the system is the thermal parameter (Spencer et al., 1989), Θ, defined as

$$\Theta = \frac{\sqrt{K \rho C_p \omega}}{\epsilon \sigma T^3} \tag{1.12}$$

Here ϵ is the emissivity, σ is the Stefan-Boltzmann constant, and T is the sub-solar temperature of the surface. This can be rewritten in terms of thermal inertia Γ as

$$\Theta = \frac{\Gamma \sqrt{\omega}}{\epsilon \sigma T^3} \tag{1.13}$$

If the surface of the body is in equilibrium with the incident radiation, $\Theta = 0$. Objects with low Θ are often referred to as "slow rotators", as heat is conducted quickly relative to the rotation rate. A body with uniform surface temperature would have Θ approaching infinity, and objects with high Θ are termed "fast rotators" (Spencer et al., 1989).

1.5 Structure of this Dissertation

The second chapter of this dissertation focuses on predictions of Yarkovsky magnitudes for 540 NEAs, with the goals of identifying interesting targets for future Yarkovsky measurements, and encouraging current observations to enable future detections. We used geometric albedos (p_V) and diameters derived from NEOWISE as well as geometric albedos and diameters from the literature, to produce more accurate diurnal Yarkovsky drift predictions for 540 NEAs out of the current sample of $\sim$ 8800 objects that have been discovered to date. The work in this chapter is also published as Nugent et al. (2012a).

The third chapter of this dissertation introduces a new method for detecting the Yarkovsky drift, and the fourth chapter discusses the results and implications from this new method. We identified and quantified semi-major axis drifts in NEAs by performing orbital fits to optical and radar astrometry of all numbered NEAs. We discuss on a subset of 54 NEAs that

exhibit some of the most reliable and strongest drift rates. Our selection criteria include a *Yarkovsky sensitivity* metric that quantifies the detectability of semi-major axis drift in any given data set, a signal-to-noise metric, and orbital coverage requirements. In 42 cases, the observed drifts ($\sim 10^{-3}$ AU/Myr) agree well with numerical estimates of Yarkovsky drifts. This agreement suggests that the Yarkovsky effect is the dominant non-gravitational process affecting these orbits, and allows us to derive constraints on asteroid physical properties. We define the *Yarkovsky efficiency* f_Y as the ratio of the change in orbital energy to incident solar radiation energy, and we find that typical Yarkovsky efficiencies are $\sim 10^{-5}$. These two chapters have also been published as Nugent et al. (2012b).

The fifth chapter of this dissertation describes the development of a detailed themophysical model of (29075) 1950 DA. Using radar-derived shape models and hundreds of infrared observations by the WISE spacecraft, we derived thermal inertia and roughness parameters for these objects. The thermophysical properties derived from the application of the model can be used to improve estimates of the strength of the Yarkovsky drift on this NEA and others. The work in this chapter has been submitted to The Astrophysical Journal.

This dissertation represents a new and original contribution to the study of NEAs. We increased the number of published predicted Yarkovsky drifts by an order of magnitude, increased the number of Yarkovsky detections by a factor of four, and developed new code to measure thermophysical parameters.

CHAPTER 2

Yarkovsky Drift Predictions

2.1 Introduction

In this chapter, we give predictions of Yarkovsky drifts for 540 NEAs. The goal for this work was to highlight those objects likely to have very high drifts, so that observers could target these objects. Optical observations on the order of 10 years will be needed to produce drift measurements for many of the fastest drifting objects.

The Yarkovsky effect has been modeled by several researchers (Vokrouhlický et al. (2000); Spitale & Greenberg (2001), for example). Mathematical formulations, such as those by Vokrouhlický et al. (2000), indicate that Yarkovsky drift is inversely proportional to diameter. Although the amount of absorbed radiation increases with the square of the diameter, mass increases with the cube of the diameter (D), so drift rate is expected to show a $1/D$ dependence.

However, because thermal inertia could also depend on size, the size-dependence of Yarkovsky drift could be more complicated than presently assumed. Theory predicts that the more massive a body is, the more regolith it should retain (Scheeres et al., 2002), and regolith may act as an insulating blanket (though for bodies smaller than 10 km in diameter, spin state may be more indicative of regolith presence). Low porosity and high thermal inertia should create a longer time lag between absorbed radiation and thermal re-radiation, perhaps resulting in a stronger Yarkovsky effect (depending on the rotation state).

Additionally, these models incorporate physical properties of asteroids that are often poorly measured. Although obliquity, heat capacity, thermal conductivity, and bulk density

are generally difficult to quantify, even more basic properties such as geometric albedo (p_V) and diameter can be ill-constrained. This dearth of information has hindered the accuracy of Yarkovsky predictions.

In thermally-dominated WISE wavelengths, it has been shown that for asteroids observed with good signal-to-noise ratios and relatively low amplitude lightcurve variations, effective spherical diameter can be determined to within ±10%, and p_V can be determined to within ±25% of the amount of the albedo (Mainzer et al., 2011c,d). Combining WISE measurements with published reliable diameters determined from in situ spacecraft visits, stellar occultations, and radar produces a list of NEOs with well-determined diameters and geometric albedos used in this chapter.

2.2 Methods

We employed the mathematical formulation of the diurnal Yarkovsky effect developed by Vokrouhlický et al. (2000) to numerically estimate Yarkovsky drifts. Although our methods are not identical, this work follows that of Vokrouhlický et al. (2005), who predicted drifts for 28 NEAs. We expand from that foundation, incorporating newly available physical properties.

For a time step along an NEA's orbit, the Yarkovsky acceleration was computed following equation (1) of Vokrouhlický et al. (2000). This equation assumes a spherical body and that temperatures throughout the body do not greatly deviate from an average temperature. Obliquity was assumed to be 0° to produce maximum drift. Therefore, the reported drifts in this chapter are upper limits. Additionally, a 0° obliquity assumes that all drift is due to the diurnal Yarkovsky effect, as the seasonal Yarkovsky effect has zero magnitude for this case (Bottke et al., 2006). This acceleration was resolved along orthogonal directions, and Gauss' form of Lagrange's planetary equations (Danby, 1992) was employed to evaluate an orbit-averaged da/dt.

The magnitude of the diurnal Yarkovsky drift depends on physical parameters which can

be ill-defined. The drift magnitude is not linearly related to these unknown parameters, and so the resultant drift magnitude was statistically modeled to more accurately determine the effect of these uncertainties. For each NEA, we used p_V and diameter measurements derived by NEOWISE (Mainzer et al., 2011b) or other sources of reliable diameter and p_V measurements in the literature, primarily radar detections and stellar occultations. We employed a Monte Carlo method to explore how variations in physical parameters contribute to errors in the prediction of da/dt. For 1000 realizations per NEA, we added Gaussian-distributed noise to the diameter and p_V measurements, so that standard distribution of the noise corresponded to the 1σ error bars on those measurements.

As the formulation of Vokrouhlický et al. (2000) relies on Bond albedo A, we approximated A using $A \approx (0.290 + 0.684G)p_V$, where G is the phase curve slope parameter (Bowell et al., 1989). In seven cases, G was available in the JPL Small-Bodies database (Chamberlin, 2008). In the remaining cases, G was taken to equal 0.15, as this was the value used to compute physical properties of NEAs in Mainzer et al. (2011a), based on the standard value assumed by the Minor Planet Center for computing H.

Additionally, we varied the thermal conductivity, bulk density, and density of the surface layer between the ranges shown in Table 2.1. The physical parameters in Table 2.1 were chosen to represent a range of asteroid compositions, so that our Yarkovsky estimates would represent reasonable estimates of the range of physical properties of rocky asteroids. At one end of the spectrum are physical parameters mimicking a low-density rubble pile, at the other, a regolith-free rock chunk.

Emissivity was always assumed to be 0.9. If rotation rate was not available in the JPL Database (Chamberlin, 2008), the rotation rate was assumed to be 5 revolutions/day, based on the average spin rate values for asteroids 1 to 10 km in diameter shown in Figure 1 of Pravec & Harris (2000). Rotation rates were unavailable for 81% of the NEAs.

The da/dt values quoted in this chapter are the mean of these 1000 realizations. Error bars on da/dt were determined by computing the standard deviation from the mean.

Table 2.1 Physical and thermal properties used for generating predictions of da/dt drifts. Thermal properties are based on the work of Opeil et al. (2010), who measured three meteorites at 200 K. Listed are heat capacity C_p, thermal conductivity K, bulk density of the surface ρ_s, and mean bulk density ρ_b. The surface and bulk densities are assumed to have a similar range of values, however, ρ_s was not necessarily equal to ρ_b for a given object and realization.

Composition	C_p (J kg^{-1}K^{-1})	K (W m^{-1}K^{-1})	ρ_s/ρ_b (kg m^{-3}))
Rubble Pile	500	0.01	1000
Rock Chunk	500	0.50	3000

2.3 Results

We estimated diurnal Yarkovsky drifts for 540 NEAs with measured diameters and geometric albedos. The dozen objects with the highest drifts are listed in Table 2.2, upcoming apparitions of those objects are in Table 2.3, and predicted drifts for all objects are in Table 2.4 (which can be found at the end of this chapter). Tables 2.2 and 2.4 include an order of magnitude estimate of along-track displacement ($\Delta\rho$) that would result from the da/dt drift over 10 years. For this we use the following formulation from Vokrouhlický et al. (2000),

$$\Delta\rho \simeq 7\dot{a}_4(\Delta_{10}t)^2 a_{AU}^{-3/2} \tag{2.1}$$

where $\Delta\rho$ is in units of km, $\dot{a}_4$ is da/dt in units of 10^{-4} AU/Myr, $\Delta_{10}t$ is the time difference between observations in tens of years, and a_{AU} is the semimajor axis of the object in AU. We note that the four of the twelve objects with the largest predicted drifts were discovered by the NEOWISE portion of the WISE mission (2010 JG87, 2010 HX107, 2010 EX11, and 2010 GQ75).

Table 2.2. The 12 NEAs with largest predicted Yarkovsky drift rates.

NEA	a (AU)	e	i (deg)	D (km)	p_V	Arc	da/dt 10^{-4} AU/Myr	$\Delta\rho$ (km)
2010 JG87	2.76	0.95	16.91	0.41 ± 0.02	0.20 ± 0.04	54 days	72.11 ± 25.12	110.0
2006 HY51	2.60	0.97	30.58	1.22 ± 0.27	0.16 ± 0.09	2006-2011	54.35 ± 23.85	90.8
2007 EP88	0.84	0.89	20.78	0.64 ± 0.04	0.17 ± 0.04	2007-2010	48.57 ± 16.22	443.8
(137924) 2000 BD19	0.88	0.89	25.69	0.97 ± 0.04	0.25 ± 0.05	1997-2010	34.30 ± 12.02	292.6
2010 HX107	0.80	0.30	3.37	0.06 ± 0.01	0.19 ± 0.07	60 days	33.11 ± 23.05	323.6
2002 LT24	0.72	0.50	0.76	0.14 ± 0.02	0.14 ± 0.07	2002-2010	29.06 ± 16.58	333.1
(153201) 2000 WO107	0.91	0.78	7.78	0.51 ± 0.08	0.13 ± 0.06	2000-2010	23.45 ± 10.14	188.7
2010 EX11	0.96	0.11	9.75	0.04 ± 0.01	0.23 ± 0.09	37 days	23.09 ± 18.64	173.0
2008 EY5	0.63	0.63	5.07	0.36 ± 0.01	0.12 ± 0.03	2008-2011	23.00 ± 9.75	324.6
2006 NL	0.85	0.58	20.08	0.22 ± 0.05	0.46 ± 0.14	2006-2009	20.05 ± 12.66	179.8
2006 MD12	0.84	0.61	27.27	0.27 ± 0.06	0.43 ± 0.13	2006-2009	19.60 ± 12.15	178.6
2010 GQ75	2.43	0.87	43.23	0.37 ± 0.02	0.11 ± 0.03	34 days	19.48 ± 9.83	36.0

Table 2.3. Observing opportunities for NEAs with highest predicted Yarkovsky drift rates. Apparitions listed are when elongation is greater than 90°. Apparitions with magnitude ranges always above 23.5 V(mag) are not shown.

NEA	da/dt 10^{-4} AU/Myr	Apparition			V (mag) range	Dec range degrees
2010 JG87	64.99 ± 23.26	May 29 2014	-	Sep 20 2014	20.3, 24.4	07, 19
2006 HY51	34.32 ± 14.86	Feb 08 2014	-	Jul 06 2014	21.5, 23.6	-12, -03
		Feb 04 2015	-	Jun 17 2015	20.4, 22.9	06, 22
		Feb 05 2018	-	Jul 08 2018	22.3, 24.0	-10, -02
		Mar 11 2019	-	Jun 05 2019	17.9, 21.8	24, 53
		Jan 25 2020	-	Jul 01 2020	23.4, 24.6	00, 08
		Feb 03 2022	-	Apr 01 2022	23.3, 24.3	-09, -06
2007 EP88	31.04 ± 12.04	Mar 14 2013	-	May 14 2013	17.2, 21.2	-58, -03
		Feb 09 2014	-	May 26 2014	19.7, 21.1	-44, -14
		Mar 11 2015	-	Mar 25 2015	19.9, 20.6	-59, -51
		Feb 10 2017	-	May 26 2017	19.5, 21.2	-42, -11
		Feb 19 2018	-	Apr 27 2018	18.8, 21.3	-79, -40
		Feb 17 2020	-	May 24 2020	19.0, 21.4	-43, -09
		Feb 13 2021	-	May 14 2021	19.2, 21.4	-56, -27
(137924) 2000 BD19	34.30 ± 12.02	Dec 15 2012	-	Mar 10 2013	17.8, 20.2	42, 76
		Nov 28 2013	-	Mar 17 2014	18.5, 19.9	31, 53
		Dec 05 2014	-	Feb 28 2015	16.6, 20.2	23, 54
		Jan 23 2017	-	Feb 19 2017	18.2, 19.4	46, 54
		Dec 03 2017	-	Mar 15 2018	18.4, 20.1	36, 61
		Nov 29 2018	-	Mar 15 2019	18.1, 20.2	27, 50
		Dec 14 2019	-	Feb 05 2020	15.7, 19.8	16, 22
		Dec 22 2021	-	Mar 08 2022	17.6, 20.1	43, 85
2010 HX107	69.83 ± 30.39	Apr 28 2015	-	May 19 2015	22.7, 23.3	14, 26
2002 LT24	57.95 ± 20.60	May 22 2013	-	Jul 16 2013	16.6, 21.0	-10, -04
		Jun 10 2016	-	Jul 13 2016	20.6, 22.1	-06, 08
(153201) 2000 WO107	23.45 ± 10.14	Dec 15 2013	-	Feb 06 2014	18.7, 21.8	-02, 20
		Nov 08 2014	-	Feb 26 2015	18.9, 22.2	17, 31
		Nov 05 2015	-	Mar 04 2016	19.7, 21.8	20, 34
		Nov 13 2016	-	Feb 25 2017	18.9, 22.2	19, 44
		Dec 09 2017	-	Jan 10 2018	19.9, 21.5	08, 13
		Nov 29 2020	-	Feb 14 2021	13.0, 22.1	13, 25
		Nov 05 2021	-	Mar 01 2022	19.3, 22.1	19, 32
2010 EX11	89.47 ± 40.33	(not observable)				

Table 2.3 (cont'd)

NEA	da/dt 10^{-4} AU/Myr	Apparition			V (mag) range	Dec range degrees
2008 EY5	31.79 ± 10.60	Feb 25 2013	-	Mar 23 2013	17.4, 19.1	-76, -46
		Feb 25 2014	-	Mar 20 2014	17.6, 19.4	-85, -45
		Feb 27 2015	-	Mar 17 2015	18.2, 19.5	-69, -43
		Mar 02 2016	-	Mar 10 2016	19.1, 19.6	-51, -43
2006 NL	20.05 ± 12.66	Jun 30 2013	-	Oct 02 2013	16.7, 21.8	-42, 19
		Jul 15 2014	-	Sep 05 2014	20.3, 21.8	-30, -08
		Jun 21 2017	-	Oct 09 2017	19.5, 21.2	-60, -04
		Jul 07 2020	-	Sep 27 2020	15.4, 21.8	-38, 62
		Jul 06 2021	-	Sep 18 2021	19.9, 21.8	-54, -08
2006 MD12	19.60 ± 12.15	May 22 2012	-	Aug 30 2012	18.6, 21.3	-61, -15
		Jun 12 2015	-	Aug 20 1015	19.4, 21.5	-61, -24
		May 25 2016	-	Aug 15 2016	18.3, 21.5	-15, 55
		May 18 2019	-	Aug 31 2019	17.8, 21.2	-28, 02
2010 GQ75	36.30 ± 12.49	Apr 14 2013	-	Sep 02 2013	23.3, 25.7	-53, -32
		Apr 30 2017	-	Jul 25 2017	21.5, 24.5	-70, -36

Individual realizations for the NEA with the fastest predicted drift, 2010 JG87, are examined in Figures 2.1 and 2.2. In each of these figures, all 1000 realizations of physical parameter combinations are shown, so their individual influences are apparent for this object.

2010 JG87's diameter was determined to within ±10% (Mainzer et al., 2011b) based on the WISE observations (Figure 2.1), and as diameter and bulk density are used to estimate mass, it is the uncertainty in bulk density that mainly determines the predicted drift for this object (Figure 2.2). Surface density and thermal conductivity both contribute to the thermal lag, and for this object, low values of K and ρ_s lead to a thermal lag that produces the strongest drifts (given the object's assumed rotation period of 5 revolutions/day). As geometric albedo has been determined to be 0.20±0.04 for this object, the range of geometric albedo values explored do not strongly influence the resulting drift.

We now examine the values that govern Yarkovsky strength for all objects in our sample. As we are comparing the mean da/dt values of each object, the following compares drifts effectively computed with the same bulk density and density of the surface layer. The predicted diurnal da/dt has a 1/D dependence, and also depends on the amount of average incident radiation the NEA receives per orbit and da/dt.

The 1/D dependence can be seen in Figure 2.3. As all objects in these plots are assumed

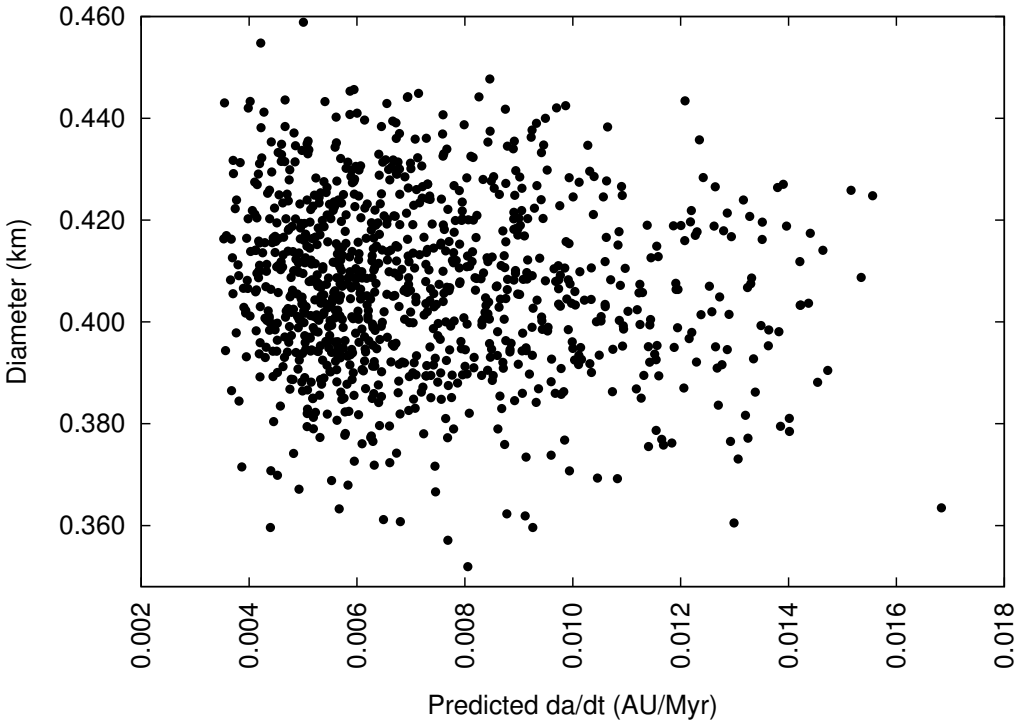

Figure 2.1 1000 realizations of diameter vs da/dt for NEA 2010 JG87. Each point represents the drift produced by a different combination of physical parameters. This object has the fastest predicted diurnal drift of all the NEAs in this chapter, with $da/dt = (72.11 \pm 25.12) \times 10^{-4}$ AU/Myr. Although Yarkovsky drift has a $1/D$ dependence, the relatively small error bars on this object's diameter (and therefore the small range of diameters shown in this plot), combined with the variations in the other parameters (surface density, bulk density, thermal conductivity K, p_v, and G) prevent this dependence from being immediately apparent in this figure. For a clearer illustration of the relationship between da/dt and diameter, see Figure 2.3. For the relationship between da/dt and the other physical properties that were varied during each realization, see Figure 2.2.

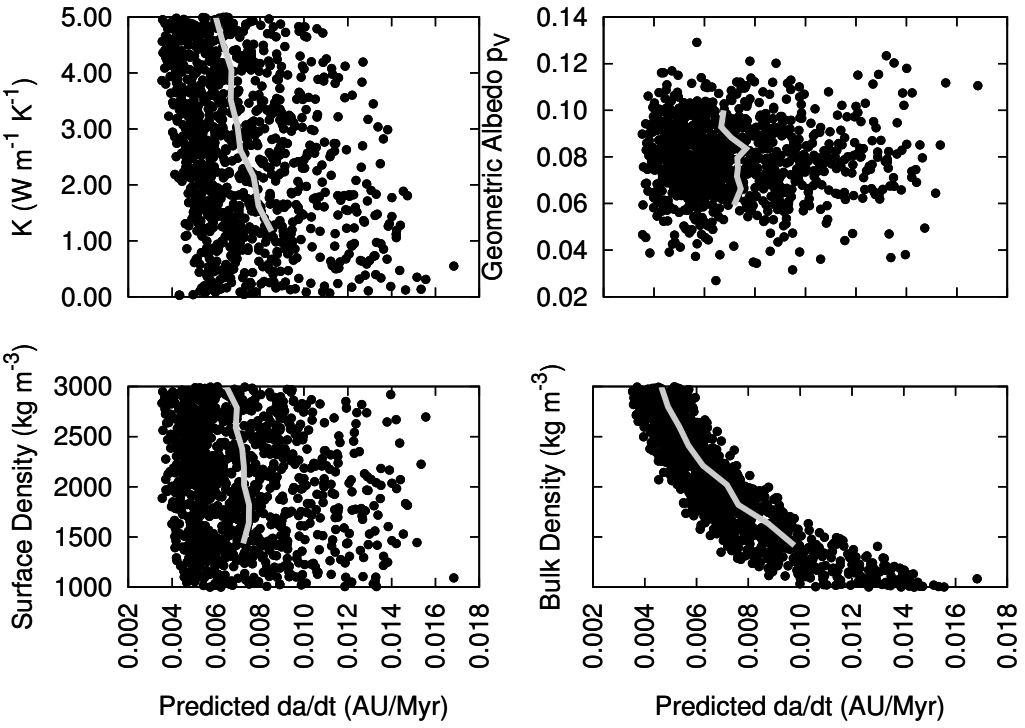

Figure 2.2 1000 realizations of predicted diurnal da/dt drift for 2010 JG87, the NEA with the fastest predicted diurnal drift in this paper. For each realization, diameter, thermal conductivity, geometric albedo, slope parameter G, density of the surface layer, and bulk density were varied as described in the text. Grey lines are running averages. For this object, it is the uncertainty in bulk density that is mainly responsible for the span of calculated da/dt drifts, as the diameter of this object is well-constrained (see Figure 2.1). Also visible are the relationships between thermal conductivity and surface density and drift. These two properties govern the thermal lag angle.

to have the same bulk density (2000 kg m^{-3}), it is only the difference in diameters that produces different mass estimates.

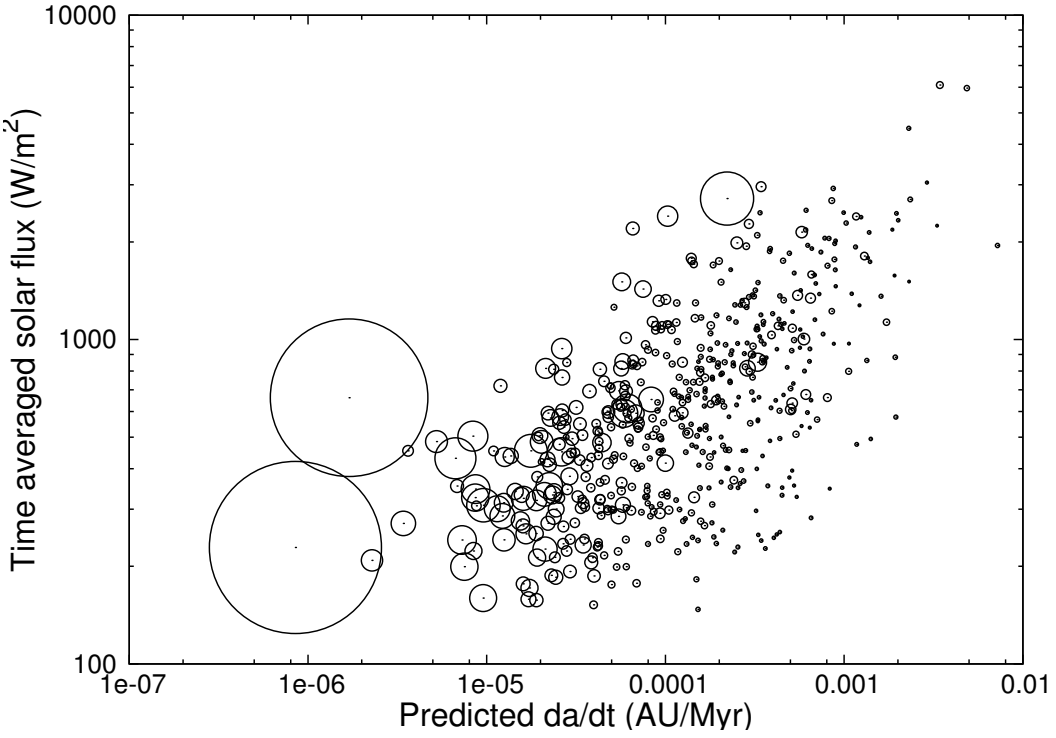

Figure 2.3 Relationship between the time averaged solar flux each NEA receives per orbit and predicted diurnal da/dt drift. Circle sizes are proportional to the diameter of the object. The more solar flux an object receives during its orbit, the more power is available to the Yarkovsky drift. However, this link is tempered by the the diameter– larger objects experience a smaller drift than smaller objects, given the same average incident radiation.

After diameter, the second parameter that strongly influences drift magnitude is the time averaged solar flux, as seen in Figure 2.3. At a given point in an orbit, solar flux is given by S_*/R_{helio}^2, where S_* is the solar flux at 1 AU and R_{helio} is the asteroid's heliocentric distance in AU. The time averaged solar flux is the mean of these fluxes calculated over points evenly spaced in time along the asteroid's orbit. As the figure shows, the more light received by the NEA over its orbit, the more light is available for re-emission and the loss of momentum that powers the drift.

Many values of da/dt reported in Table 2.4 have large error bars due to uncertainties in

physical properties. Observations that further constrain the obliquity, density, rotation rate, thermal conductivity and heat capacity would also constrain predicted drift rates. Measurements of thermal properties of these objects would be valuable, as would the measurement of rotation rates and obliquities (either from lightcurves or radar observations). It is expected that 1/6 objects larger than 200 meters are binary systems (Margot et al., 2002; Pravec et al., 2006), a property which could enable density measurements.

Historically, Yarkovsky detections require either radar observations over three apparitions (Chesley et al., 2003) or optical observations that meet a set of criteria. The drift-fitting method discussed in the next chapter requires an object to (1) have an observed arc of at least ~ 15 years, (2) have observations distributed throughout that arc in time (defined as at least 8 observations per orbit for at least 5 orbits) and (3) have a fraction of these observations at favorable geometries and distances (defined by the Yarkovsky sensitivity $s_Y > 2.0$).

None of the objects in Table 2.2 have enough optical or radar observations to meet the above criteria for detection. Therefore, when possible we encourage the community to observe these objects and contribute astrometry to the Minor Planet Center. More astrometry is needed for all these objects to enable a future Yarkovsky detection via a fit to optical-only data.

To facilitate these observations, Table 2.3 provides apparitions and associated apparent magnitude ranges for these objects between April 1st, 2012 and April 1st, 2022. These apparitions are defined as the times when the object's elongation is greater than 90°, and were generated using the JPL's Horizons ephemeris computation service.

The worldwide community of amateur and professional follow up observers is encouraged to consult this table when planning their observations. Several of the brighter objects may also be automatically picked up by sky surveys such as (in order of decreasing number of observations) PanSTARRS, the Catalina Sky Survey, Spacewatch, and the Lincoln Near Earth Asteroid Research Program (Larson, 2007; McMillan, 2007; Stokes et al., 2000). However, some of these objects only have brief windows where their elongation is greater than 90° and $V < 20.5$ mag (which is roughly the sensitivity limit of most surveys) and may be missed

without special attention. The two brightest objects are likely to be automatically observed by surveys, however, additional observations that expanded coverage over the orbit in mean anomaly would be useful.

Unfortunately, not all objects are easily observable. 2010 EX11 does not have an elongation greater than 90° during that time span, though on two apparitions (in 2012 and 2013) it does exceed 60°. Several of the remaining objects are extremely faint, with V (mag) rarely brighter than 23.5. Although these observations may be challenging, they are vital for well-defined orbits and future Yarkovsky detections.

2.4 Conclusion

In this chapter we use WISE-derived geometric albedos and diameters, as well as values for geometric albedos and diameters published in the literature, to produce more accurate diurnal Yarkovsky drift predictions for 540 NEAs. Table 2.2 lists the 12 objects in our sample with the fastest rates, and Table 2.3 gives their apparitions over the next decade. Three of these objects have observed arcs of less than a year, and we encourage observers to obtain more astrometry of these objects when possible. Predicting which NEAs are most likely to be subject to strong Yarkovsky drifts relies upon robust determinations of asteroid physical properties, underscoring the need to continue to obtain such characterization data.

Table 2.4. NEAs with highest predicted Yarkovsky drift rates

NEA	a (AU)	e	i (deg)	D (km)	p_V	Arc	da/dt 10^{-4} AU/Myr	$\Delta\rho$ (km)
2010 JG87	2.76	0.95	16.91	0.41 ± 0.02	0.20 ± 0.04	54 days	72.11 ± 25.12	110.0
2006 HY51	2.60	0.97	30.58	1.22 ± 0.27	0.16 ± 0.09	2006-2011	54.35 ± 23.85	90.8
2007 EP88	0.84	0.89	20.78	0.64 ± 0.04	0.17 ± 0.04	2007-2010	48.57 ± 16.22	443.8
(137924) 2000 BD19	0.88	0.89	25.69	0.97 ± 0.04	0.25 ± 0.05	1997-2010	34.30 ± 12.02	292.6
2010 HX107	0.80	0.30	3.37	0.06 ± 0.01	0.19 ± 0.07	60 days	33.11 ± 23.05	323.6
2002 LT24	0.72	0.50	0.76	0.14 ± 0.02	0.14 ± 0.07	2002-2010	29.06 ± 16.58	333.1
(153201) 2000 WO107	0.91	0.78	7.78	0.51 ± 0.08	0.13 ± 0.06	2000-2010	23.45 ± 10.14	188.7
2010 EX11	0.96	0.11	9.75	0.04 ± 0.01	0.23 ± 0.09	37 days	23.09 ± 18.64	173.0
2008 EY5	0.63	0.63	5.07	0.36 ± 0.01	0.12 ± 0.03	2008-2011	23.00 ± 9.75	324.6
2006 NL	0.85	0.58	20.08	0.22 ± 0.05	0.46 ± 0.14	2006-2009	20.05 ± 12.66	179.8
2006 MD12	0.84	0.61	27.27	0.27 ± 0.06	0.43 ± 0.13	2006-2009	19.60 ± 12.15	178.6
2010 GQ75	2.43	0.87	43.23	0.37 ± 0.02	0.11 ± 0.03	34 days	19.48 ± 9.83	36.0
2010 GR7	1.83	0.85	24.22	0.45 ± 0.01	0.38 ± 0.07	2010-2011	19.33 ± 9.42	54.6
2001 CQ36	0.94	0.18	1.29	0.07 ± 0.01	0.41 ± 0.11	2001-2011	19.13 ± 13.63	146.9
2010 AJ30	0.81	0.30	7.59	0.11 ± 0.02	0.12 ± 0.06	37 days	18.61 ± 12.30	178.1
2004 LG	2.07	0.90	70.97	0.87 ± 0.01	0.15 ± 0.03	2004-2010	17.26 ± 7.47	40.7
2010 HW81	1.22	0.73	12.85	0.35 ± 0.05	0.04 ± 0.02	10 days	16.08 ± 8.64	83.8
2010 NB2	2.08	0.76	28.66	0.21 ± 0.01	0.30 ± 0.05	34 days	14.09 ± 9.16	32.9
2010 NJ1	0.97	0.54	11.22	0.22 ± 0.04	0.26 ± 0.10	2010-2011	13.97 ± 8.77	102.6
(252399) 2001 TX44	0.87	0.55	15.21	0.26 ± 0.05	0.68 ± 0.20	2001-2010	13.81 ± 9.00	118.2
2010 GA7	0.91	0.39	30.02	0.15 ± 0.02	0.26 ± 0.12	54 days	13.57 ± 9.25	108.9
(162195) 1999 RK45	1.60	0.77	5.89	0.39 ± 0.08	0.19 ± 0.06	1999-2011	13.39 ± 8.38	46.4
(139289) 2001 KR1	1.26	0.84	23.23	1.13 ± 0.24	0.13 ± 0.07	2001-2010	12.98 ± 7.36	64.3
2005 GB120	0.79	0.39	9.15	0.21 ± 0.01	0.28 ± 0.04	2005-2010	12.44 ± 7.53	123.7
2006 SY5	1.04	0.15	7.56	0.09 ± 0.02	0.34 ± 0.23	2006-2007	12.19 ± 9.89	80.1
2010 NU1	2.12	0.78	33.70	0.29 ± 0.05	0.07 ± 0.03	8 days	11.76 ± 7.57	26.7
2005 MB	0.99	0.79	41.40	1.01 ± 0.14	0.25 ± 0.10	2003-2011	11.66 ± 5.05	83.5
(234341) 2001 FZ57	0.94	0.60	20.67	0.34 ± 0.05	0.49 ± 0.19	2000-2011	11.58 ± 6.71	88.4
2010 LJ61	1.04	0.46	9.73	0.19 ± 0.03	0.21 ± 0.08	10 days	11.02 ± 8.22	72.6
(225312) 1996 XB27	1.19	0.06	2.47	0.08 ± 0.02	0.48 ± 0.26	1996-2009	10.63 ± 8.81	57.4
2008 EM9	1.96	0.85	9.40	0.79 ± 0.03	0.32 ± 0.07	2008-2011	10.60 ± 5.22	27.0
(66400) 1999 LT7	0.86	0.57	9.07	0.41 ± 0.08	0.18 ± 0.09	1999-2010	10.25 ± 5.93	90.7
2008 CN1	0.77	0.35	7.22	0.23 ± 0.00	0.20 ± 0.03	2008-2010	9.93 ± 6.71	102.8

Table 2.4 (cont'd)

NEA	a (AU)	e	i (deg)	D (km)	p_V	Arc	da/dt 10^{-4} AU/Myr	$\Delta\rho$ (km)
(164202) 2004 EW	0.99	0.28	4.66	0.16 ± 0.03	0.36 ± 0.22	2004-2011	8.97 ± 6.47	63.9
2010 NG1	0.85	0.33	24.74	0.23 ± 0.04	0.23 ± 0.11	71 days	8.96 ± 6.03	80.1
(141531) 2002 GB	0.99	0.53	22.56	0.30 ± 0.01	0.48 ± 0.08	2002-2012	8.91 ± 5.37	63.1
2009 JO2	0.89	0.48	19.63	0.31 ± 0.03	0.34 ± 0.09	2009-2011	8.85 ± 5.55	74.0
(255071) 2005 UH6	1.00	0.63	2.64	0.52 ± 0.14	0.22 ± 0.07	2005-2011	8.83 ± 6.11	61.7
2010 FA81	1.20	0.15	15.48	0.10 ± 0.02	0.22 ± 0.09	48 days	8.75 ± 7.80	46.9
(33342) 1998 WT24	0.72	0.42	7.34	0.42 ± 0.04	0.56 ± 0.20	1998-2008	8.70 ± 4.93	100.0
1998 SV4	0.82	0.64	53.30	0.74 ± 0.15	0.20 ± 0.06	1998-2010	8.53 ± 4.40	80.9
(163758) 2003 OS13	1.30	0.74	41.56	0.66 ± 0.13	0.44 ± 0.14	2003-2009	8.52 ± 5.15	40.4
2010 LH14	2.20	0.57	4.66	0.10 ± 0.02	0.27 ± 0.11	152 days	8.30 ± 7.22	17.8
(307918) 2004 EU9	0.88	0.51	28.59	0.37 ± 0.05	0.36 ± 0.10	2004-2010	8.22 ± 5.21	69.7
(267221) 2001 AD2	1.04	0.66	1.66	0.56 ± 0.02	0.10 ± 0.02	2001-2011	8.08 ± 4.37	53.4
2006 KZ112	2.52	0.89	37.76	1.18 ± 0.03	0.27 ± 0.05	2006-2010	8.06 ± 3.89	14.1
2003 HB	0.85	0.38	18.11	0.29 ± 0.05	0.27 ± 0.10	2003-2010	7.79 ± 5.01	69.6
2010 GW62	1.27	0.58	32.43	0.28 ± 0.02	0.38 ± 0.08	72 days	7.62 ± 5.19	37.3
2010 JE87	0.91	0.44	17.15	0.31 ± 0.02	0.11 ± 0.03	5 days	7.42 ± 4.82	60.1
(164207) 2004 GU9	1.00	0.14	13.65	0.16 ± 0.01	0.22 ± 0.04	2001-2011	7.26 ± 6.21	50.8
(275974) 2001 XD	2.04	0.80	11.41	0.63 ± 0.10	0.22 ± 0.10	2001-2010	7.06 ± 4.41	16.9
2010 NY65	1.00	0.37	11.72	0.23 ± 0.01	0.07 ± 0.01	27 days	6.93 ± 4.75	48.9
2010 LK68	1.16	0.47	21.76	0.24 ± 0.02	0.03 ± 0.01	4 days	6.86 ± 4.57	38.3
(141432) 2002 CQ11	0.98	0.43	2.46	0.24 ± 0.04	0.34 ± 0.14	2002-2011	6.83 ± 5.12	49.4
2009 WZ104	0.86	0.19	9.84	0.24 ± 0.00	0.31 ± 0.07	2005-2010	6.59 ± 4.72	58.3
(162269) 1999 VO6	1.14	0.74	40.10	1.01 ± 0.18	0.27 ± 0.11	1993-2011	6.56 ± 3.69	37.9
2010 DK34	2.75	0.76	27.47	0.28 ± 0.01	0.15 ± 0.03	32 days	6.53 ± 4.84	10.0
(41429) 2000 GE2	1.59	0.55	2.19	0.20 ± 0.03	0.27 ± 0.08	1998-2010	6.53 ± 5.07	22.7
(225416) 1999 YC	1.42	0.83	38.22	1.65 ± 0.18	0.09 ± 0.03	1999-2010	6.48 ± 2.77	26.8
(67381) 2000 OL8	1.32	0.54	10.67	0.28 ± 0.06	0.25 ± 0.08	2000-2011	6.43 ± 4.96	29.7
2010 KU7	1.66	0.38	6.76	0.10 ± 0.01	0.22 ± 0.08	40 days	6.42 ± 5.06	20.9
(152564) 1992 HF	1.39	0.56	13.31	0.28 ± 0.05	0.17 ± 0.07	1992-2010	6.40 ± 4.77	27.3
2006 DS14	0.86	0.34	26.53	0.32 ± 0.01	0.12 ± 0.02	2002-2010	6.26 ± 4.00	54.6
2010 GR75	1.73	0.64	17.78	0.28 ± 0.05	0.33 ± 0.09	84 days	6.23 ± 4.47	19.2
(242191) 2003 NZ6	0.79	0.49	18.24	0.37 ± 0.03	0.33 ± 0.07	2003-2010	6.13 ± 4.07	60.7
2002 WZ2	2.46	0.88	51.40	1.60 ± 0.12	0.11 ± 0.03	2002-2010	6.10 ± 3.12	11.1

Table 2.4 (cont'd)

NEA	a (AU)	e	i (deg)	D (km)	p_V	Arc	da/dt 10^{-4} AU/Myr	$\Delta\rho$ (km)
(230111) 2001 BE10	0.82	0.37	17.51	0.40 ± 0.06	0.25 ± 0.06	2001-2010	6.09 ± 4.26	57.0
2005 WC1	1.40	0.49	19.98	0.29 ± 0.06	0.11 ± 0.03	2005-2011	6.00 ± 4.25	25.3
(242643) 2005 NZ6	1.83	0.86	8.50	1.99 ± 0.48	0.04 ± 0.04	2005-2010	5.95 ± 3.48	16.8
2010 JG	1.19	0.32	23.31	0.19 ± 0.03	0.21 ± 0.08	2010-2011	5.88 ± 4.90	31.7
(184990) 2006 KE89	1.05	0.80	45.08	1.96 ± 0.11	0.13 ± 0.03	1994-2012	5.79 ± 2.53	37.5
2010 FG81	1.66	0.39	7.97	0.11 ± 0.00	0.07 ± 0.01	36 days	5.78 ± 4.45	18.9
2010 KX7	0.99	0.17	21.48	0.21 ± 0.02	0.08 ± 0.02	2010-2011	5.71 ± 4.57	40.6
2009 WA	1.14	0.14	29.84	0.16 ± 0.03	0.22 ± 0.14	174 days	5.68 ± 4.51	32.8
2010 OC101	1.22	0.23	13.60	0.15 ± 0.00	0.38 ± 0.07	182 days	5.66 ± 3.95	29.4
(40267) 1999 GJ4	1.34	0.81	34.53	1.64 ± 0.05	0.45 ± 0.09	1955-2009	5.49 ± 2.49	24.8
2010 HZ104	2.25	0.57	20.22	0.14 ± 0.02	0.09 ± 0.06	23 days	5.43 ± 4.51	11.2
2010 LU108	2.24	0.82	9.51	0.82 ± 0.01	0.03 ± 0.01	51 days	5.37 ± 3.11	11.2
2010 OF101	0.95	0.33	23.37	0.30 ± 0.05	0.23 ± 0.12	2010-2011	5.26 ± 3.69	39.7
2010 HC	2.13	0.52	6.88	0.13 ± 0.01	0.33 ± 0.06	114 days	5.25 ± 4.50	11.8
(285339) 1999 JR6	1.37	0.68	20.34	0.61 ± 0.02	0.27 ± 0.06	1999-2011	5.25 ± 3.27	23.0
2003 CR1	1.45	0.46	12.71	0.20 ± 0.03	0.43 ± 0.15	2003-2010	5.20 ± 3.53	20.8
(192559) 1998 VO	1.07	0.23	10.06	0.22 ± 0.04	0.30 ± 0.17	1998-2008	5.15 ± 4.43	32.4
(194268) 2001 UY4	1.45	0.79	5.43	1.24 ± 0.02	0.05 ± 0.01	2001-2011	5.13 ± 2.54	20.5
2010 KY127	2.50	0.88	60.38	1.77 ± 0.29	0.13 ± 0.06	2010-2011	5.12 ± 2.56	9.1
2010 CJ171	2.00	0.49	7.38	0.13 ± 0.00	0.36 ± 0.07	174 days	5.12 ± 4.50	12.7
(277570) 2005 YP180	1.37	0.62	4.11	0.44 ± 0.05	0.18 ± 0.04	2005-2011	5.09 ± 3.37	22.2
2002 GO5	1.90	0.77	13.81	0.75 ± 0.15	0.24 ± 0.08	2002-2004	5.08 ± 3.37	13.6
2005 YY93	2.58	0.88	23.43	1.75 ± 0.06	0.08 ± 0.02	2005-2010	5.03 ± 2.47	8.5
2010 OS22	1.64	0.69	9.36	0.50 ± 0.01	0.41 ± 0.09	2010-2011	5.01 ± 3.02	16.8
(250680) 2005 QC5	0.89	0.36	9.45	0.40 ± 0.01	0.15 ± 0.03	1978-2011	4.94 ± 3.33	41.0
2010 LL68	2.07	0.53	10.49	0.15 ± 0.02	0.06 ± 0.02	124 days	4.93 ± 4.16	11.6
2010 PM58	1.37	0.46	13.60	0.26 ± 0.04	0.10 ± 0.04	181 days	4.80 ± 3.76	20.9
2007 VD12	1.15	0.36	22.86	0.22 ± 0.04	0.39 ± 0.12	19 days	4.63 ± 3.40	26.4
1999 GY5	1.15	0.61	24.44	0.67 ± 0.12	0.04 ± 0.02	1999-2010	4.59 ± 2.90	26.2
2010 PU66	1.49	0.39	18.09	0.18 ± 0.01	0.08 ± 0.02	62 days	4.58 ± 3.87	17.7
(312070) 2007 TA19	0.95	0.51	22.63	0.60 ± 0.10	0.09 ± 0.04	2007-2011	4.55 ± 2.82	34.2
2010 CB55	1.13	0.15	25.92	0.20 ± 0.00	0.04 ± 0.01	189 days	4.51 ± 3.42	26.2
2010 JK33	2.23	0.61	4.03	0.21 ± 0.01	0.15 ± 0.03	2010-2010	4.50 ± 3.63	9.5

Table 2.4 (cont'd)

NEA	a (AU)	e	i (deg)	D (km)	p_V	Arc	da/dt 10^{-4} AU/Myr	$\Delta\rho$ (km)
2010 GO33	2.41	0.70	19.12	0.31 ± 0.02	0.38 ± 0.09	2010-2010	4.49 ± 3.55	8.4
(152754) 1999 GS6	1.19	0.50	2.02	0.41 ± 0.08	0.22 ± 0.11	1999-2010	4.43 ± 3.37	23.9
(4034) Vishnu	1.06	0.44	11.17	0.42 ± 0.07	0.58 ± 0.25	1986-2009	4.37 ± 3.00	28.1
2010 GT7	2.71	0.68	9.28	0.22 ± 0.01	0.33 ± 0.06	75 days	4.37 ± 2.95	6.8
2010 FL	1.91	0.66	11.45	0.35 ± 0.01	0.27 ± 0.05	2002-2010	4.37 ± 3.20	11.5
2002 LS32	1.78	0.70	8.83	0.57 ± 0.12	0.29 ± 0.09	2002-2010	4.35 ± 3.58	12.8
(152671) 1998 HL3	1.13	0.37	2.68	0.30 ± 0.01	0.20 ± 0.04	1998-2012	4.31 ± 3.22	25.2
2007 BM8	1.34	0.72	27.63	1.08 ± 0.17	0.07 ± 0.02	2002-2010	4.26 ± 2.52	19.2
2010 FH81	1.23	0.21	16.79	0.20 ± 0.01	0.09 ± 0.02	107 days	4.21 ± 3.43	21.7
2010 OE22	2.65	0.63	14.31	0.17 ± 0.01	0.18 ± 0.04	61 days	4.20 ± 3.17	6.8
2010 CC55	1.55	0.47	6.79	0.24 ± 0.01	0.03 ± 0.01	2010-2011	4.15 ± 3.08	15.1
2010 GS7	2.71	0.65	9.68	0.20 ± 0.01	0.11 ± 0.03	154 days	4.04 ± 3.15	6.3
2010 LM14	1.11	0.38	25.92	0.36 ± 0.08	0.04 ± 0.01	2010-2011	3.98 ± 3.18	23.8
2010 GF25	1.40	0.73	37.57	1.13 ± 0.10	0.02 ± 0.01	8 days	3.93 ± 2.22	16.7
2010 OB101	1.62	0.52	9.12	0.28 ± 0.02	0.14 ± 0.03	2010-2011	3.90 ± 2.98	13.3
2010 LE15	0.86	0.27	13.26	0.46 ± 0.01	0.15 ± 0.02	2001-2010	3.86 ± 2.72	33.6
2010 LJ68	1.69	0.43	16.50	0.19 ± 0.04	0.04 ± 0.02	7 days	3.85 ± 2.86	12.3
(152637) 1997 NC1	0.87	0.21	16.72	0.43 ± 0.10	0.59 ± 0.20	1997-2009	3.83 ± 2.90	33.3
2010 OL100	2.26	0.65	22.16	0.31 ± 0.04	0.25 ± 0.06	160 days	3.74 ± 2.86	7.7
2002 EZ2	1.25	0.05	13.02	0.21 ± 0.04	0.40 ± 0.12	2002-2009	3.67 ± 3.72	18.4
2010 GK23	2.92	0.70	35.38	0.28 ± 0.04	0.30 ± 0.13	8 days	3.62 ± 3.01	5.1
2005 OU2	1.23	0.37	47.77	0.34 ± 0.07	0.37 ± 0.11	2005-2009	3.57 ± 2.92	18.2
(6239) Minos	1.15	0.41	3.95	0.47 ± 0.12	0.56 ± 0.39	1983-2009	3.54 ± 2.68	20.0
2010 GP67	1.11	0.11	13.27	0.25 ± 0.02	0.03 ± 0.01	205 days	3.53 ± 2.71	21.0
2009 XF2	1.29	0.25	14.01	0.24 ± 0.04	0.27 ± 0.14	202 days	3.52 ± 3.19	16.9
2010 JD87	1.43	0.64	24.58	0.69 ± 0.01	0.09 ± 0.02	28 days	3.50 ± 2.23	14.4
2010 OH126	1.90	0.50	14.39	0.22 ± 0.01	0.10 ± 0.02	15 days	3.49 ± 2.75	9.3
(152941) 2000 FM10	1.48	0.68	8.74	0.82 ± 0.00	0.21 ± 0.03	2000-2012	3.49 ± 2.23	13.5
(3361) Orpheus	1.21	0.32	2.69	0.35 ± 0.06	0.36 ± 0.13	1982-2009	3.44 ± 2.41	18.1
2010 LV108	2.75	0.66	4.78	0.23 ± 0.01	0.03 ± 0.00	30 days	3.44 ± 2.64	5.3
(163243) 2002 FB3	0.76	0.60	20.27	1.62 ± 0.01	0.19 ± 0.03	2002-2010	3.43 ± 1.68	36.1
(228502) 2001 TE2	1.08	0.20	7.62	0.30 ± 0.05	0.19 ± 0.06	2000-2009	3.42 ± 2.72	21.2
2003 TL4	0.78	0.38	12.15	0.38 ± 0.07	0.22 ± 0.07	2003-2009	3.39 ± 2.83	34.6

Table 2.4 (cont'd)

NEA	a (AU)	e	i (deg)	D (km)	p_V	Arc	da/dt 10^{-4} AU/Myr	$\Delta\rho$ (km)
2000 TJ1	1.16	0.08	39.54	0.25 ± 0.04	0.40 ± 0.16	2000-2010	3.37 ± 2.89	18.9
2000 YF29	1.49	0.37	6.30	0.24 ± 0.04	0.25 ± 0.15	2000-2011	3.34 ± 2.66	12.8
2010 OL101	2.61	0.60	26.07	0.20 ± 0.02	0.32 ± 0.09	132 days	3.31 ± 3.01	5.5
2008 EV5	0.96	0.08	7.44	0.40 ± 0.01	0.14 ± 0.01	2008-2010	3.29 ± 2.57	24.6
2010 ON101	1.63	0.41	9.31	0.24 ± 0.02	0.22 ± 0.04	2010-2012	3.29 ± 2.61	11.1
2010 OD101	1.62	0.36	15.39	0.20 ± 0.03	0.22 ± 0.07	80 days	3.29 ± 2.48	11.2
2004 SB20	1.18	0.41	30.28	0.43 ± 0.08	0.41 ± 0.12	2004-2008	3.28 ± 2.41	17.9
(136874) 1998 FH74	2.20	0.88	21.26	3.40 ± 0.13	0.07 ± 0.02	1995-2011	3.28 ± 1.44	7.0
2007 BG29	0.83	0.33	18.51	0.65 ± 0.02	0.26 ± 0.05	2007-2012	3.26 ± 2.22	30.1
2007 YQ56	1.14	0.29	26.46	0.34 ± 0.07	0.16 ± 0.05	2007-2008	3.26 ± 2.55	18.7
1996 GQ	1.99	0.50	0.89	0.21 ± 0.00	0.02 ± 0.00	1996-2010	3.25 ± 2.64	8.1
(285179) 1996 TY11	1.23	0.54	13.93	0.62 ± 0.12	0.09 ± 0.03	1996-2011	3.24 ± 2.24	16.7
2010 JN71	2.39	0.59	17.72	0.21 ± 0.00	0.11 ± 0.02	38 days	3.22 ± 2.29	6.1
(85990) 1999 JV6	1.01	0.31	5.32	0.45 ± 0.03	0.10 ± 0.02	1999-2012	3.18 ± 2.33	22.0
(138971) 2001 CB21	1.03	0.33	7.90	0.58 ± 0.11	0.24 ± 0.12	2001-2011	3.13 ± 2.48	20.8
2010 CN141	1.52	0.40	23.81	0.25 ± 0.01	0.03 ± 0.01	50 days	3.12 ± 2.21	11.7
2003 TJ2	1.32	0.47	17.44	0.45 ± 0.09	0.23 ± 0.07	2003-2012	3.11 ± 2.62	14.4
2010 NZ1	1.37	0.65	32.79	0.85 ± 0.05	0.04 ± 0.01	1997-2010	3.09 ± 1.94	13.5
(277617) 2006 BT7	1.52	0.63	16.14	0.67 ± 0.10	0.19 ± 0.08	2006-2012	3.08 ± 1.94	11.5
2010 CO1	1.01	0.22	23.97	0.38 ± 0.00	0.03 ± 0.00	15 days	3.07 ± 2.16	21.1
2004 XK50	1.45	0.69	38.21	1.04 ± 0.08	0.04 ± 0.01	2004-2011	3.05 ± 1.83	12.2
2010 JH87	1.54	0.54	43.77	0.43 ± 0.07	0.13 ± 0.06	2010-2011	3.05 ± 2.32	11.2
2005 GY110	1.85	0.69	12.64	0.66 ± 0.02	0.19 ± 0.03	2005-2010	2.98 ± 1.84	8.3
(154993) 2005 EA94	1.52	0.66	10.32	0.83 ± 0.05	0.20 ± 0.05	2002-2008	2.94 ± 1.88	11.0
2007 YZ	1.04	0.36	16.42	0.53 ± 0.10	0.09 ± 0.04	2007-2011	2.93 ± 2.23	19.3
(85989) 1999 JD6	0.88	0.63	17.05	1.46 ± 0.02	0.13 ± 0.03	1999-2010	2.93 ± 1.63	24.7
(164201) 2004 EC	2.00	0.86	34.64	2.87 ± 0.57	0.12 ± 0.04	2004-2010	2.88 ± 1.65	7.1
(87024) 2000 JS66	1.20	0.19	14.43	0.31 ± 0.06	0.63 ± 0.34	2000-2009	2.86 ± 2.14	15.3
(252558) 2001 WT1	1.09	0.40	7.15	0.53 ± 0.03	0.06 ± 0.01	2001-2010	2.84 ± 2.00	17.5
(162483) 2000 PJ5	0.87	0.37	51.18	0.92 ± 0.01	0.23 ± 0.03	2000-2010	2.84 ± 1.61	24.3
2010 LU134	1.90	0.55	27.38	0.32 ± 0.03	0.44 ± 0.11	138 days	2.81 ± 1.85	7.5
(38086) Beowulf	1.42	0.57	23.67	0.70 ± 0.20	0.37 ± 0.12	1992-2011	2.79 ± 3.43	11.5
2010 OC103	1.19	0.67	23.11	1.47 ± 0.31	0.02 ± 0.01	2006-2011	2.78 ± 1.60	14.9

Table 2.4 (cont'd)

NEA	a (AU)	e	i (deg)	D (km)	p_V	Arc	da/dt 10^{-4} AU/Myr	$\Delta\rho$ (km)
2010 DJ56	1.25	0.25	34.84	0.32 ± 0.05	0.33 ± 0.15	2003-2010	2.76 ± 2.30	13.8
2010 JF88	2.23	0.66	17.45	0.45 ± 0.01	0.32 ± 0.07	2010-2011	2.74 ± 2.25	5.8
(162416) 2000 EH26	1.85	0.48	0.40	0.14 ± 0.03	0.18 ± 0.14	2000-2005	2.70 ± 3.05	7.5
2007 MK13	1.02	0.14	19.88	0.39 ± 0.01	0.12 ± 0.02	2007-2011	2.69 ± 2.10	18.1
2006 LF	2.14	0.66	7.97	0.50 ± 0.10	0.25 ± 0.08	2002-2009	2.66 ± 1.97	5.9
2008 WB59	1.04	0.19	25.65	0.41 ± 0.07	0.20 ± 0.10	2008-2010	2.63 ± 1.97	17.2
2010 JA35	2.16	0.58	29.00	0.31 ± 0.05	0.11 ± 0.06	201 days	2.62 ± 2.22	5.8
2005 EJ	1.45	0.15	12.46	0.23 ± 0.04	0.43 ± 0.24	2005-2012	2.57 ± 2.31	10.4
2010 FO92	2.14	0.52	6.75	0.25 ± 0.01	0.28 ± 0.05	238 days	2.55 ± 2.05	5.7
2010 CN44	2.85	0.68	3.84	0.34 ± 0.01	0.19 ± 0.04	115 days	2.55 ± 1.93	3.7
2009 UX17	1.19	0.08	10.80	0.31 ± 0.01	0.04 ± 0.01	134 days	2.54 ± 2.19	13.7
2010 GV147	0.96	0.66	44.05	2.05 ± 0.04	0.02 ± 0.00	2010-2011	2.51 ± 1.24	18.7
2010 FQ	1.53	0.36	10.55	0.29 ± 0.00	0.21 ± 0.03	2010-2012	2.50 ± 1.81	9.3
(138947) 2001 BA40	1.12	0.25	12.85	0.44 ± 0.09	0.42 ± 0.26	2001-2007	2.48 ± 2.01	14.7
(207945) 1991 JW	1.04	0.12	8.71	0.42 ± 0.03	0.16 ± 0.04	1955-2009	2.45 ± 1.89	16.2
2010 DM21	2.86	0.66	21.14	0.30 ± 0.01	0.13 ± 0.02	48 days	2.44 ± 1.84	3.5
2006 KD1	2.48	0.78	30.71	1.14 ± 0.12	0.18 ± 0.05	2006-2010	2.41 ± 1.67	4.3
(221980) 1996 EO	1.34	0.40	21.60	0.43 ± 0.05	0.20 ± 0.05	1996-2009	2.40 ± 1.85	10.8
(52381) 1993 HA	1.28	0.14	7.73	0.34 ± 0.10	0.14 ± 0.11	1993-2009	2.39 ± 2.83	11.6
1998 SB15	1.23	0.16	15.63	0.34 ± 0.03	0.06 ± 0.01	1998-2010	2.36 ± 1.95	12.1
2010 HZ108	1.25	0.21	22.88	0.36 ± 0.07	0.06 ± 0.03	180 days	2.32 ± 1.93	11.7
(99942) Apophis	0.92	0.19	3.33	0.27 ± 0.06	0.33 ± 0.08	2004-2012	2.32 ± 2.29	18.3
(239849) 1999 VO11	2.25	0.64	15.80	0.45 ± 0.06	0.32 ± 0.13	1999-2010	2.31 ± 1.76	4.8
2003 WD158	1.43	0.41	16.71	0.44 ± 0.09	0.29 ± 0.09	2003-2008	2.30 ± 1.94	9.5
(238456) 2004 RK	1.39	0.30	18.15	0.33 ± 0.04	0.31 ± 0.14	1986-2010	2.30 ± 1.87	9.8
(275558) 1999 RH33	1.55	0.17	11.02	0.23 ± 0.04	0.73 ± 0.35	1999-2012	2.27 ± 1.89	8.2
(55408) 2001 TC2	1.10	0.22	30.39	0.46 ± 0.01	0.34 ± 0.05	1979-2010	2.27 ± 1.60	13.8
2009 SO103	2.00	0.66	29.46	0.67 ± 0.01	0.43 ± 0.07	2006-2010	2.27 ± 1.56	5.6
2009 UK	1.98	0.48	3.53	0.28 ± 0.02	0.22 ± 0.05	1984-2010	2.25 ± 1.74	5.6
(3200) Phaethon	1.27	0.89	22.23	11.00 ± 0.40	0.02 ± 0.01	1983-2012	2.21 ± 0.74	10.8
2007 FE1	2.02	0.55	9.85	0.39 ± 0.01	0.35 ± 0.07	2007-2010	2.21 ± 1.89	5.4
(85938) 1999 DJ4	1.85	0.48	9.15	0.48 ± 0.10	0.28 ± 0.23	1999-2009	2.18 ± 1.86	6.0
(163132) 2002 CU11	1.22	0.30	48.77	0.46 ± 0.02	0.41 ± 0.06	2002-2010	2.17 ± 1.70	11.3

Table 2.4 (cont'd)

NEA	a (AU)	e	i (deg)	D (km)	p_V	Arc	da/dt 10^{-4} AU/Myr	$\Delta\rho$ (km)
(140158) 2001 SX169	1.35	0.46	2.51	0.57 ± 0.01	0.29 ± 0.06	2001-2009	2.15 ± 1.59	9.6
(277039) 2005 CF41	1.65	0.59	15.89	0.68 ± 0.02	0.16 ± 0.03	2005-2011	2.12 ± 1.49	7.0
2010 EX119	1.90	0.60	15.57	0.56 ± 0.01	0.08 ± 0.01	2010-2010	2.10 ± 1.58	5.6
2010 FB81	2.58	0.60	9.48	0.32 ± 0.01	0.05 ± 0.01	118 days	2.10 ± 1.69	3.5
2009 VO24	1.55	0.46	6.05	0.47 ± 0.02	0.10 ± 0.02	2009-2011	2.08 ± 1.73	7.6
2010 JG88	1.37	0.38	30.61	0.46 ± 0.01	0.14 ± 0.02	2010-2010	2.08 ± 1.60	9.0
2010 GE25	2.07	0.47	21.65	0.30 ± 0.05	0.23 ± 0.10	40 days	2.05 ± 1.84	4.8
2010 JN33	1.72	0.34	55.30	0.29 ± 0.01	0.09 ± 0.02	4 days	2.05 ± 1.74	6.4
(262623) 2006 WY2	0.98	0.33	27.55	0.76 ± 0.08	0.12 ± 0.04	2006-2012	2.05 ± 1.55	14.7
2006 OD7	1.33	0.17	30.33	0.33 ± 0.07	0.27 ± 0.08	2006-2009	2.04 ± 1.71	9.3
(5604) 1992 FE	0.93	0.41	4.79	0.96 ± 0.01	0.52 ± 0.08	1985-2010	1.99 ± 1.33	15.6
2007 JZ20	1.31	0.34	40.48	0.48 ± 0.04	0.31 ± 0.07	2004-2010	1.97 ± 1.47	9.2
1998 OK1	1.36	0.43	13.99	0.56 ± 0.01	0.10 ± 0.02	1998-2010	1.96 ± 1.38	8.7
2010 AE	1.49	0.38	15.97	0.41 ± 0.00	0.18 ± 0.04	2010-2010	1.96 ± 1.74	7.6
(218017) 2001 XV266	1.20	0.19	12.00	0.45 ± 0.01	0.12 ± 0.03	2001-2010	1.95 ± 1.66	10.4
(302591) 2002 QE7	1.47	0.18	12.11	0.32 ± 0.06	0.34 ± 0.20	2002-2011	1.95 ± 1.93	7.7
2000 CO101	1.08	0.09	15.32	0.53 ± 0.16	0.11 ± 0.19	2000-2011	1.93 ± 1.61	12.1
2010 JE	2.78	0.66	13.90	0.41 ± 0.05	0.09 ± 0.03	194 days	1.93 ± 1.46	2.9
(238063) 2003 EG	1.74	0.71	31.75	1.47 ± 0.30	0.23 ± 0.13	1996-2010	1.92 ± 1.24	5.9
2005 ED318	1.85	0.45	2.39	0.20 ± 0.01	0.21 ± 0.04	2005-2010	1.87 ± 1.77	5.2
2010 FC81	2.67	0.63	1.68	0.40 ± 0.01	0.02 ± 0.00	97 days	1.87 ± 1.71	3.0
(65679) 1989 UQ	0.92	0.26	1.29	0.73 ± 0.18	0.06 ± 0.06	1954-2011	1.85 ± 1.59	14.8
2010 KB61	1.27	0.23	44.60	0.42 ± 0.01	0.06 ± 0.01	189 days	1.85 ± 1.51	9.0
(138911) 2001 AE2	1.35	0.08	1.66	0.34 ± 0.07	0.34 ± 0.22	1984-2012	1.83 ± 1.61	8.2
1998 SE36	1.34	0.10	11.68	0.34 ± 0.07	0.30 ± 0.22	1998-2009	1.83 ± 1.40	8.2
2009 XD	2.45	0.67	31.47	0.62 ± 0.02	0.15 ± 0.03	2009-2010	1.83 ± 1.30	3.3
2010 MF1	2.50	0.59	9.12	0.36 ± 0.00	0.18 ± 0.03	177 days	1.82 ± 1.35	3.2
(152889) 2000 CF59	1.68	0.64	41.59	1.02 ± 0.02	0.39 ± 0.07	1998-2010	1.79 ± 1.26	5.8
(154035) 2002 CV59	1.21	0.53	49.06	1.10 ± 0.12	0.15 ± 0.03	2002-2010	1.79 ± 1.26	9.4
(152978) 2000 GJ147	1.16	0.24	25.01	0.53 ± 0.01	0.11 ± 0.02	2000-2010	1.79 ± 1.40	10.0
2010 DW1	1.22	0.20	23.77	0.45 ± 0.00	0.09 ± 0.01	2002-2010	1.78 ± 1.36	9.2
(138937) 2001 BK16	2.07	0.68	31.83	0.92 ± 0.20	0.21 ± 0.06	1998-2010	1.78 ± 1.30	4.2
2010 HR80	1.35	0.50	26.71	0.78 ± 0.01	0.02 ± 0.00	2010-2010	1.77 ± 1.21	7.9

Table 2.4 (cont'd)

NEA	a (AU)	e	i (deg)	D (km)	p_V	Arc	da/dt 10^{-4} AU/Myr	$\Delta\rho$ (km)
2010 MR87	1.73	0.39	34.98	0.36 ± 0.06	0.22 ± 0.10	2003-2010	1.76 ± 1.36	5.4
2009 WC26	2.17	0.70	12.02	0.92 ± 0.01	0.23 ± 0.04	2007-2010	1.76 ± 1.23	3.8
2003 SL5	2.11	0.47	6.10	0.34 ± 0.07	0.38 ± 0.22	2003-2009	1.75 ± 1.72	4.0
2010 JM151	1.70	0.48	16.64	0.54 ± 0.02	0.09 ± 0.02	2010-2012	1.68 ± 1.30	5.3
2010 MU112	1.76	0.54	48.02	0.60 ± 0.02	0.03 ± 0.01	134 days	1.68 ± 1.23	5.0
2010 GZ6	1.40	0.14	44.84	0.37 ± 0.06	0.21 ± 0.07	2002-2010	1.67 ± 1.55	7.0
2010 NT1	1.46	0.22	39.52	0.38 ± 0.06	0.21 ± 0.08	99 days	1.67 ± 1.65	6.6
(105141) 2000 NF11	1.42	0.19	14.82	0.35 ± 0.05	0.43 ± 0.14	1978-2005	1.67 ± 1.20	6.9
(9162) Kwiila	1.50	0.60	9.02	1.13 ± 0.23	0.09 ± 0.04	1987-2009	1.66 ± 1.28	6.4
2010 FZ80	2.78	0.74	25.72	0.87 ± 0.01	0.02 ± 0.00	2010-2010	1.65 ± 1.14	2.5
2010 LF64	1.34	0.16	18.25	0.35 ± 0.01	0.03 ± 0.01	2 days	1.65 ± 1.40	7.4
2010 CP140	1.90	0.54	14.47	0.56 ± 0.10	0.11 ± 0.03	127 days	1.62 ± 1.19	4.3
2010 LT108	1.35	0.37	31.87	0.60 ± 0.01	0.06 ± 0.01	90 days	1.59 ± 1.33	7.1
(22099) 2000 EX106	1.10	0.28	9.84	0.62 ± 0.11	0.29 ± 0.16	1994-2008	1.58 ± 1.17	9.5
2003 QH5	1.26	0.22	17.61	0.54 ± 0.09	0.06 ± 0.03	2003-2010	1.58 ± 1.38	7.8
2009 ST103	2.69	0.72	15.94	0.85 ± 0.01	0.14 ± 0.02	2000-2010	1.57 ± 1.17	2.5
1999 TX2	1.28	0.46	61.39	0.96 ± 0.19	0.11 ± 0.03	1999-2005	1.57 ± 1.36	7.6
(52750) 1998 KK17	1.43	0.52	11.16	1.06 ± 0.01	0.39 ± 0.08	1992-2009	1.57 ± 1.01	6.4
2010 GU21	2.18	0.56	3.19	0.51 ± 0.04	0.02 ± 0.01	136 days	1.56 ± 1.20	3.4
(90373) 2003 SZ219	1.63	0.20	9.87	0.31 ± 0.05	0.58 ± 0.30	1998-2007	1.56 ± 1.28	5.3
(172974) 2005 YW55	1.64	0.25	8.47	0.34 ± 0.08	0.30 ± 0.24	2002-2011	1.55 ± 1.46	5.2
(280136) 2002 OM4	1.50	0.56	55.32	1.03 ± 0.20	0.30 ± 0.09	2002-2011	1.55 ± 1.18	5.9
1993 RA	1.92	0.42	5.61	0.36 ± 0.06	0.40 ± 0.23	1993-2010	1.54 ± 1.25	4.1
(10302) 1989 ML	1.27	0.14	4.38	0.24 ± 0.04	0.49 ± 0.28	1989-2006	1.53 ± 1.37	7.5
2010 FJ81	3.59	0.69	42.26	0.42 ± 0.01	0.05 ± 0.01	174 days	1.52 ± 1.31	1.6
2010 FY80	2.69	0.61	18.86	0.45 ± 0.01	0.12 ± 0.02	128 days	1.52 ± 1.17	2.4
(25143) Itokawa	1.32	0.28	1.62	0.45 ± 0.18	0.41 ± 0.20	1998-2010	1.50 ± 2.29	6.9
2000 GV147	1.75	0.46	10.57	0.50 ± 0.10	0.19 ± 0.12	2000-2009	1.50 ± 1.15	4.6
2010 CN1	1.50	0.44	20.97	0.64 ± 0.06	0.12 ± 0.04	2010-2011	1.49 ± 1.22	5.7
2010 DH77	3.27	0.71	34.37	0.58 ± 0.01	0.01 ± 0.00	107 days	1.49 ± 1.18	1.8
(226198) 2002 UN3	1.74	0.26	8.70	0.31 ± 0.05	0.67 ± 0.35	1994-2009	1.49 ± 1.30	4.5
(263976) 2009 KD5	1.05	0.26	13.47	0.78 ± 0.01	0.13 ± 0.02	1950-2012	1.47 ± 1.04	9.6
(164121) 2003 YT1	1.11	0.29	44.06	1.10 ± 0.08	0.49 ± 0.04	1982-2011	1.46 ± 1.04	8.8

Table 2.4 (cont'd)

NEA	a (AU)	e	i (deg)	D (km)	p_V	Arc	da/dt 10^{-4} AU/Myr	$\Delta\rho$ (km)
2001 HA4	2.68	0.80	17.20	1.85 ± 0.04	0.05 ± 0.01	2001-2010	1.44 ± 0.99	2.3
(215442) 2002 MQ3	0.91	0.27	36.28	1.05 ± 0.02	0.08 ± 0.00	2002-2009	1.44 ± 0.91	11.6
(42286) 2001 TN41	1.42	0.39	24.07	0.70 ± 0.20	1.00 ± 0.30	1975-2012	1.43 ± 1.23	5.9
2010 CH18	2.61	0.57	27.15	0.39 ± 0.01	0.26 ± 0.04	128 days	1.42 ± 1.17	2.4
2002 YF4	1.75	0.33	33.68	0.38 ± 0.01	0.43 ± 0.05	2002-2010	1.41 ± 1.07	4.2
2004 JX20	0.90	0.27	10.52	1.13 ± 0.01	0.02 ± 0.00	2004-2011	1.40 ± 1.02	11.4
(153220) 2000 YN29	2.53	0.68	5.87	0.81 ± 0.16	0.27 ± 0.09	1997-2009	1.40 ± 1.09	2.4
(152931) 2000 EA107	0.93	0.46	28.58	1.65 ± 0.04	0.24 ± 0.04	2000-2011	1.39 ± 0.86	10.9
2005 XD1	1.62	0.31	18.29	0.41 ± 0.01	0.18 ± 0.03	2005-2011	1.39 ± 1.13	4.7
(220124) 2002 TE66	1.46	0.38	51.34	0.61 ± 0.03	0.21 ± 0.04	2002-2009	1.37 ± 1.01	5.4
(99799) 2002 LJ3	1.46	0.28	7.56	0.49 ± 0.10	0.42 ± 0.25	1989-2012	1.34 ± 1.09	5.3
2009 UP1	1.52	0.40	17.28	0.61 ± 0.02	0.04 ± 0.01	95 days	1.34 ± 0.94	5.0
(242147) 2003 BH84	1.96	0.72	23.40	1.69 ± 0.01	0.11 ± 0.03	2003-2010	1.33 ± 0.88	3.4
2009 SX1	1.72	0.45	8.29	0.56 ± 0.01	0.17 ± 0.03	2002-2010	1.32 ± 1.09	4.1
2010 GH65	2.71	0.61	21.08	0.49 ± 0.02	0.24 ± 0.06	2001-2010	1.31 ± 1.18	2.1
(237551) 2000 WQ19	1.41	0.35	34.28	0.63 ± 0.04	0.23 ± 0.05	2000-2010	1.30 ± 0.97	5.5
(306462) 1999 RC32	1.84	0.43	30.97	0.48 ± 0.06	0.38 ± 0.09	1999-2010	1.30 ± 1.12	3.7
2010 BH2	2.35	0.46	24.62	0.36 ± 0.07	0.21 ± 0.10	149 days	1.29 ± 1.23	2.5
(6489) Golevka	2.50	0.61	2.28	0.53 ± 0.03	0.15 ± 0.02	1991-2011	1.25 ± 1.14	2.2
(9202) 1993 PB	1.42	0.61	40.82	1.62 ± 0.05	0.27 ± 0.06	1993-2009	1.25 ± 0.78	5.1
2010 HQ80	1.57	0.49	27.86	0.89 ± 0.15	0.02 ± 0.01	2010-2010	1.25 ± 1.11	4.4
(55532) 2001 WG2	1.79	0.70	38.50	1.96 ± 0.40	0.14 ± 0.04	1953-2006	1.24 ± 0.95	3.6
2010 LR33	1.69	0.46	5.83	0.66 ± 0.01	0.21 ± 0.04	2001-2012	1.23 ± 1.04	3.9
2008 EB9	1.56	0.22	21.35	0.43 ± 0.08	0.07 ± 0.04	2008-2010	1.23 ± 0.96	4.4
(4660) Nereus	1.49	0.36	1.43	0.40 ± 0.10	0.55 ± 0.17	1981-2010	1.23 ± 1.37	4.7
(161999) 1989 RC	2.31	0.52	7.39	0.46 ± 0.02	0.21 ± 0.04	1989-2010	1.20 ± 0.91	2.4
(152964) 2000 GP82	1.40	0.39	13.22	0.79 ± 0.15	0.34 ± 0.18	1995-2010	1.20 ± 0.88	5.1
2002 WP	1.45	0.22	19.15	0.52 ± 0.08	0.32 ± 0.13	2002-2010	1.19 ± 1.06	4.8
2010 GX62	2.95	0.70	21.64	0.79 ± 0.01	0.01 ± 0.00	180 days	1.17 ± 0.86	1.6
2006 EE1	1.20	0.28	36.40	0.78 ± 0.02	0.04 ± 0.01	2006-2010	1.17 ± 0.80	6.2
2009 AV	1.03	0.07	45.87	0.87 ± 0.02	0.15 ± 0.03	2009-2012	1.16 ± 0.90	7.7
(138359) 2000 GX127	1.14	0.36	20.24	1.08 ± 0.03	0.09 ± 0.02	2000-2010	1.15 ± 0.84	6.6
2009 SP	2.22	0.49	25.28	0.48 ± 0.10	0.12 ± 0.07	168 days	1.15 ± 1.03	2.4

Table 2.4 (cont'd)

NEA	a (AU)	e	i (deg)	D (km)	p_V	Arc	da/dt 10^{-4} AU/Myr	$\Delta\rho$ (km)
(159686) 2002 LB6	1.80	0.69	24.69	1.84 ± 0.01	0.17 ± 0.03	1997-2010	1.13 ± 0.68	3.3
2010 CG18	1.44	0.23	10.16	0.56 ± 0.02	0.02 ± 0.00	2010-2011	1.12 ± 0.94	4.6
2007 WV4	1.49	0.44	38.34	0.89 ± 0.16	0.04 ± 0.02	2007-2010	1.11 ± 0.85	4.3
2005 JA22	1.53	0.30	13.24	0.67 ± 0.17	0.16 ± 0.12	2005-2012	1.10 ± 1.07	4.0
2010 DM56	1.31	0.29	25.61	0.77 ± 0.00	0.02 ± 0.00	121 days	1.09 ± 0.84	5.1
(35107) 1991 VH	1.14	0.14	13.91	1.12 ± 0.23	0.27 ± 0.20	1991-2008	1.08 ± 0.92	6.2
2002 NW16	1.11	0.03	14.16	0.85 ± 0.01	0.16 ± 0.03	2002-2011	1.05 ± 0.87	6.3
(277616) 2006 BN6	2.56	0.71	18.38	1.24 ± 0.01	0.13 ± 0.03	2002-2010	1.04 ± 0.74	1.8
(137805) 1999 YK5	0.83	0.56	16.74	3.88 ± 0.16	0.03 ± 0.01	1999-2012	1.03 ± 0.57	9.5
(161989) Cacus	1.12	0.21	26.06	1.13 ± 0.07	0.20 ± 0.05	1978-2010	1.02 ± 0.85	6.0
2010 CD19	2.26	0.58	20.70	0.74 ± 0.01	0.25 ± 0.05	2009-2010	1.02 ± 0.84	2.1
(3671) Dionysus	2.20	0.54	13.55	0.89 ± 0.11	0.67 ± 0.37	1984-2011	1.02 ± 0.80	2.2
2002 NP1	1.25	0.17	19.12	0.81 ± 0.16	0.25 ± 0.08	2002-2010	1.02 ± 0.91	5.1
(1865) Cerberus	1.08	0.47	16.10	1.61 ± 0.01	0.14 ± 0.02	1971-2008	1.00 ± 0.68	6.3
(4197) 1982 TA	2.30	0.77	12.57	3.04 ± 0.16	0.28 ± 0.08	1954-2010	1.00 ± 0.62	2.0
2007 DK8	1.65	0.42	32.57	0.79 ± 0.16	0.08 ± 0.03	2007-2009	0.98 ± 0.86	3.2
(1915) Quetzalcoatl	2.54	0.57	20.41	0.75 ± 0.25	0.09 ± 0.09	1953-2004	0.97 ± 1.10	1.7
(3757) 1982 XB	1.83	0.45	3.87	0.50 ± 0.10	0.12 ± 0.13	1982-2008	0.97 ± 0.76	2.7
(235756) 2004 VC	1.13	0.26	39.15	1.14 ± 0.03	0.04 ± 0.01	1992-2010	0.96 ± 0.79	5.6
2010 DH56	2.24	0.57	33.65	0.77 ± 0.02	0.02 ± 0.01	44 days	0.95 ± 0.70	2.0
2010 KY39	1.74	0.40	25.51	0.68 ± 0.01	0.03 ± 0.00	167 days	0.94 ± 0.85	2.9
(162463) 2000 JH5	1.15	0.24	22.21	1.05 ± 0.08	0.16 ± 0.04	2000-2011	0.94 ± 0.75	5.4
2010 LG64	2.67	0.61	42.32	1.12 ± 0.49	0.01 ± 0.00	139 days	0.94 ± 2.30	1.5
2010 KZ117	2.27	0.51	33.16	0.62 ± 0.01	0.09 ± 0.02	166 days	0.93 ± 0.80	1.9
(177614) 2004 HK33	1.89	0.52	5.44	0.94 ± 0.18	0.19 ± 0.14	2001-2009	0.93 ± 0.74	2.5
(7335) 1989 JA	1.77	0.48	15.21	0.93 ± 0.15	0.32 ± 0.15	1989-2008	0.93 ± 0.91	2.8
2010 JL33	2.66	0.74	5.33	1.78 ± 0.03	0.05 ± 0.01	1997-2011	0.93 ± 0.71	1.5
2004 RA11	1.82	0.40	39.36	0.63 ± 0.06	0.14 ± 0.04	2004-2010	0.92 ± 0.78	2.6
(175706) 1996 FG3	1.05	0.35	1.99	1.90 ± 0.52	0.03 ± 0.03	1996-2012	0.92 ± 0.73	5.9
(68359) 2001 OZ13	1.52	0.17	9.86	0.62 ± 0.15	0.42 ± 0.27	1995-2010	0.90 ± 0.69	3.4
(283729) 2002 UX	1.47	0.16	20.21	0.65 ± 0.13	0.31 ± 0.10	2002-2012	0.90 ± 0.84	3.5
(153814) 2001 WN5	1.71	0.47	1.92	0.93 ± 0.01	0.10 ± 0.02	1996-2010	0.89 ± 0.74	2.8
(7822) 1991 CS	1.12	0.16	37.12	1.44 ± 0.01	0.09 ± 0.01	1991-2010	0.89 ± 0.66	5.2

Table 2.4 (cont'd)

NEA	a (AU)	e	i (deg)	D (km)	p_V	Arc	da/dt 10^{-4} AU/Myr	$\Delta\rho$ (km)
(142464) 2002 TC9	1.23	0.15	16.28	0.89 ± 0.01	0.12 ± 0.02	1991-2006	0.88 ± 0.73	4.5
2005 WE	1.15	0.25	12.36	1.15 ± 0.01	0.02 ± 0.00	2005-2011	0.88 ± 0.68	5.0
2010 JF87	2.44	0.62	24.93	0.94 ± 0.01	0.04 ± 0.01	65 days	0.86 ± 0.66	1.6
(222869) 2002 FB6	1.80	0.54	33.70	1.20 ± 0.24	0.14 ± 0.03	2002-2009	0.85 ± 0.72	2.5
1989 AZ	1.65	0.47	11.78	1.09 ± 0.20	0.03 ± 0.02	1989-2008	0.85 ± 0.69	2.8
(90367) 2003 LC5	1.16	0.43	16.88	1.75 ± 0.00	0.05 ± 0.01	1983-2008	0.85 ± 0.57	4.8
2010 KK127	2.23	0.42	6.94	0.50 ± 0.02	0.03 ± 0.01	177 days	0.84 ± 0.65	1.8
(5143) Heracles	1.83	0.77	9.03	4.84 ± 0.38	0.23 ± 0.05	1953-2011	0.83 ± 0.48	2.3
(242187) 2003 KR18	2.34	0.48	5.58	0.65 ± 0.13	0.29 ± 0.15	1985-2010	0.82 ± 1.64	1.6
(311321) 2005 NP1	1.83	0.30	34.70	0.58 ± 0.11	0.17 ± 0.09	2005-2012	0.82 ± 0.70	2.3
2010 HD33	2.62	0.52	24.48	0.56 ± 0.10	0.27 ± 0.13	134 days	0.80 ± 0.63	1.3
(10115) 1992 SK	1.25	0.32	15.32	1.00 ± 0.08	0.28 ± 0.14	1953-1999	0.80 ± 0.68	4.0
(185716) 1998 SF35	1.69	0.27	35.19	0.63 ± 0.10	0.34 ± 0.15	1998-2009	0.80 ± 0.62	2.6
2007 RM133	2.21	0.44	10.75	0.59 ± 0.08	0.27 ± 0.08	2007-2010	0.80 ± 0.66	1.7
(254419) 2004 VT60	2.08	0.43	43.53	0.63 ± 0.02	0.41 ± 0.09	2001-2010	0.79 ± 0.62	1.9
(7839) 1994 ND	2.16	0.52	27.18	0.78 ± 0.01	0.18 ± 0.03	1994-2010	0.79 ± 0.57	1.7
2003 WO7	2.15	0.43	7.67	0.68 ± 0.16	0.11 ± 0.07	2003-2009	0.79 ± 0.77	1.7
2004 TB18	1.82	0.45	13.20	0.86 ± 0.01	0.20 ± 0.04	2004-2011	0.78 ± 0.62	2.2
(137062) 1998 WM	1.22	0.32	22.52	1.27 ± 0.04	0.28 ± 0.07	1987-2010	0.77 ± 0.53	4.0
2010 FX80	2.17	0.45	36.94	0.68 ± 0.13	0.02 ± 0.01	84 days	0.77 ± 0.73	1.7
2006 AD	1.05	0.49	54.98	3.06 ± 0.61	0.04 ± 0.02	2006-2009	0.75 ± 0.53	4.9
2010 GY6	1.29	0.23	21.91	1.10 ± 0.08	0.03 ± 0.01	240 days	0.74 ± 0.68	3.6
2005 SC71	1.91	0.38	32.37	0.74 ± 0.15	0.15 ± 0.11	2005-2010	0.74 ± 0.71	2.0
2002 HF8	2.32	0.49	4.78	0.71 ± 0.16	0.18 ± 0.14	2002-2009	0.73 ± 0.66	1.5
2009 WN	1.38	0.22	32.79	0.95 ± 0.04	0.06 ± 0.01	2002-2010	0.73 ± 0.59	3.1
(315508) 2008 AB31	1.60	0.32	30.02	0.82 ± 0.05	0.02 ± 0.01	2002-2012	0.72 ± 0.62	2.5
(29075) 1950 DA	1.70	0.51	12.18	2.00 ± 0.20	0.07 ± 0.02	1950-2012	0.71 ± 0.54	2.2
(89959) 2002 NT7	1.74	0.53	42.33	1.41 ± 0.08	0.22 ± 0.05	1954-2011	0.71 ± 0.51	2.2
(142563) 2002 TR69	1.66	0.34	20.49	0.86 ± 0.14	0.38 ± 0.17	1997-2012	0.70 ± 0.56	2.3
2010 OK126	1.96	0.45	52.54	0.85 ± 0.01	0.01 ± 0.00	129 days	0.70 ± 0.61	1.8
(162903) 2001 JV2	1.30	0.24	47.49	1.09 ± 0.01	0.06 ± 0.02	2001-2010	0.69 ± 0.55	3.3
2003 UL12	3.29	0.70	19.73	1.08 ± 0.02	0.20 ± 0.05	1998-2010	0.69 ± 0.50	0.8
(139345) 2001 KA67	1.80	0.70	22.37	3.10 ± 0.14	0.04 ± 0.01	2001-2010	0.68 ± 0.47	2.0

Table 2.4 (cont'd)

NEA	a (AU)	e	i (deg)	D (km)	p_V	Arc	da/dt 10^{-4} AU/Myr	$\Delta\rho$ (km)
(3908) Nyx	1.93	0.46	2.18	1.00 ± 0.15	0.16 ± 0.08	1980-2009	0.67 ± 0.54	1.7
(2102) Tantalus	1.29	0.30	64.01	1.81 ± 0.22	0.21 ± 0.08	1975-2008	0.66 ± 0.51	3.2
2010 EH43	1.28	0.04	37.55	0.99 ± 0.02	0.05 ± 0.01	2010-2010	0.66 ± 0.52	3.2
(2100) Ra-Shalom	0.83	0.44	15.76	2.30 ± 0.20	0.13 ± 0.03	1975-2009	0.66 ± 0.47	6.1
2007 HX4	1.32	0.33	56.56	1.39 ± 0.04	0.07 ± 0.01	1998-2010	0.65 ± 0.52	3.0
(212546) 2006 SV19	2.13	0.51	7.34	1.06 ± 0.23	0.13 ± 0.11	2003-2009	0.65 ± 0.66	1.5
(66272) 1999 JW6	1.51	0.14	51.32	0.82 ± 0.01	0.42 ± 0.06	1999-2007	0.64 ± 0.58	2.4
(243566) 1995 SA	2.46	0.64	20.06	1.46 ± 0.18	0.09 ± 0.03	1991-2010	0.64 ± 0.54	1.2
(15745) 1991 PM5	1.72	0.25	14.42	0.80 ± 0.20	0.23 ± 0.07	1982-2007	0.63 ± 0.55	2.0
(103067) 1999 XA143	1.84	0.58	38.54	1.28 ± 0.03	0.25 ± 0.05	1994-2010	0.63 ± 0.48	1.8
(85628) 1998 KV2	1.59	0.33	13.03	1.01 ± 0.06	0.30 ± 0.08	1998-2012	0.62 ± 0.48	2.2
(2101) Adonis	1.87	0.76	1.33	5.73 ± 0.39	0.04 ± 0.01	1936-2007	0.61 ± 0.36	1.7
(66251) 1999 GJ2	1.54	0.20	11.28	1.22 ± 0.23	0.19 ± 0.09	1984-2012	0.61 ± 0.50	2.2
2000 HD74	2.92	0.59	49.30	0.83 ± 0.02	0.16 ± 0.03	2000-2010	0.60 ± 0.54	0.8
2000 JA3	2.25	0.46	10.18	0.77 ± 0.15	0.10 ± 0.06	2000-2010	0.60 ± 0.47	1.2
(4953) 1990 MU	1.62	0.66	24.39	2.26 ± 0.50	0.79 ± 0.25	1974-2009	0.60 ± 0.44	2.0
2009 XC2	2.64	0.58	25.77	0.97 ± 0.01	0.26 ± 0.03	1954-2010	0.60 ± 0.46	1.0
(40263) 1999 FQ5	1.49	0.16	25.84	0.95 ± 0.19	0.18 ± 0.08	1994-2012	0.60 ± 0.54	2.3
(12711) Tukmit	1.19	0.27	38.48	1.90 ± 0.40	0.19 ± 0.06	1991-2009	0.60 ± 0.47	3.3
(8566) 1996 EN	1.51	0.43	37.96	1.57 ± 0.26	0.22 ± 0.11	1996-2011	0.60 ± 0.46	2.3
(66008) 1998 QH2	1.43	0.36	61.01	1.48 ± 0.28	0.32 ± 0.17	1996-2008	0.59 ± 0.49	2.4
(2212) Hephaistos	2.16	0.84	11.69	5.54 ± 0.04	0.16 ± 0.03	1978-2011	0.58 ± 0.35	1.3
(215757) 2004 FU64	1.84	0.37	24.88	0.91 ± 0.18	0.19 ± 0.06	1999-2009	0.58 ± 0.47	1.6
(7888) 1993 UC	2.43	0.66	26.08	2.75 ± 0.60	0.18 ± 0.06	1989-2008	0.58 ± 0.48	1.1
(17182) 1999 VU	1.39	0.55	9.27	2.88 ± 0.19	0.03 ± 0.01	1977-2007	0.58 ± 0.39	2.5
(138847) 2000 VE62	1.62	0.29	22.19	0.97 ± 0.15	0.40 ± 0.15	1983-2012	0.58 ± 0.48	2.0
(3554) Amun	0.97	0.28	23.36	3.33 ± 0.02	0.08 ± 0.01	1986-2012	0.57 ± 0.39	4.1
(17188) 1999 WC2	2.22	0.64	29.41	1.82 ± 0.23	0.15 ± 0.04	1990-2011	0.57 ± 0.39	1.2
(87311) 2000 QJ1	1.59	0.51	7.69	1.95 ± 0.14	0.14 ± 0.04	1982-2011	0.57 ± 0.45	2.0
(218863) 2006 WO127	2.19	0.55	11.00	1.24 ± 0.01	0.39 ± 0.09	2002-2010	0.57 ± 0.45	1.2
(1864) Daedalus	1.46	0.61	22.20	2.72 ± 0.11	0.27 ± 0.06	1971-2006	0.57 ± 0.40	2.2
(138883) 2000 YL29	1.54	0.34	21.89	1.22 ± 0.22	0.25 ± 0.12	1984-2011	0.56 ± 0.50	2.1
(138013) 2000 CN101	1.60	0.63	15.95	3.52 ± 0.23	0.17 ± 0.05	1984-2012	0.55 ± 0.41	1.9

Table 2.4 (cont'd)

NEA	a (AU)	e	i (deg)	D (km)	p_V	Arc	da/dt 10^{-4} AU/Myr	$\Delta\rho$ (km)
(100004) 1983 VA	2.60	0.70	16.29	2.70 ± 0.10	0.07 ± 0.01	1983-2005	0.55 ± 0.40	0.9
2000 JY8	2.78	0.60	16.53	1.11 ± 0.22	0.32 ± 0.09	2000-2009	0.54 ± 0.45	0.8
(12538) 1998 OH	1.54	0.41	24.53	1.66 ± 0.33	0.23 ± 0.12	1991-2010	0.54 ± 0.47	2.0
2010 AG79	2.91	0.58	32.97	0.89 ± 0.01	0.02 ± 0.00	70 days	0.53 ± 0.43	0.8
2010 VY190	1.81	0.31	19.97	0.95 ± 0.22	0.04 ± 0.02	2010-2011	0.52 ± 0.43	1.5
(11500) Tomaiyowit	1.08	0.36	10.31	0.74 ± 0.01	0.14 ± 0.02	1989-2007	0.52 ± 0.36	3.2
2005 CR37	1.91	0.47	26.07	1.20 ± 0.24	0.03 ± 0.02	2005-2010	0.51 ± 0.38	1.4
2010 LQ33	2.27	0.46	24.60	0.87 ± 0.01	0.04 ± 0.01	164 days	0.51 ± 0.45	1.0
(40329) 1999 ML	2.27	0.45	2.51	0.96 ± 0.23	0.16 ± 0.16	1999-2009	0.50 ± 0.43	1.0
2009 UV18	3.17	0.63	8.34	1.00 ± 0.00	0.71 ± 0.10	2004-2010	0.50 ± 0.36	0.6
(243147) 2007 TX18	2.14	0.42	7.37	0.91 ± 0.01	0.28 ± 0.06	1991-2012	0.50 ± 0.43	1.1
2007 XC10	1.62	0.23	47.94	1.05 ± 0.20	0.03 ± 0.01	2007-2011	0.50 ± 0.45	1.7
(162181) 1999 LF6	1.41	0.28	18.94	0.86 ± 0.16	0.13 ± 0.09	1999-2010	0.49 ± 0.43	2.1
(16834) 1997 WU22	1.47	0.44	15.99	1.50 ± 0.30	0.40 ± 0.12	1988-2012	0.49 ± 0.43	1.9
(144901) 2004 WG1	1.64	0.52	13.06	2.24 ± 0.03	0.04 ± 0.01	2004-2012	0.48 ± 0.34	1.6
(68372) 2001 PM9	1.62	0.42	8.10	1.73 ± 0.45	0.02 ± 0.02	2001-2011	0.48 ± 0.44	1.6
(159402) 1999 AP10	2.38	0.58	7.63	1.20 ± 0.30	0.34 ± 0.23	1999-2009	0.48 ± 0.44	0.9
(2201) Oljato	2.17	0.71	2.52	1.80 ± 0.10	0.43 ± 0.03	1931-2012	0.48 ± 0.40	1.0
(52760) 1998 ML14	2.41	0.62	2.43	1.00 ± 0.05	0.27 ± 0.24	1998-2003	0.47 ± 0.39	0.9
(159399) 1998 UL1	1.53	0.21	41.97	1.24 ± 0.25	0.27 ± 0.09	1998-2011	0.47 ± 0.41	1.7
(88188) 2000 XH44	2.01	0.39	11.37	1.37 ± 0.26	0.37 ± 0.17	1991-2011	0.46 ± 0.37	1.1
2010 KH	2.76	0.55	14.57	1.03 ± 0.02	0.03 ± 0.01	222 days	0.45 ± 0.41	0.7
(3103) Eger	1.40	0.35	20.93	1.80 ± 0.30	0.39 ± 0.12	1982-2012	0.45 ± 0.41	1.9
(85713) 1998 SS49	1.92	0.64	10.76	3.48 ± 0.79	0.08 ± 0.04	1998-2011	0.44 ± 0.37	1.2
(232382) 2003 BT47	2.34	0.49	7.49	1.12 ± 0.00	0.16 ± 0.02	2003-2011	0.44 ± 0.38	0.9
2010 AB78	2.25	0.55	33.24	1.52 ± 0.01	0.04 ± 0.00	2003-2010	0.43 ± 0.35	0.9
(155334) 2006 DZ169	2.03	0.41	6.62	1.15 ± 0.32	0.20 ± 0.18	1983-2011	0.43 ± 0.36	1.0
2002 LV	2.32	0.60	29.53	1.73 ± 0.35	0.15 ± 0.05	2002-2012	0.43 ± 0.38	0.9
(7350) 1993 VA	1.36	0.39	7.26	2.36 ± 0.13	0.05 ± 0.01	1986-2008	0.43 ± 0.36	1.9
(54401) 2000 LM	1.71	0.26	18.95	1.19 ± 0.19	0.18 ± 0.07	1989-2009	0.42 ± 0.38	1.3
(54686) 2001 DU8	1.78	0.34	33.21	1.25 ± 0.25	0.34 ± 0.09	1988-2011	0.42 ± 0.33	1.3
(85839) 1998 YO4	1.65	0.25	9.33	1.14 ± 0.01	0.41 ± 0.08	1993-2012	0.42 ± 0.34	1.4
2010 MU111	2.40	0.61	41.36	1.95 ± 0.01	0.02 ± 0.00	167 days	0.42 ± 0.36	0.8

Table 2.4 (cont'd)

NEA	a (AU)	e	i (deg)	D (km)	p_V	Arc	da/dt 10^{-4} AU/Myr	$\Delta\rho$ (km)
2010 CM	2.62	0.54	7.42	1.17 ± 0.23	0.06 ± 0.01	2002-2010	0.42 ± 0.39	0.7
(86067) 1999 RM28	1.82	0.32	30.54	1.25 ± 0.21	0.31 ± 0.13	1989-2011	0.42 ± 0.35	1.2
2000 WC67	2.69	0.57	10.00	1.31 ± 0.02	0.04 ± 0.01	2000-2010	0.42 ± 0.36	0.7
(159608) 2002 AC2	1.67	0.35	58.88	1.51 ± 0.30	0.20 ± 0.06	2002-2011	0.42 ± 0.36	1.3
(230118) 2001 DB3	2.69	0.56	24.48	1.18 ± 0.00	0.15 ± 0.02	2001-2010	0.42 ± 0.30	0.7
2005 LY19	1.60	0.24	30.00	1.36 ± 0.27	0.26 ± 0.08	2005-2011	0.41 ± 0.35	1.4
2009 KC3	3.21	0.70	10.01	2.19 ± 0.45	0.02 ± 0.02	2009-2010	0.40 ± 0.33	0.5
2010 NW1	3.39	0.62	39.55	1.16 ± 0.23	0.19 ± 0.10	109 days	0.40 ± 0.40	0.4
(230979) 2005 AT42	2.86	0.61	11.23	1.52 ± 0.04	0.21 ± 0.05	2004-2010	0.39 ± 0.32	0.6
(86326) 1999 WK13	1.84	0.36	34.30	1.35 ± 0.03	0.10 ± 0.02	1979-2011	0.38 ± 0.29	1.1
2004 YR32	3.06	0.70	20.52	2.29 ± 0.28	0.03 ± 0.01	2004-2010	0.38 ± 0.29	0.5
(153219) 2000 YM29	2.09	0.44	40.33	1.29 ± 0.01	0.05 ± 0.01	2000-2010	0.38 ± 0.33	0.9
(1943) Anteros	1.43	0.26	8.71	2.40 ± 0.30	0.15 ± 0.05	1973-2012	0.38 ± 0.34	1.5
(12923) Zephyr	1.96	0.49	5.29	2.06 ± 0.01	0.20 ± 0.03	1955-2012	0.36 ± 0.32	0.9
(152558) 1990 SA	2.01	0.44	38.12	1.46 ± 0.01	0.16 ± 0.02	1990-2007	0.36 ± 0.29	0.9
2002 XG4	2.26	0.48	21.03	1.42 ± 0.04	0.05 ± 0.01	2002-2010	0.36 ± 0.26	0.7
2010 NG3	2.61	0.56	26.97	1.52 ± 0.04	0.10 ± 0.02	186 days	0.35 ± 0.29	0.6
2010 AH30	2.29	0.55	43.27	1.86 ± 0.15	0.02 ± 0.00	59 days	0.35 ± 0.27	0.7
(214088) 2004 JN13	2.87	0.70	13.33	2.97 ± 0.64	0.25 ± 0.08	1975-2009	0.35 ± 0.26	0.5
(68350) 2001 MK3	1.67	0.25	29.56	1.79 ± 0.33	0.22 ± 0.11	1955-2007	0.34 ± 0.32	1.1
2003 UN12	2.16	0.40	6.91	1.25 ± 0.25	0.05 ± 0.02	2003-2012	0.34 ± 0.25	0.8
(8201) 1994 AH2	2.54	0.71	9.56	1.86 ± 0.18	0.15 ± 0.04	1981-2010	0.34 ± 0.27	0.6
(85818) 1998 XM4	1.66	0.42	62.72	2.22 ± 0.02	0.21 ± 0.03	1993-2012	0.33 ± 0.29	1.1
(27346) 2000 DN8	1.87	0.40	36.95	1.75 ± 0.10	0.26 ± 0.04	1978-2011	0.33 ± 0.29	0.9
(247156) 2000 YH29	2.22	0.53	21.84	1.97 ± 0.21	0.03 ± 0.01	2000-2010	0.32 ± 0.27	0.7
(153271) 2001 CL42	1.56	0.40	21.65	2.44 ± 0.17	0.04 ± 0.01	2001-2011	0.32 ± 0.22	1.1
(241596) 1998 XM2	1.80	0.34	27.10	1.56 ± 0.02	0.10 ± 0.02	1952-2011	0.31 ± 0.23	0.9
2006 JT	2.40	0.48	36.42	1.52 ± 0.32	0.02 ± 0.01	2006-2010	0.31 ± 0.28	0.6
(85804) 1998 WQ5	1.72	0.35	27.66	2.37 ± 0.44	0.24 ± 0.09	1989-2011	0.30 ± 0.24	0.9
(5653) Camarillo	1.79	0.30	6.87	1.54 ± 0.02	0.27 ± 0.06	1974-2012	0.30 ± 0.23	0.9
2010 LO97	2.58	0.53	21.66	1.63 ± 0.31	0.02 ± 0.01	182 days	0.29 ± 0.26	0.5
2009 WF104	3.07	0.66	17.00	2.23 ± 0.03	0.05 ± 0.01	2009-2010	0.29 ± 0.22	0.4
(153249) 2001 BW15	2.12	0.59	41.21	3.16 ± 0.73	0.18 ± 0.11	1989-2010	0.29 ± 0.21	0.7

Table 2.4 (cont'd)

NEA	a (AU)	e	i (deg)	D (km)	p_V	Arc	da/dt 10^{-4} AU/Myr	$\Delta\rho$ (km)
(154029) 2002 CY46	1.89	0.46	44.16	2.23 ± 0.05	0.10 ± 0.02	2002-2010	0.29 ± 0.24	0.8
(159518) 2001 FF7	2.10	0.44	47.51	1.78 ± 0.03	0.04 ± 0.01	2001-2010	0.28 ± 0.23	0.6
(52387) 1993 OM7	1.28	0.19	24.15	1.22 ± 0.25	0.09 ± 0.03	1993-2009	0.28 ± 0.24	1.4
(153842) 2001 XT30	2.74	0.57	9.07	1.76 ± 0.11	0.19 ± 0.04	2000-2011	0.28 ± 0.24	0.4
(217807) 2000 XK44	1.72	0.39	11.24	0.73 ± 0.14	0.28 ± 0.18	1975-2009	0.28 ± 0.25	0.9
(162038) 1996 DH	1.59	0.28	17.23	1.96 ± 0.22	0.11 ± 0.03	1996-2012	0.28 ± 0.20	1.0
(85709) 1998 SG36	1.65	0.34	24.84	2.23 ± 0.14	0.14 ± 0.03	1998-2012	0.27 ± 0.24	0.9
2005 QL	2.45	0.50	10.71	1.85 ± 0.44	0.02 ± 0.01	2005-2010	0.27 ± 0.25	0.5
2010 EH20	2.62	0.52	23.89	1.80 ± 0.39	0.03 ± 0.03	2010-2010	0.27 ± 0.24	0.4
(36183) 1999 TX16	1.55	0.33	38.22	2.30 ± 0.11	0.09 ± 0.02	1997-2008	0.26 ± 0.21	1.0
(11066) Sigurd	1.39	0.38	36.89	2.78 ± 0.12	0.19 ± 0.03	1992-2012	0.26 ± 0.23	1.1
(1620) Geographos	1.25	0.34	13.34	3.90 ± 0.40	0.19 ± 0.02	1951-2012	0.26 ± 0.22	1.3
(4183) Cuno	1.98	0.63	6.70	5.62 ± 0.46	0.10 ± 0.02	1986-2012	0.26 ± 0.20	0.7
(3199) Nefertiti	1.57	0.28	32.97	3.10 ± 0.90	0.10 ± 0.10	1982-2011	0.26 ± 0.24	0.9
(5620) Jasonwheeler	2.16	0.42	7.86	1.80 ± 0.50	0.09 ± 0.09	1955-2011	0.25 ± 0.21	0.6
(304153) 2006 OU10	1.75	0.35	33.70	2.05 ± 0.02	0.03 ± 0.01	2006-2011	0.25 ± 0.19	0.8
(108519) 2001 LF	1.60	0.27	16.39	2.31 ± 0.46	0.02 ± 0.01	1989-2011	0.25 ± 0.20	0.9
(234061) 1999 HE1	2.36	0.57	8.17	2.90 ± 0.02	0.02 ± 0.00	1999-2010	0.24 ± 0.18	0.5
2004 EB	3.13	0.66	21.36	2.54 ± 0.24	0.04 ± 0.01	1999-2010	0.24 ± 0.19	0.3
2001 RX11	2.77	0.54	13.05	1.82 ± 0.04	0.04 ± 0.01	2001-2010	0.24 ± 0.19	0.4
(1863) Antinous	2.26	0.61	18.40	3.23 ± 0.60	0.10 ± 0.03	1948-2009	0.24 ± 0.22	0.5
(5645) 1990 SP	1.35	0.39	13.51	1.67 ± 0.02	0.12 ± 0.02	1974-2009	0.24 ± 0.18	1.1
(285263) 1998 QE2	2.42	0.57	12.85	2.75 ± 0.55	0.06 ± 0.02	1998-2009	0.24 ± 0.18	0.4
(276049) 2002 CE26	2.23	0.56	47.31	3.33 ± 0.95	0.03 ± 0.03	2001-2010	0.23 ± 0.21	0.5
2010 LR68	3.03	0.61	4.58	2.25 ± 0.15	0.02 ± 0.00	2006-2011	0.23 ± 0.21	0.3
(4957) Brucemurray	1.57	0.22	35.01	3.10 ± 0.60	0.17 ± 0.06	1976-2003	0.23 ± 0.20	0.8
(138925) 2001 AU43	1.90	0.38	72.13	2.41 ± 0.50	0.11 ± 0.03	2001-2009	0.22 ± 0.19	0.6
(5731) Zeus	2.26	0.65	11.43	5.23 ± 0.69	0.03 ± 0.01	1988-2006	0.22 ± 0.15	0.5
(275611) 1999 XX262	1.53	0.18	8.23	2.43 ± 0.18	0.02 ± 0.01	1974-2010	0.22 ± 0.20	0.8
(9950) ESA	2.44	0.53	14.59	2.50 ± 0.50	0.10 ± 0.03	1990-2009	0.22 ± 0.21	0.4
(20460) Robwhiteley	1.88	0.41	33.94	2.72 ± 0.59	0.20 ± 0.14	1954-2009	0.22 ± 0.18	0.6
(1685) Toro	1.37	0.44	9.38	3.79 ± 0.04	0.25 ± 0.04	1948-2010	0.21 ± 0.18	0.9
(248590) 2006 CS	2.91	0.70	52.30	4.73 ± 0.84	0.02 ± 0.01	1996-2011	0.21 ± 0.18	0.3

Table 2.4 (cont'd)

NEA	a (AU)	e	i (deg)	D (km)	p_V	Arc	da/dt 10^{-4} AU/Myr	$\Delta\rho$ (km)
(6455) 1992 HE	2.24	0.57	37.36	4.63 ± 0.41	0.23 ± 0.05	1989-2012	0.21 ± 0.17	0.4
(3122) Florence	1.77	0.42	22.16	4.40 ± 0.03	0.23 ± 0.05	1979-2012	0.20 ± 0.16	0.6
(162998) 2001 SK162	1.93	0.47	1.68	0.87 ± 0.01	0.16 ± 0.03	1993-2009	0.20 ± 0.16	0.5
(248926) 2006 WZ2	1.69	0.33	24.66	2.91 ± 0.23	0.04 ± 0.01	1998-2010	0.20 ± 0.18	0.6
(11398) 1998 YP11	1.72	0.39	15.02	1.32 ± 0.35	0.32 ± 0.10	1983-2012	0.19 ± 0.21	0.6
(4486) Mithra	2.20	0.66	3.04	1.85 ± 0.02	0.30 ± 0.06	1987-2011	0.19 ± 0.17	0.4
(6178) 1986 DA	2.82	0.58	4.31	3.20 ± 0.21	0.16 ± 0.03	1977-2010	0.19 ± 0.17	0.3
(248083) 2004 QU24	3.32	0.61	23.34	2.36 ± 0.51	0.13 ± 0.07	1993-2011	0.19 ± 0.16	0.2
(5626) 1991 FE	2.20	0.45	3.85	3.96 ± 1.22	0.15 ± 0.15	1970-2011	0.19 ± 0.19	0.4
(100085) 1992 UY4	2.64	0.63	2.80	2.60 ± 0.70	0.02 ± 0.02	1979-2006	0.19 ± 0.17	0.3
(1866) Sisyphus	1.89	0.54	41.19	6.60 ± 0.19	0.26 ± 0.05	1955-2012	0.18 ± 0.12	0.5
2001 RC12	3.22	0.64	27.33	3.20 ± 0.40	0.08 ± 0.02	2001-2007	0.17 ± 0.16	0.2
2009 XE11	3.31	0.61	14.07	2.72 ± 0.02	0.04 ± 0.01	1997-2010	0.17 ± 0.16	0.2
(4015) Wilson-Harrington	2.64	0.62	2.78	3.82 ± 0.03	0.05 ± 0.01	1949-2011	0.17 ± 0.13	0.3
(152679) 1998 KU2	2.25	0.55	4.92	4.69 ± 1.18	0.02 ± 0.01	1998-2010	0.16 ± 0.24	0.3
2009 WO6	3.09	0.58	28.76	2.49 ± 0.01	0.03 ± 0.01	121 days	0.16 ± 0.14	0.2
2010 LF86	2.41	0.46	13.54	2.51 ± 0.20	0.03 ± 0.01	2010-2011	0.16 ± 0.13	0.3
(5646) 1990 TR	2.14	0.44	7.91	2.72 ± 0.53	0.45 ± 0.19	1990-2006	0.16 ± 0.13	0.3
(163691) 2003 BB43	2.41	0.52	40.89	3.45 ± 0.54	0.02 ± 0.01	1988-2007	0.15 ± 0.13	0.3
(2368) Beltrovata	2.10	0.41	5.24	3.00 ± 0.49	0.16 ± 0.08	1977-2012	0.14 ± 0.13	0.3
(4055) Magellan	1.82	0.33	23.24	2.78 ± 0.15	0.33 ± 0.07	1985-2012	0.14 ± 0.10	0.4
(96189) Pygmalion	1.82	0.31	13.99	3.61 ± 0.16	0.04 ± 0.01	1986-2011	0.13 ± 0.10	0.4
(162566) 2000 RJ34	2.63	0.57	13.85	4.33 ± 0.10	0.07 ± 0.01	2000-2010	0.13 ± 0.09	0.2
(6050) Miwablock	2.20	0.44	6.40	3.54 ± 0.88	0.19 ± 0.15	1953-2012	0.12 ± 0.11	0.3
(5587) 1990 SB	2.39	0.55	18.10	4.86 ± 0.85	0.25 ± 0.11	1953-2012	0.12 ± 0.11	0.2
(3752) Camillo	1.41	0.30	55.55	2.31 ± 0.09	0.21 ± 0.04	1976-2003	0.12 ± 0.11	0.5
(20826) 2000 UV13	2.42	0.63	31.87	5.10 ± 1.00	0.27 ± 0.09	1953-2012	0.11 ± 0.10	0.2
(54789) 2001 MZ7	1.78	0.29	24.46	1.57 ± 0.02	0.86 ± 0.14	1978-2011	0.11 ± 0.10	0.3
(52762) 1998 MT24	2.42	0.65	33.88	6.74 ± 0.19	0.05 ± 0.01	1953-2008	0.10 ± 0.08	0.2
(5370) Taranis	3.33	0.63	19.09	5.33 ± 0.08	0.04 ± 0.01	1986-2011	0.10 ± 0.09	0.1
(19764) 2000 NF5	2.23	0.44	1.33	1.57 ± 0.07	0.34 ± 0.08	1990-2012	0.09 ± 0.08	0.2
(88263) 2001 KQ1	2.10	0.43	38.83	5.71 ± 0.03	0.04 ± 0.01	1998-2008	0.09 ± 0.07	0.2
(1580) Betulia	2.20	0.49	52.11	5.39 ± 0.54	0.08 ± 0.01	1950-2010	0.09 ± 0.07	0.2

Table 2.4 (cont'd)

NEA	a (AU)	e	i (deg)	D (km)	p_V	Arc	da/dt 10^{-4} AU/Myr	$\Delta\rho$ (km)
(17274) 2000 LC16	2.72	0.56	5.62	3.18 ± 0.11	0.04 ± 0.01	1955-2011	0.08 ± 0.07	0.1
(1980) Tezcatlipoca	1.71	0.36	26.86	5.99 ± 0.08	0.14 ± 0.02	1950-2012	0.08 ± 0.07	0.3
(26760) 2001 KP41	2.87	0.55	10.91	5.40 ± 0.37	0.04 ± 0.01	1996-2011	0.08 ± 0.06	0.1
(25916) 2001 CP44	2.56	0.50	15.75	5.68 ± 0.03	0.26 ± 0.05	1973-2012	0.07 ± 0.06	0.1
(143651) 2003 QO104	2.13	0.53	11.62	2.29 ± 0.54	0.14 ± 0.14	1981-2012	0.07 ± 0.07	0.2
(1627) Ivar	1.86	0.40	8.45	8.37 ± 0.08	0.13 ± 0.03	1929-2012	0.07 ± 0.05	0.2
(21088) 1992 BL2	1.71	0.24	38.46	4.23 ± 0.11	0.21 ± 0.05	1990-2012	0.05 ± 0.04	0.2
(3691) Bede	1.77	0.28	20.36	1.80 ± 0.11	0.59 ± 0.12	1975-2012	0.04 ± 0.03	0.1
(887) Alinda	2.48	0.57	9.36	4.79 ± 0.23	0.34 ± 0.06	1918-2008	0.03 ± 0.03	0.1
(16064) Davidharvey	2.85	0.59	4.54	4.11 ± 0.59	0.02 ± 0.01	1994-2009	0.02 ± 0.02	0.0
(433) Eros	1.46	0.22	10.83	33.60 ± 0.12	0.25 ± 0.06	1893-2012	0.02 ± 0.01	0.1
(1036) Ganymed	2.66	0.53	26.70	36.75 ± 0.31	0.23 ± 0.03	1924-2012	0.01 ± 0.01	0.0

CHAPTER 3

Description of Drift-Finding Method

3.1 Introduction

This chapter describes a method for determining semimajor axis drifts acting on an asteroid via fits to that asteroid's astrometry. We begin with relevant definitions.

The maximum possible drift rate for any radiation-powered force acting on NEAs can be obtained by equating the incident solar radiation energy on a disk over interval δt to the change in orbital energy over the interval δt.

$$-\frac{1}{2}GM_{\odot}m\left(\frac{1}{a_f}-\frac{1}{a_i}\right)=\frac{L_{\odot}}{4r^2}r_{ast}^2\delta t \tag{3.1}$$

Here $L_{\odot}$ and $M_{\odot}$ are respectively the luminosity and mass of the sun, G is the gravitational constant, r_{ast} and m are respectively the radius and the mass of the asteroid, and r is the average distance between the asteroid and the sun over dt. The quantity a_i is the initial semimajor axis of the object, and we define the final semimajor axis $a_f = a_i + \frac{da}{dt}\delta t$, which gives

$$\frac{da}{dt}=\frac{a^2}{r^2}\frac{L_{\odot}}{GM_{\odot}}\frac{r_{ast}^2}{2m} \tag{3.2}$$

From Kaula (1966),the change in mean anomaly M is defined as $dM = \frac{r^2 df}{\sqrt{a^2(1-e^2)}}$, where

e is the asteroid's eccentricity. We integrate $\frac{a^2}{r^2}$ over df to find $\langle\left(\frac{a}{r}\right)^2\rangle$ over an orbit,

$$\langle\left(\frac{a}{r}\right)^2\rangle = \frac{1}{2\pi}\int_0^{2\pi}\frac{a^2}{r^2}\frac{r^2}{a^2\sqrt{1-e^2}}df \tag{3.3}$$

which is

$$\langle\left(\frac{a}{r}\right)^2\rangle = \frac{1}{\sqrt{1-e^2}} \tag{3.4}$$

Incorporating Equation 3.4 with Equation 3.2 and writing m in terms of volume and density ρ ($m = \frac{4}{3}\frac{\rho\pi r_{ast}^3}{3}$),we find

$$\frac{da}{dt} = f_Y\frac{3}{4\pi}\frac{1}{\sqrt{1-e^2}}\frac{L_\odot}{GM_\odot}\frac{1}{D\rho}, \tag{3.5}$$

where f_Y is an efficiency factor analogous to that used by Goldreich & Sari (2009) and D is the effective diameter. This equation exhibits the expected dependence on the asteroid area-to-mass ratio. In convenient units, it reads

$$\frac{da}{dt} = \frac{1.457}{\sqrt{1-e^2}}\left(\frac{f_Y}{10^{-5}}\right)\left(\frac{1\text{km}}{D}\right)\times\left(\frac{1000\text{ kg m}^{-3}}{\rho}\right)10^{-3}\text{AU/Myr}. \tag{3.6}$$

Maximum efficiency (f_Y=1) would convert all incoming solar radiation into a change in orbital energy. We will show in Section 4 that typical Yarkovsky efficiencies are $f_Y \sim 10^{-5}$, and that typical rates are $\sim 10^{-3}$AU/Myr for kilometer-sized asteroids. The low efficiency and rates are due to the fact that it is the momentum of departing thermal photons that moves the asteroid.

As mentioned in Chapter 1, Chesley et al. (2003) used precise radar ranging measurements to (6489) Golevka and reported the first detection of asteroidal Yarkovsky drift. The drift rate for this NEA of $da/dt = (-6.39\pm0.44)\times10^{-4}$ AU/Myr (Chesley et al., 2008) corresponds to an efficiency $f_Y = 5\times10^{-6}$ for D=530 m and $\rho = 2700$ kg m^{-3}.

Vokrouhlický et al. (2008) employed the Yarkovsky effect to link a 1950 observation to asteroid (152563) 1992 BF with a da/dt rate of $(-10.7\pm0.7)\times10^{-4}$ AU/Myr. This

corresponds to an efficiency $f_Y = 7 \times 10^{-6}$ for D=420 m and ρ=2500 kg m^{-3}. If 1992 BF has a density closer to 1500 kg m^{-3}, the efficiency would be $f_Y = 4 \times 10^{-6}$.

There have been other searches for the effects of non-gravitational forces in asteroid orbits. Sitarski (1992) considered a semi-major axis drift in the orbit of (1566) Icarus and found $da/dt = (-7.3 \pm 3.9) \times 10^{-4}$ AU/Myr. Our best estimate is $da/dt = (-3.2 \pm 2.0) \times 10^{-4}$ AU/Myr. Sitarski (1998) found it necessary to incorporate a non-gravitational term $da/dt = -58 \times 10^{-4}$ AU/Myr in his orbit determination of (4179) Toutatis, however the availability of radar ranges in 1992, 1996, 2004, and 2008 strongly suggest a drift magnitude that does not exceed -5×10^{-4} AU/Myr. Ziolkowski (1983) examined the orbits of 10 asteroids and found drifts in four asteroids, including a $(-295.7 \pm 14.6) \times 10^{-4}$ AU/Myr drift for (1862) Apollo. Yeomans (1991) used a cometary model to search for perturbations and also detected a drift associated with (1862) Apollo, though a value was not reported. Our best estimate is $(-2.38 \pm 0.25) \times 10^{-4}$ AU/Myr (Section 4). It appears that these early estimates are not aligned with modern determinations, and may have been caused by erroneous or insufficient astrometry. More recently, Chesley et al. (2008) searched for Yarkovsky signatures and reported rate estimates for 12 candidates.

Here we use new developments in star catalog debiasing (Chesley et al., 2010) as well as the most recent astrometric data to compute semi-major drift rates for select NEAs, which multiplies the number of existing measurements by a factor of $\sim$4.

Observations of Yarkovsky rates can be used to place constraints on composition (i.e. metal vs. rock), physical properties (i.e. bulk density), and spin properties (i.e. prograde vs. retrograde). The magnitude of the force is dependent on the object's mass, size, obliquity, spin rate, and surface thermal properties. Separating how each of these quantities uniquely contributes to a measured da/dt is often not possible, but past Yarkovsky detections have allowed for insight into the associated objects. With certain assumptions on surface thermal properties, bulk densities were determined from the measured drifts of Golevka (Chesley et al., 2003) and (152563) 1992 BF (Vokrouhlický et al., 2008). For the latter, the magnitude and direction of the drift point to an obliquity in excess of 120 degrees (Vokrouhlický et al.,

2008).

3.2 Yarkovsky sensitivity

The Yarkovsky drift manifests itself primarily as a change in mean anomaly (or along-track position) (Vokrouhlický et al., 2000), and some observational circumstances are poorly suited to detect such changes. Examples include optical astrometry secured when the line-of-sight is roughly parallel to the asteroid velocity vector or when the object is at large distances from Earth. In both instances the differences in astrometric positions can be much smaller than observational uncertainties, resulting in low sensitivity to the Yarkovsky effect. The overall Yarkovsky sensitivity depends on the orbital geometry of the NEA and on the entire set of available observations. This can be quantified rigorously. For each epoch t_i at which optical observations were obtained ($1 \leq i \leq N$), we predict the position P_i^0 for the best-fit orbit ($da/dt = 0$) and the position P_i^* for the same orbit modified by a nominal non-zero da/dt. The value of the nominal rate is not important as long as it results in detectable ($\sim$arcsecond) changes in coordinates and as long as it is applied consistently to all objects; we used da/dt=0.1 AU/Myr.

We then define the *Yarkovsky sensitivity* s_Y as

$$s_Y = \sqrt{\frac{1}{N} \sum_{i=1}^{N} \frac{(P_i^* - P_i^0)^2}{\sigma_i^2}}, \tag{3.7}$$

where σ_i is the positional uncertainty associated with observation i. This root mean square quantity provides an excellent metric to assess the relative sensitivity of any given data set to a drift in semi-major axis, including drifts caused by Yarkovsky influences. The metric can be applied to the entire set of available observations, or to the subset of observations that survive the outlier rejection steps described below. We computed both quantities and used the latter for our analysis. We found that data sets with scores s_Y below unity yield unreliable results, including artificially large rates and large error bars. Out of $\sim$1,250

numbered NEAs, only ∼300 have $s_Y > 1$ and ∼150 have $s_Y > 2$. In this dissertation we focus on a subset of these NEAs.

3.3 Orbital fits

For this work we employed orbital fits to optical astrometry to determine semi-major axis drift rates for NEAs. We used the OrbFit software package, which is developed and maintained by the OrbFit Consortium (Milani & Gronchi, 2009). OrbFit can fit NEA trajectories to astrometric data by minimizing the root mean square of the weighted residuals to the data, optionally taking into account a given non-zero rate of change in semi-major axis da/dt. We included perturbations from 21 asteroids whose masses were estimated by Konopliv et al. (2011).

We downloaded optical astrometry for all numbered minor planets (NumObs.txt.gz) from the Minor Planet Center (MPC) on January 31st, 2012. We have assumed that all the astrometry has been properly converted to the J2000 system. The quality of the astrometry varies greatly, and we applied the data weighting and debiasing techniques implemented in OrbFit, which appear to follow the recommendations of Chesley et al. (2010). Data weights are based on the time the observation was performed, the method of the observation (CCD or plate), the accuracy of the star catalog, and in some cases the accuracy of the observatory. Correction for known star catalog biases was applied when possible. Biases vary depending on the specific star catalog and region of the sky, and can reach 1.5 arcseconds in both R.A. and Dec. Correction for these biases can substantially improve the recovery of orbital parameters from observations. However, as discussed in Chesley et al. (2010), not every observation can be debiased. Some observations were reported to the MPC without noting the star catalog used in the data reduction. Although Chesley et al. (2010) deduced the star catalogs used by several major surveys, there remain observations from smaller observatories that do not have associated star catalogs. Accordingly, a fraction of the astrometry used in this dissertation was not debiased. Based on counts published Chesley et al. (2010), we

estimate this fraction to be less than 7.2% of all the observations.

Our procedure for determining the semi-major axis drift rate included three steps: an initial fit to the debiased data, an outlier rejection step, and a search for the best-fit da/dt, with iteration of the last two steps when necessary.

We used the orbital elements from the Minor Planet Center's MPCORB database as initial conditions for the first fit for each object (step 1). This first fit, performed with $da/dt = 0$ and outlier rejection turned off, slightly corrected the orbital elements for our weighted, debiased observations. The orbital elements from each object's first fit became the starting orbital elements for all later fits of that object.

The second fit of each object served to reject outliers and was initially performed with $da/dt = 0$ (step 2). The residual for each observation was calculated using the usual observed (O) minus computed (C) quantities:

$$\chi_{\rm res} = \sqrt{\left(\frac{({\rm R.A._O} - {\rm R.A._C}) \times \cos({\rm Dec._O})}{\sigma_{\rm R.A.}}\right)^2 + \left(\frac{{\rm Dec._O} - {\rm Dec._C}}{\sigma_{\rm Dec.}}\right)^2}, \qquad (3.8)$$

where $\sigma_{\rm R.A.}$ and $\sigma_{\rm Dec.}$ are the uncertainties for that observation in R.A. and Dec., respectively. We rejected observations when their $\chi_{res} > \sqrt{8}$, and recovered previously rejected observations at $\chi_{res} = \sqrt{7}$, with the rejection step iterated to convergence. Results are fairly robust over a large range of thresholds for rejection (Section 4). If the post-fit residuals were normally distributed, the chosen thresholds would result in $< 1\%$ of observations being rejected as outliers. Because errors are not normally distributed, our typical rejection rates are 2-5% of all available astrometry. This second fit produced the set of observations which were used in the third step.

The third step was a series of orbital element fits to the observations over a set of fixed da/dt values. During these fits, we used the set of observations defined by the second fit and did not allow further outlier rejection. The quality of a fit was determined by summing the squares of residuals $\chi^2 = \sum \chi^2_{res}$. To locate the region with the lowest χ^2, we used a three-point parabolic fit or the golden-section minimization routine (Press et al., 1992).

A parabola was then fit to the χ^2 curve in the vicinity of the minimum, and we used the minimum of the parabola to identify the best-fit da/dt value.

Confidence limits were estimated using χ^2 statistics. Confidence regions of 68.3% and 95.4% (1σ and 2σ, respectively) were established by the range of da/dt values that yielded χ^2 values within 1.0 and 4.0 of the best-fit χ^2 value, respectively (Fig. 3.1).

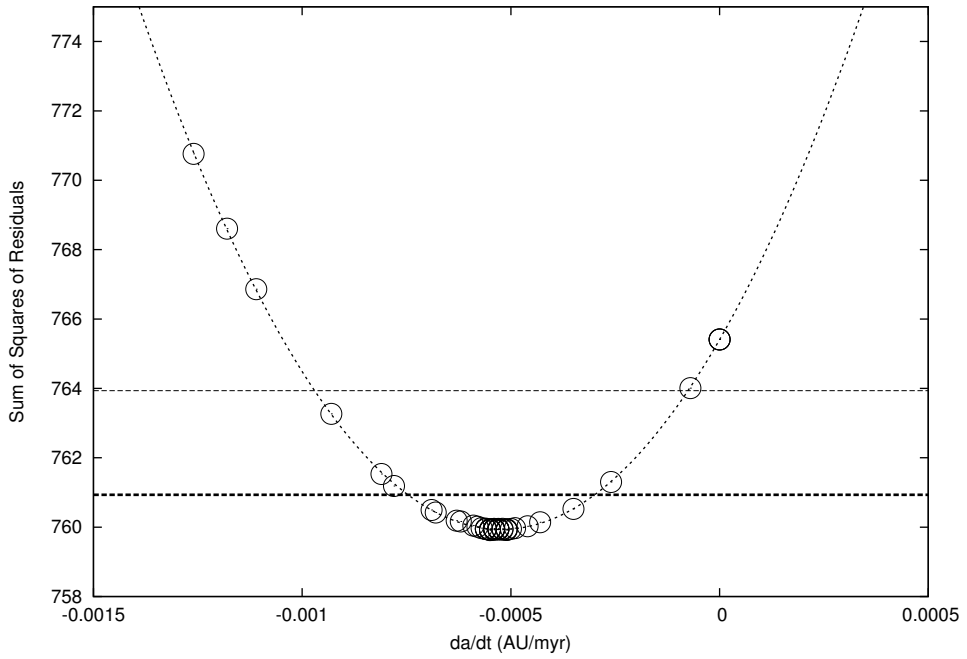

Figure 3.1 Search for best-fit da/dt value to optical astrometry of (2100) Ra-Shalom (1,281 observation epochs, 2,562 observations, 7 adjustable parameters, 2,555 degrees of freedom). The sums of squares of residuals corresponding to a range of da/dt values are shown as circles, with a parabolic fit shown as a dotted line. The da/dt values plotted here were determined by the golden section search algorithm (Press et al., 1992) as it searched for and found a minimum at $da/dt = -5.20 \times 10^{-4}$ AU/Myr with a reduced χ^2 value of 0.30. Confidence limits of 68.3% (1σ) are indicated by the thick dashed line, and correspond to the range $da/dt = [-7.4, -2.9] \times 10^{-4}$ AU/Myr. The thin dashed line shows the 95.4% (2σ) confidence region.

The initial outlier rejection step can in some cases eliminate valid observations simply because the Yarkovsky influences are not captured in a dynamical model with $da/dt = 0$. To circumvent this difficulty, we iterated the outlier rejection step with the best-fit da/dt value and we repeated the fitting process. In 52 out of 54 cases, the new best-fit value matched

the previous best-fit value to within 1σ, and we accepted the new best-fit values as final. For the other objects we repeated the reject and fit processes until successive best-fit values converged within 1σ (which never required more than one additional iteration). Our results report the da/dt values obtained at the end of this iterative process.

3.4 Sample selection

We restricted our study to numbered NEAs with the best Yarkovsky sensitivity (Equation 3.7), specifically $s_Y > 2$ (Fig. 4.1).

We also chose to focus on objects with non-zero da/dt values by using a signal-to-noise ratio (SNR) metric, defined as the ratio of the best-fit da/dt to its 1σ uncertainty. We accepted all objects with SNR > 1 (Fig. 4.1).

Some asteroids have observations that precede the majority of the object's astrometry by several decades and have relatively high uncertainties. In order to test the robustness of our results, we removed these sparse observations, which were defined as ten or fewer observations over a 10-year period. Fits were then repeated for these objects without the early observations. If the initial best-fit value fell within the 1σ error bars of the new best-fit value, the initial result was accepted; otherwise, the object was rejected.

Superior detections of the Yarkovsky effect are likely favored with longer observational arcs, larger number of observations, and good orbital coverage. For this reason we limited the sample to those NEAs with an observational arc at least 15 years long, with a number of reported observations exceeding 100, and with at least 8 observations per orbit on at least 5 separate orbits.

We report on the 54 objects that met all of these criteria: sensitivity, SNR, sparse test, and orbital coverage.

3.5 Validation

We validated our optical-only technique whenever radar ranging observations were available on at least two apparitions. This could only be done for a fraction of the objects in our sample. In the remainder of this chapter, *optical-only* results are clearly distinguished from *radar+optical* results. For the radar+optical fits, we included all available radar astrometry and disallowed rejection of potential radar outliers. The internal consistency of radar astrometry is so high that outliers are normally detected before measurements are reported.

We also verified that a fitting procedure that holds successive da/dt values constant is equivalent to performing 7-parameter fits (6 orbital parameters and da/dt simultaneously). The da/dt values obtained with both procedures are consistent with one another.

3.6 Yarkovsky modeling

In addition to the measurements described above, we produced numerical estimates of the diurnal Yarkovsky drift for each of the objects in our sample. Comparing the measured and estimated rates provides a way to test Yarkovsky models. In some instances, e.g., robust observations irreconcilable with accurate Yarkovsky modeling, it could also lead to the detection of other non-gravitational forces, such as cometary activity. Our numerical estimates were generated as follows. At each timestep, we computed the diurnal Yarkovsky acceleration according to equation (1) of Vokrouhlický et al. (2000), which assumes a spherical body, with the physical parameters (Opeil et al., 2010) listed in Table 2.1 and an assumption of 0° or 180° obliquity. We assumed that the thermal conductivity did not have a temperature dependence, but found that adding a temperature-dependent term according to the prescription of Hütter & Kömle (2008) ($K = K_0 + K_1 T^3$, with $K_1 = 0.0076$) did not change our predictions by more than 1%. We then resolved the acceleration along orthogonal directions, and used Gauss' form of Lagrange's planetary equations (Danby, 1992) to evaluate an orbit-averaged da/dt.

The physical parameters chosen for these predictions mimic two extremes of rocky asteroids; one is intended to simulate a rubble pile with low bulk density, the other a regolith-free chunk of rock (Table 2.1). These parameters correspond to a thermal inertia range of $77-707$ J m^{-2} s$^{-0.5}$ K^{-1}, enveloping the results of Delbó et al. (2007), who found an average NEA thermal inertia to be 200 J m^{-2} s$^{-0.5}$ K^{-1}. In most cases, the drift rates produced by these two extreme cases encompass the drift produced by a rubble-pile object that has a regolith-free surface, or the drift produced by a solid object with regolith.

There is no simple relationship between these physical parameters and predicted drift rates, but for most cases the rubble pile exhibits the larger da/dt values due to its low bulk density (Equation 3.6). The smaller values of density of the surface and thermal conductivity for rubble piles produce a smaller thermal inertia, and therefore a longer thermal lag. Generally, but not always, this longer thermal lag, combined with the rotation of the asteroid, allows for a larger fraction of departing thermal emission to be aligned with the asteroid's velocity, resulting in a larger drift.

When available, measured values of the geometric albedo, diameter, and spin rate from the JPL Small-Body Database (Chamberlin, 2008) were incorporated into our predictions for Yarkovsky drifts. When not available, the diameter D in km was estimated from the absolute magnitude H using (Pravec & Harris, 2007),

$$D = \frac{1329}{\sqrt{p_V}} * 10^{-0.2H} \tag{3.9}$$

where we used two values of the V-band geometric albedo p_V (0.05 and 0.45), a range that captures observed albedos for the majority of NEAs. When spin rate was unknown, we assumed a value of 5 revolutions/day, based on the average spin rate values for asteroids 1 to 10 km in diameter shown in Fig. 1 of Pravec & Harris (2000). Emissivity was assumed to be 0.9. Bond albedo was estimated with a uniform value of the phase integral (q=0.39) on the basis of the IAU two-parameter magnitude system for asteroids Bowell et al. (1989) and an assumed slope parameter G=0.15.

We have assumed $p_V = 0.14$ for the purpose of quantifying the Yarkovsky efficiency when the asteroid size was unknown.

The results of this method are discussed in the following chapter.

CHAPTER 4

Detected Drifts and their Scientific Consequences

We measured the semi-major axis drift rate of all 1,252 numbered NEAs known as of March 2012. Some of the drift rates are not reliable because of poor sensitivity to Yarkovsky influences (Fig. 4.1).

After our process of selection and elimination (Section 3.4), we were left with 54 NEAs that exhibit some of the most reliable and strongest drift rates. Although we report objects with $s_Y > 2$, we have the most confidence in objects with highest Yarkovsky sensitivity, and we show objects in order of decreasing s_Y value in our figures.

We examined the impact of various choices of reject/recover thresholds when rejecting outlier observations (Fig. 4.2). At moderate values of the rejection threshold (i.e. eliminating less than $\sim$5% of observations), best-fit values are consistent with one another. In this regime, results are fairly robust against the choice of rejection thresholds. However results do become sensitive to rejection thresholds when a larger fraction of observations is rejected. As the reject/recover thresholds become more stringent, astrometry with evidence of semi-major axis drift is preferentially rejected, and the best-fit da/dt values approach zero. Our adopted reject/recover thresholds ($\sqrt{8}/\sqrt{7}$) are stringent enough that they eliminate obvious outliers, but not so stringent as to suppress the Yarkovsky signal. In 52 out of 54 cases, repeating the outlier rejection step with the best-fit da/dt value resulted in no appreciable change to the result.

As a validation step, we compared the semi-major axis drift rates obtained with our procedure (both optical-only and radar+optical) to previously published values (Table 4.1). We found good agreement for Golevka (Chesley et al., 2003; Chesley et al., 2008) and

1992 BF (Vokrouhlický et al., 2008), and for most, but not all, NEAs included in a similar study done by Chesley et al. (2008). The differences between our results and those of Chesley et al. (2008) can probably be attributed to our use of debiased data, of improved data weights, and of longer observational arcs extending to 2012. Eight objects included in Table 4.1 meet our selection criteria for detailed analysis in the rest of this chapter: (1620) Geographos, (1685) Toro, (1862) Apollo, (1865) Cerberus, (2063) Bacchus, (2100) Ra-Shalom, (2340) Hathor, and (152563) 1992 BF.

Table 4.1 Comparison of our optical-only results to radar+optical (r+o) results and to the results of a previous study by Chesley et al. (2008). Best-fit da/dt values in units of 10^{-4} AU/Myr and their one-sigma uncertainties are listed for optical-only and radar+optical observations. Also shown is the root-mean-square (RMS) of weighted residuals for the gravity-only ($da/dt = 0$) solution and for the non-zero da/dt solution (RMS'). We restrict the radar analysis to those objects that have range measurements on at least two apparitions; this excludes (1685) Toro, (1865) Cerberus, (2063) Bacchus, (2340) Hathor, (85953) 1999 FK21, and (152563) 1992 BF.

NEA	radar RMS	radar RMS'	r+o RMS'	optical-only da/dt	r+o da/dt	Chesley 08 da/dt
(1620) Geographos	0.393	0.356	0.55	-2.43 ± 0.7	-2.52 ± 0.6	-1.18 ± 0.39
(1685) Toro	···	···	0.51	-1.40 ± 0.7	···	-0.52 ± 0.27
(1862) Apollo	1.111	0.403	0.61	-1.79 ± 0.6	-2.38 ± 0.3	-2.44 ± 0.26
(1865) Cerberus	···	···	0.54	-5.11 ± 2.7	···	-7.80 ± 2.28
(2063) Bacchus	···	···	0.59	-4.17 ± 3.7	···	-10.59 ± 2.21
(2100) Ra-Shalom	0.488	0.594	0.51	-4.79 ± 2.2	-5.45 ± 1.5	-7.09 ± 0.88
(2340) Hathor	···	···	0.67	-14.55 ± 3.6	···	-13.94 ± 3.84
(6489) Golevka	0.879	0.387	0.61	-2.05 ± 12.6	-5.74 ± 0.7	-6.39 ± 0.44
(54509) YORP[a]	0.796	0.260	0.55	-25.98 ± 37.4	-35.63 ± 10.5	-25.12 ± 6.18
(85953) 1999 FK21[b]	···	···	0.56	-10.44 ± 1.5	···	-14.13 ± 2.35
(101955) 1999 RQ36[b]	15.694	0.127	0.39	-12.90 ± 7.1	-18.9 ± 0.2	-15.69 ± 4.99
(152563) 1992 BF[c]	···	···	0.60	-12.84 ± 1.0	···	-10.78 ± 0.73

[a]This object is in a Sun-Earth horseshoe orbit (Taylor et al., 2007). [b]This object experiences perihelion precession of ∼16 arcseconds/century (Margot & Giorgini, 2009b).[c] This object is the target of the OSIRIS-REx mission (Chesley et al., 2012). [d]Fits to this object use the astrometry corrections given in Vokrouhlický et al. (2008) for the 1953 observations, which we did not subject to rejection.

Several conclusions can be drawn from the data presented in Table 4.1. First, the RMS

values indicate excellent fits to the astrometry. Second, the solutions with non-zero da/dt values provide a much better match to the radar data than the gravity-only solutions, with typical RMS values decreasing by a factor of 2 or more. Third, radar+optical estimates have consistently lower error bars than optical-only estimates, sometimes dramatically so, which is typical in NEA studies. Finally, there is a generally good agreement between the optical-only da/dt values and the radar+optical da/dt values, indicating that the optical-only technique is a useful tool that can be used even in the absence of radar data.

Drift rates for the 54 NEAs that pass our selection criteria are presented in Table 4.3 (end of this chapter) along with orbital elements and physical properties. If an object has both a optical-only and a radar+optical value, we used the more accurate radar+optical value in the following figures and calculations (unless specified otherwise). We used Equation (3.6) with a density of 1,200 kg m^{-3} to compute efficiency factors f_Y and found that objects divided roughly into two groups.

In the first group of 42 objects with $f_Y \leq 2 \times 10^{-5}$, most observed da/dt values are consistent (within 1σ) with Yarkovsky predictions. We refer to these objects as *Yarkovsky-dominated* (Figs. 4.3 and 4.4). In the second group of 12 objects with $f_Y > 2 \times 10^{-5}$ the observed da/dt values are somewhat larger than Yarkovsky predictions, but improvements in the knowledge of physical properties or in Yarkovsky modeling could plausibly bring some of the observed rates in agreement with predictions. We refer to these objects as *possibly Yarkovsky-dominated* (Fig. 4.5).

Figures 4.3 and 4.4 indicate that there is generally agreement between observations and numerical estimates of Yarkovsky drift rates for NEAs with $f_Y \leq 2 \times 10^{-5}$. These data suggest that $f_Y \sim 10^{-5}$ represents a typical efficiency for the Yarkovsky process. Predicted values are based on calculations with obliquities of 0° and 180°, therefore, observed rates that are lower than predictions could still be due to the Yarkovsky effect.

The majority of objects in Fig. 4.4 appear to exceed predictions. This is a consequence of the SNR > 1 selection criterion, as it eliminates objects with lower da/dt values.

On the basis of the entire sample of measured drifts for objects with $s_Y > 2$, we can compute average properties for observed Yarkovsky rates and efficiencies. The mean, mean weighted by uncertainties, median, and dispersion are shown in Table 4.2. The aggregate properties are comparable if we restrict objects to the subset with SNR > 1, except for slightly increased da/dt rates (median rate of $\sim 12 \times 10^{-4}$ AU/Myr instead of $\sim 7 \times 10^{-4}$ AU/Myr), as expected. The Yarkovsky process appears to have an efficiency f_Y of order 10^{-5}, with a fairly small dispersion. Because the Yarkovsky efficiency scales with density ($f_Y|_\rho = f_Y|_{1,200} \times \rho/1,200$ kg m^{-3}) some of the observed scatter is due to density variations.

4.1 Discussion

In this chapter we examine several consequences of our results. First we discuss how the Yarkovsky drifts can inform us about asteroid physical properties, spin states, and trajectories. Then we discuss binary asteroid (1862) Apollo and the curious case of asteroid (1036) Ganymed. Finally we discuss the possible mechanisms for non-Yarkovsky driven rates, including association with meteoroid streams and rock comet phenomenon.

4.2 Yarkovsky-derived constraints on asteroid physical properties

Because a clear connection exists between asteroid physical properties and Yarkovsky drifts, we explored the constraints that can be placed on bulk density and surface thermal conductivity for seven objects with well-known diameters and (excepting one case) spin periods: (1620) Geographos, (1862) Apollo, (2100) Ra-Shalom, (2062) Aten, (2340) Hathor, (1566) Icarus, and (3361) Orpheus. We compared the measured Yarkovsky rates to numerical estimates obtained with a range of physical parameters. For these estimates, we assumed a constant heat capacity $C_p = 500$ J kg^{-1} K^{-1} (Table 2.1) and a single value of the bulk density of the surface $\rho_s = 1,700$ kg m^{-3}, but we explore a wide range of bulk density and surface thermal conductivity values. Because the obliquities are uncertain or ambiguous in many

cases, we chose to illustrate outcomes for two obliquity values, typically 180° and 135°.

Our results are shown in Figures 4.6 and 4.7, which are similar to Fig. 4 in Chesley et al. (2003). The shaded range consistent with the 1σ confidence limits on da/dt delineates the space of acceptable bulk densities and thermal conductivities, assuming that the Yarkovsky effect is being modeled correctly. By acceptable, we mean consistent with observed da/dt values, even though some of the $K - \rho$ values may not be appropriate for asteroids.

Infrared observations indicate that (2100) Ra-Shalom has a thermal conductivity between 0.1 and 1 W m^{-1} K^{-1} (Delbó et al., 2003; Shepard et al., 2008). If we assume a minimum bulk density of 1,500 kg m^{-3}, this conductivity value is consistent with the range suggested by our Yarkovsky rate determination.

If we make the same minimum density assumption for (1620) Geographos, our measurements suggest that its surface thermal conductivity is greater than 0.002 W m^{-1} K^{-1}.

For (1862) Apollo, we show the range of physical properties that are consistent with both the optical-only fits and the radar+optical fits. The precision of the radar measurements dramatically shrinks the size of the measured error bars, with correspondingly tighter constraints on density and surface thermal conductivity. This example illustrates that reliable obliquity determinations will be important to extract physical properties from Yarkovsky rate determinations.

Our measurement of (2062) Aten's drift provides some useful insights. If we assume that its bulk density exceeds $1,500$ kg m^{-3}, then its surface thermal conductivity K must exceed 0.3 W m^{-1} K^{-1}. Furthermore, if we assume that its bulk density exceeds $1,600$ kg m^{-3}, the 1σ confidence region on the measured Yarkovsky drift suggests that its obliquity is between $180° - 135°$.

The Yarkovsky simulations for (2340) Hathor were computed with an assumed spin period of 4.5 hours. If the actual period is longer, the curves shown would shift to the left, and if the period is shorter, the curves would shift to the right. Consequently, we cannot make inferences about the K value for this object until its spin period is measured. However,

looking at the height of the curve, and with an assumption that the object's bulk density is greater than $1,500$ kg m^{-3}, we can conclude that (2340) Hathor likely has an obliquity lower than 180°.

The assumption of 135° or 180° obliquity for (1566) Icarus restricts this object to low surface conductivity values and low bulk density values, or high surface conductivity values and high bulk density values. Although these obliquities do produce physically plausible parameter combinations, it seems likely that the obliquity for this object is $\leq 135°$.

The curves for (3361) Orpheus were calculated with an assumed geometric albedo of 0.15. As (3361) Orpheus has a positive da/dt value, obliquities were assumed to be 0° and 45°. The curve representing an obliquity equal to 0° for this object requires very low (< 0.002 W m^{-1} K^{-1}) or very high (> 0.7 W m^{-1} K^{-1}) surface thermal conductivity values for most densities. A more likely scenario is that this object has an obliquity $> 0°$, or perhaps even $> 45°$. An independent measurement of the obliquity could be used to validate obliquity constraints derived from Yarkovsky measurements.

4.3 Yarkovsky rates and distribution of spin states

La Spina et al. (2004) and Chesley et al. (2008) examined the predominance of retrograde spins and negative Yarkovsky drift rates and concluded that they were consistent with the presumed delivery method of NEAs from the main belt of asteroids. The ν_6 and 3:1 resonance regions deliver NEAs to near-Earth space (Bottke et al., 2002a). A main belt asteroid can arrive at the 3:1 resonance at 2.5 AU via a positive (if it originates in the inner main belt) or negative (if it originates in the outer main belt) Yarkovsky drift. However, a main belt asteroid can only arrive at the ν_6 resonance (at the inner edge of the main belt) by way of a negative drift. According to Bottke et al. (2002a) and Morbidelli & Vokrouhlický (2003), $30\%-37\%$ of NEAs are transported via the ν_6 resonance, with the rest from other resonances. The net result is a preference for retrograde spins.

An observational consequence of this process would be an excess of retrograde rotators in

the near-Earth asteroid population. La Spina et al. (2004) conducted a survey of 21 NEAs and found the ratio of retrograde/prograde rotators to be $2.0^{+1}_{-0.7}$.

We note that out of the 42 Yarkovsky-dominated NEAs, 12 have a positive da/dt value. For this sample, our ratio of retrograde/prograde rotators is 2.5 ± 0.1, similar to the value found by La Spina et al. (2004).

4.4 Impact of drift rates on asteroid trajectory predictions

The semi-major axis drifts described in this chapter affect NEA trajectory predictions. An order of magnitude estimate for the along track displacement due to a non-zero da/dt is given in Vokrouhlický et al. (2000):

$$\Delta\rho \simeq 7\dot{a}_4(\Delta_{10}t)^2 a_{AU}^{-3/2} \tag{4.1}$$

where $\Delta\rho$ is in units of km, $\dot{a}_4$ is da/dt in 10^{-4} AU/Myr, $\Delta_{10}t$ is the time difference between observations in tens of years, and a_{AU} is the semimajor axis of the object in AU. For instance, the estimated along-track displacement due to the observed da/dt for (1862) Apollo is 9 km after 10 years. Similarly, the estimated along-track displacement for faster-moving (1864) Daedalus is 67 km after 10 years.

Our data indicate that (101955) 1999 RQ36, the target of the OSIRIS-REx mission, has a measurable Yarkovsky drift of $(-18.9 \pm 0.2) \times 10^{-4}$ AU/Myr. Although it has a relatively short arc (12 years) it has been observed three times by radar, allowing for an accurate da/dt measurement. We estimated the along-track displacement of (101955) 1999 RQ36 over the 6-month duration of the OSIRIS-REx mission to be 0.3 km, which will be easily detectable by a radio science instrument.

4.5 Binary asteroid (1862) Apollo

(1862) Apollo is a binary asteroid (Ostro et al., 2005). Binary asteroids present a unique opportunity for the determination of physical parameters. If mass and density can be measured from the binary orbit and component sizes, the Yarkovsky constraint on thermal conductivity can become much more meaningful. If the orientation of the plane of the mutual orbital can be measured, a plausible obliquity can be assumed, which makes the constraints on thermal properties tighter still. In some cases, actual obliquity measurements can be obtained from shape modeling efforts.

Yeomans (1991, 1992) identified a non-gravitational perturbation acting on the orbit of (1862) Apollo, but was not able to determine a drift magnitude. To 1σ our observed da/dt value for (1862) Apollo agrees with our Yarkovsky predictions.

4.6 The curious case of (1036) Ganymed

(1036) Ganymed has by far the largest Yarkovsky efficiency value ($f_Y \sim 15 \times 10^{-5}$) among the objects presented in Table 4.3. With a nominal value of $\sim -7 \times 10^{-4}$ AU/Myr, the measured da/dt value is comparable to that of other NEAs. Combined with Ganymed's large diameter estimate (~ 32 km based on IRAS measurements, Tedesco et al. (2002)), this Yarkovsky rate results in an unusually high f_Y value.

How can this anomaly be explained? One possibility is that some of the early astrometry, dating back to 1924, is erroneous. This could be due to measurement errors, timing errors, bias errors, or reference frame conversion errors. We evaluated the semi-major axis drift with various subsets of the available astrometry and found values ranging between -3×10^{-4} and -8×10^{-4} AU/Myr. On that basis we modified the adopted uncertainties for this object, and our preferred value is $(-6.62^{+3.6}_{-1.4}) \times 10^{-4}$ AU/Myr. Doing so does not eliminate the possibility of systematic bias in the astrometry, and we are still left with anomalously high f_Y values.

Another possibility is that the diameter of Ganymed, an S-type asteroid, is much smaller than reported. This seems unlikely considering the more recent WISE diameter measurement of 37 ± 3 km (Mainzer et al., 2011b).

If Ganymed's bulk density was especially low, a higher than usual f_Y value would be expected, but this would likely explain a factor of 2 or 3 at most, and would not explain the anomalous value.

Perhaps Ganymed departs significantly from a spherical shape, with an effective diameter and mass that are much smaller than those implied by the diameter values reported in the literature. The relatively low lightcurve amplitudes (~ 0.2 mag, Mainzer et al. (2011b)) do not seem to support such an argument, unless the asteroid is particularly oblate. In that case one could plausibly arrive at volume and mass estimates that are off by a factor of 5-10.

If we can rule out these possibilities (i.e. Ganymed is roughly spherical with no substantial concavities, its diameter estimate is reasonably accurate, and the early astrometry can be trusted), and if no other modeling error can be identified, then we would be compelled to accept an anomalously high Yarkovsky efficiency for this object.

4.7 Non-Yarkovsky processes

In the course of our study we observed drift values that cannot be accounted for easily by Yarkovsky drift, because they considerably exceed the predicted Yarkovsky rates. In most cases, these can be attributed to poor sensitivity to Yarkovsky influences (Fig. 4.1). Therefore, the high rates can generally be safely discarded. In other cases, the high rates may be due to erroneous optical astrometry or mismodeling of asteroid-asteroid perturbations. However we cannot entirely rule out the possibility that some of the high drift rates are secure and will be confirmed by further observation and analysis. If the high rates cannot be ascribed to poor Yarkovsky sensitivity or faulty astrometry, one would need to invoke other non-gravitational forces.

One possibility is that orbits are perturbed when NEAs are losing gas or dust in an

anisotropic manner. To estimate a rough rate of mass loss that would be needed to account for the drifts measured, we used the basic thrust equation

$$F = qV_e \tag{4.2}$$

where F is the force, q is the rate at which the mass departs the asteroid, and V_e is the ejection speed. For an asteroid of mass m this yields

$$a_{\text{massloss}} = \frac{qV_e}{m} \tag{4.3}$$

which can be incorporated into Gauss' form of Lagrange's planetary equations (Danby, 1992) as an acceleration aligned with the velocity of the object. The dependence of the force on heliocentric distance r is not known precisely; we assumed $F \propto r^{-2}$, similar to the Yarkovsky dependence, for simplicity, and because the amount of outgassing likely scales with the amount of incident radiation (as in Fig. 4 of Delsemme (1982)). We assumed $V_e = 1.5$ m s^{-1}, the value derived by Hsieh et al. (2004) for 133P/Elst-Pizarro, and we assumed that the mass is departing in the optimal thrust direction.

We quantified the mass loss rates needed to produce the observed drifts of NEAs with the highest Yarkovsky efficiencies. We estimated a rate of 0.16 kg s^{-1} for (154330) 2002 VX94 and 2.3 kg s^{-1} for (7889) 1994 LX. Although these estimates represent the minimum amount of mass loss necessary to account for the observed drifts (if due to mass loss), they are smaller than typical levels from comets. Comets have mass loss rates that span a wide range of values. On the high side a rate of 2×10^6 kg s^{-1} was estimated for Hale-Bopp (Jewitt & Matthews, 1999). On the low side Ishiguro et al. (2007) measured mass loss rates for three comets, averaged over their orbits: 2P/Encke (48 ± 20 kg s^{-1}), 22P/Kopff (17 ± 3 kg s^{-1}), and 65P/Gunn (27 ± 9 kg s^{-1}). Mass loss rates of active asteroids have been estimated to be in the range from ≤ 0.04 kg s^{-1} (113P/Elst-Pizarro) to ≤ 150 kg s^{-1} (107P/Wilson-Harrington) (Jewitt, 2012).

Mass loss does not seem to be a viable mechanism to explain the semi-major axis drift

rate of (1036) Ganymed, as it would require a minimum mass loss rate of ∼2,500 kg s^{-1}. This would presumably have left detectable observational signatures, which have not been reported to date.

We explore a couple of possibilities for mass loss mechanisms that could cause semi-major axis drifts.

4.7.1 Associations with meteoroid streams

To our knowledge, (433) Eros, (1566) Icarus, (1620) Geographos, (1685) Toro, (1862) Apollo, and 1982 TA are the only objects in our sample to have been associated with a meteoroid stream. Sekanina (1976) found a weak correlation between the first five objects and various streams using the "dissimilarity criterion". However, this metric was later described as not convincing by Jenniskens (2008), and current literature does not support such associations. In our results, Apollo shows good agreement with Yarkovsky predictions, with $f_Y = 0.25 \times 10^{-5}$. The Yarkovsky force is therefore a plausible cause of Apollo's observed semi-major axis drift.

4.7.2 Rock comet phenomenon

The brightening of (3200) Phaethon, the parent body of the Geminid meteor shower, has been attributed to a "rock comet" phenomenon (Jewitt & Li, 2010). With a perihelion at 0.14 AU, (3200) Phaethon's surface temperatures have been estimated by Jewitt & Li (2010) to be in the range $746 < T < 1050$ K. The authors propose that these high surface temperatures could create thermal gradients in the body, resulting in thermal fracturing that would release dust. The resulting mass loss would affect the orbit. The combination of mass loss due to decomposing hydrated minerals and thermal fracturing led the authors to term (3200) Phaethon a "rock comet". A moderate amount ($\sim$ 1 kg s^{-1}) of mass lost in an anisotropic manner by "rock comets" could explain the observed semi-major axis drift rates.

4.8 Conclusions

Modeling of the Yarkovsky effect is needed to improve trajectory predictions of near-Earth asteroids and to refine our understanding of the dynamics of small bodies. Using fits to astrometric data, we identified semi-major axis drifts in 54 NEAs, 42 of which show good agreement with numerical estimates of Yarkovsky drifts, indicating that they are likely Yarkovsky-dominated. These objects exhibit Yarkovsky efficiencies of $\sim 10^{-5}$, where the efficiency describes the ratio of the change in orbital energy to incident solar radiation energy. 12 objects in our sample have drifts that exceed nominal Yarkovsky predictions and are labeled possibly Yarkovsky-dominated. Improvements in the knowledge of physical properties or in thermal modeling could bring these drift rates in better agreement with results from numerical models. However, if the high rates are confirmed by additional observations and analysis, they would be indicative of the presence of other non-gravitational forces, such as that resulting from a loss of mass.

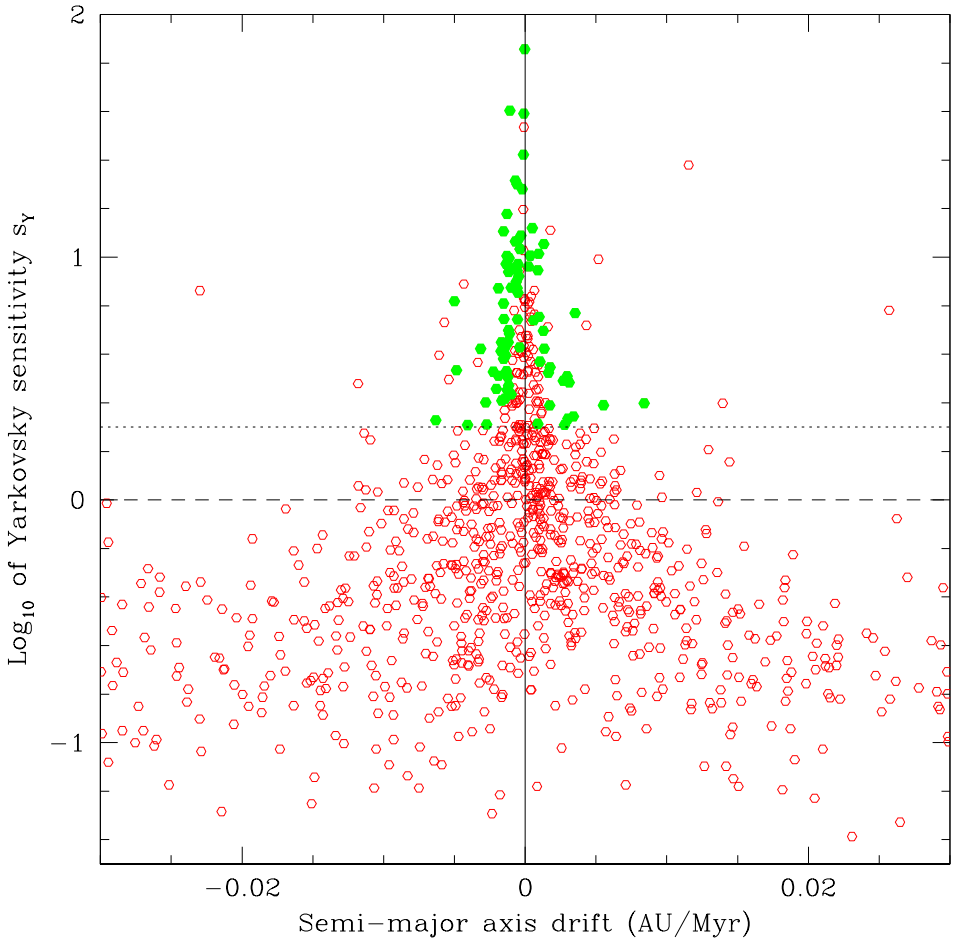

Figure 4.1 Yarkovsky sensitivity metric s_Y plotted as a function of semi-major axis drift rate da/dt for 1,252 numbered NEAs. Data sets with Yarkovsky sensitivity below unity (dashed line) yield unreliable results, including large rates and large error bars. Our selection criteria require $s_Y > 2$ (dotted line) and SNR > 1. The 80 objects that meet both selection criteria are shown in green. About 26 of these 80 NEAs are eliminated by the sparse test and orbital coverage requirements (see Section 3.4).

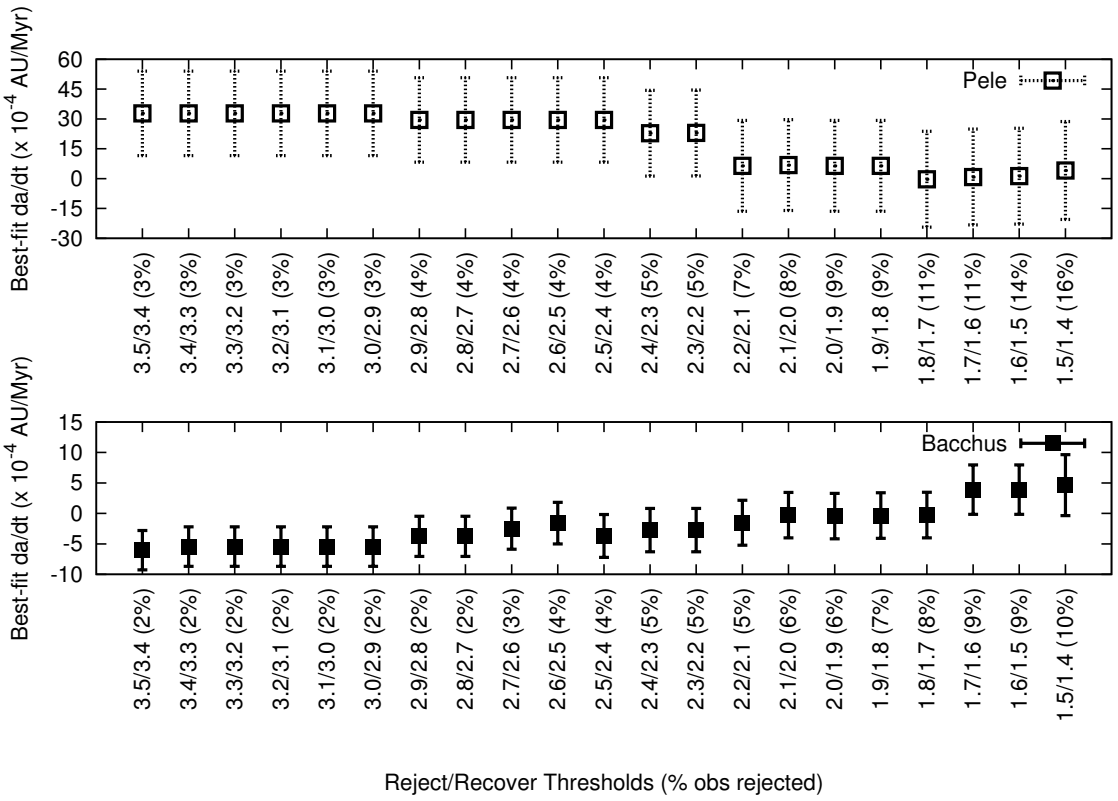

Figure 4.2 Impact of different choices of reject/recover thresholds for the initial rejection step ($da/dt = 0$) on the best-fit da/dt values. Results from optical-only fits are shown with their 1σ error bars for two representative cases, (2202) Pele and (2063) Bacchus. Best-fit da/dt values are consistent with one another in the left half of the diagram. Values to the right of 2.3/2.2 (Pele) and 2.5/2.4 (Bacchus) have SNR less than unity and would not meet our selection criteria. Our adopted reject/recover thresholds are $\sqrt{8} = 2.828$ and $\sqrt{7} = 2.646$.

Table 4.2 Statistical properties of observed Yarkovsky rates and efficiencies.

		abs$(da/dt) \times 10^{-4}$ AU/Myr		
Yarkovsky rate	mean	weighted mean	median	stdev
objects with $f_Y < 2 \times 10^{-5}$	7.6	4.4	5.6	6.4
objects with $f_Y > 2 \times 10^{-5}$	27.0	18.5	20.1	18.7
all objects	10.4	5.2	7.3	11.4
		$f_Y \times 10^{-5}$		
Yarkovsky efficiency	mean	weighted mean	median	stdev
objects with $f_Y < 2 \times 10^{-5}$	0.67	0.53	0.50	0.51
objects with $f_Y > 2 \times 10^{-5}$	4.50	7.47	3.01	3.38
all objects	1.22	0.89	0.65	1.91

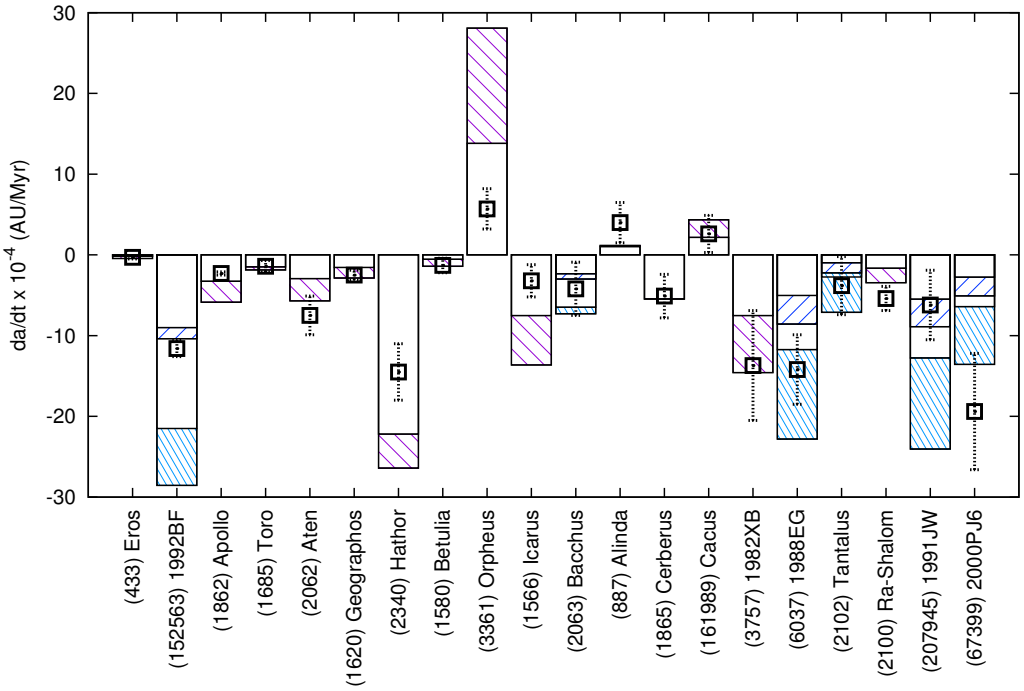

Figure 4.3 Measured and predicted drift values for 20 asteroids with Yarkovsky-dominated drifts, ordered by decreasing value of Yarkovsky sensitivity. Best fits to optical-only data are shown as squares with dotted 1σ error bars. Shaded boxes show a range of predicted Yarkovsky rates representing different compositions (Table 2.1). As predicted Yarkovsky values were calculated assuming 0° or 180° obliquity, the shaded boxes represent maximum drifts for the object. Therefore, a fit that lies between a shaded box and $da/dt = 0$ is considered to have good agreement. Objects with a single corresponding shaded box have a known diameter (Table 4.3). Objects with two shaded boxes did not have known diameters, and were modeled using diameters derived from assumed albedos (45% in light blue, larger predicted drift magnitudes, and 5% in dark blue, smaller predicted drift magnitudes). The vertical extents of the shaded boxes represent the range of compositional types described in Table 2.1, with the larger absolute values representing the "rubble pile" composition, and the lower absolute values representing the "rock chunk" composition.

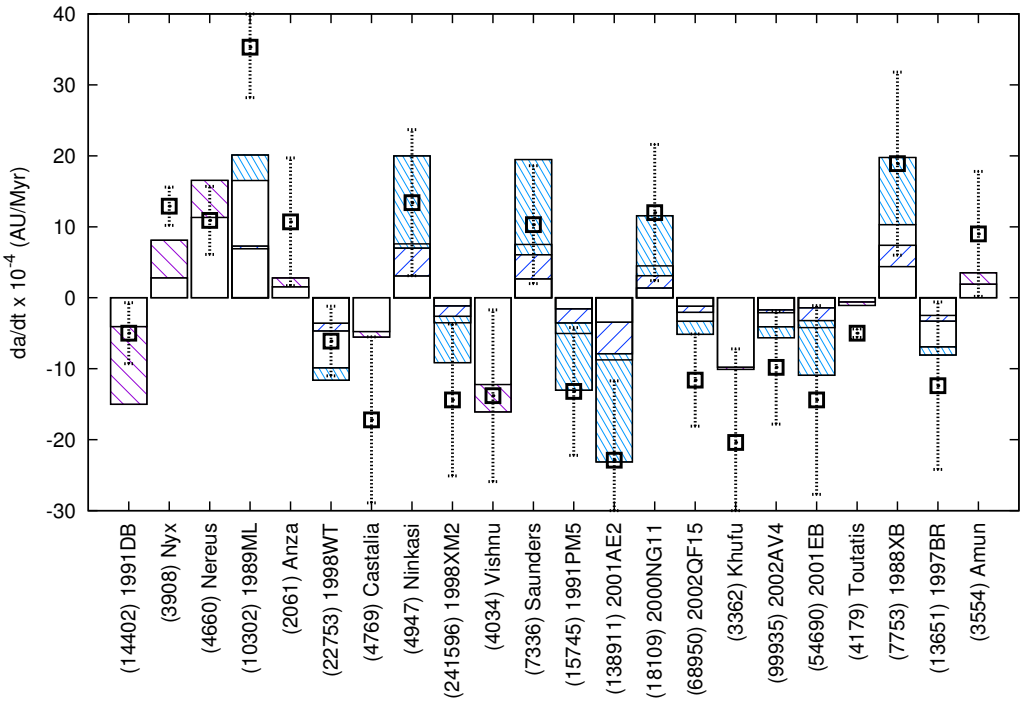

Figure 4.4 Measured and predicted drift values for an additional 22 asteroids with Yarkovsky-dominated drifts, ordered by decreasing value of Yarkovsky sensitivity. Symbols are as in Fig. 4.3. The observed rates for the majority of objects shown in this figure appear to exceed predicted values. This is a consequence of the SNR > 1 selection criterion which eliminates objects with lower da/dt values.

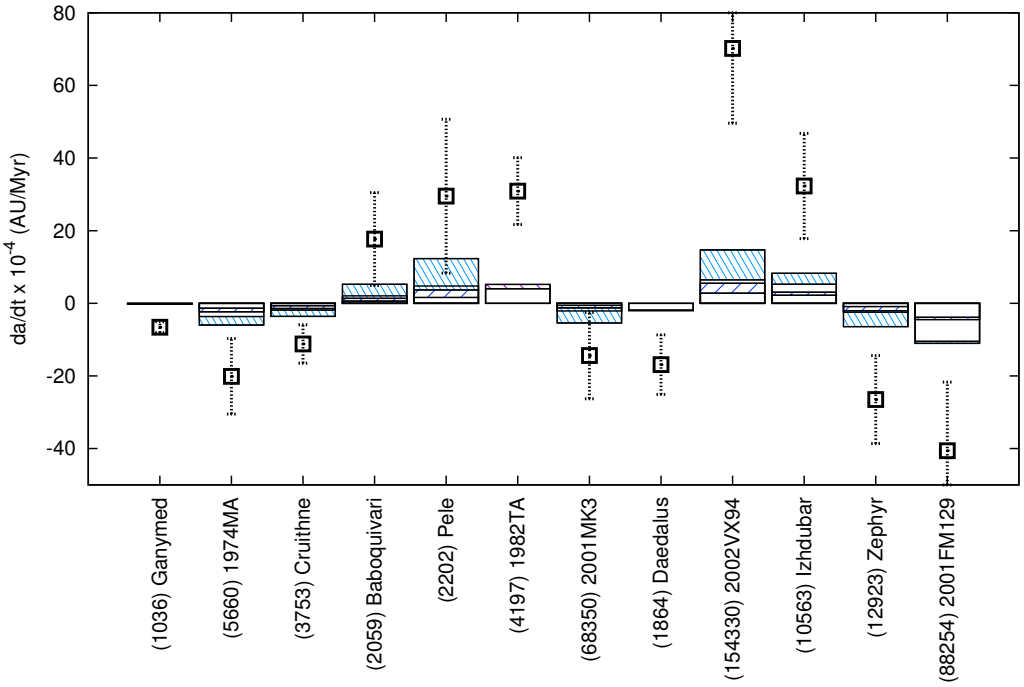

Figure 4.5 Measured and predicted drift values for 12 asteroids with possible Yarkovsky-dominated drifts, defined as objects with Yarkovsky efficiency f_Y exceeding 2 $\times 10^{-5}$. Symbols are as in Fig. 4.3. Most objects in this figure have measured drifts that lie outside of the range of values expected on the basis of Yarkovsky models. This could be due to inaccuracies in our knowledge of physical properties, faulty astrometry, or modeling errors.

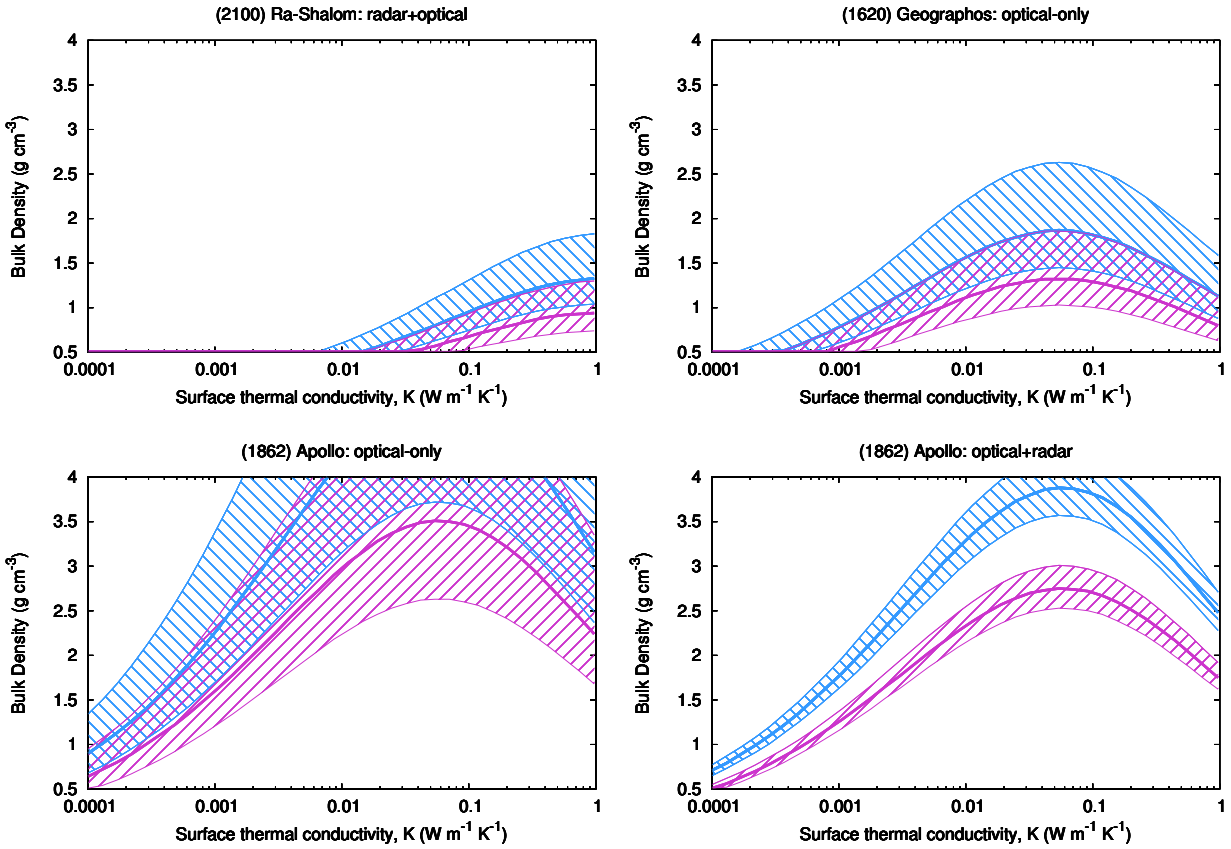

Figure 4.6 Range of bulk densities and thermal conductivities of three Yarkovsky-dominated asteroids consistent with their observed da/dt values. Blue (top) solid line corresponds to values consistent with best-fit da/dt and 180° obliquity, pink (lower) solid line corresponds to values consistent with best-fit da/dt and 135° obliquity. Dashed regions surrounding each solid line encompass the 1σ confidence limits on the corresponding da/dt determinations. Not all values displayed in this K-ρ space are necessarily appropriate for asteroids. Infrared observations suggest that (2100) Ra-Shalom has a thermal conductivity between 0.1 and 1 W m^{-1} K^{-1} (Delbó et al., 2003; Shepard et al., 2008), consistent with the range suggested by our Yarkovsky rate determination. For Apollo, we show results for both optical-only and radar+optical determinations. The inclusion of radar data greatly reduces the error bars on the measured drift, and therefore the area of the shaded curves.

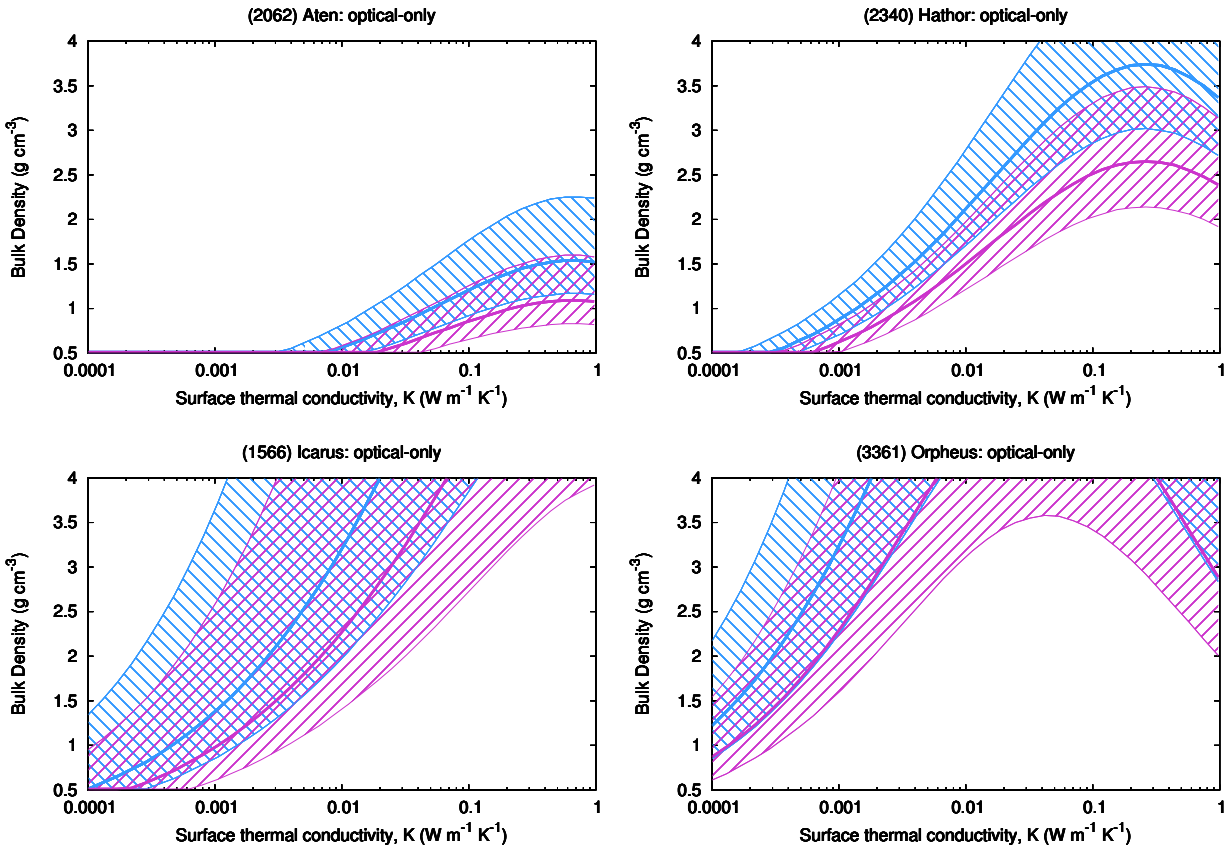

Figure 4.7 Companion to Fig. 4.6. Range of bulk densities and thermal conductivities of three Yarkovsky-dominated asteroids consistent with their observed da/dt values. For (2062) Aten and (2340) Hathor, blue (top) solid line corresponds to values consistent with best-fit da/dt and 180° obliquity, pink (lower) solid line corresponds to values consistent with best-fit da/dt and 135° obliquity. The constraints for (1566) Icarus suggest that it may have a lower obliquity than those assumed. (3361) Orpheus has a positive drift, so the blue (top) solid line corresponds to values consistent with best-fit da/dt and 0° obliquity, pink (lower) solid line corresponds to values consistent with best-fit da/dt and 45° obliquity. Dashed regions surrounding each solid line encompass the 1σ confidence limits on the corresponding da/dt determinations. Not all values displayed in this K-ρ space are necessarily appropriate for asteroids. A period of 4.5 hours was assumed for (2340) Hathor, and a 0.15 geometric albedo was assumed for (3361) Orpheus.

Table 4.3. Semi-major Axis Drift Rates

NEA		a (AU)	e	i (deg)	D (km)	P (h)	p_V	Arc	$(da/dt)_{\rm o}$ (10^{-4} AU/Myr)	1σ	$(da/dt)_{\rm r+o}$ (10^{-4} AU/Myr)	1σ	SNR	s_Y	f_Y $\times 10^{-5}$
(433)	Eros	1.46	0.22	10.83	16.84	5.270	0.25	1893-2012	-0.3	0.2	···	···	1.81	70.56	0.38
(152563)	1992 BF	0.91	0.27	7.25	0.42†	···	···	1992-2011	-11.6	1.0	···	···	11.26	40.28	0.37
(1862)	Apollo	1.47	0.56	6.35	1.50	3.065	0.25	1957-2012	-1.8	0.6	-2.3	0.2	11.50	36.11	0.23
(1685)	Toro	1.37	0.44	9.38	3.40	10.1995	0.31	1948-2010	-1.4	0.7	···	···	2.00	24.06	0.34
(2062)	Aten	0.97	0.18	18.93	1.10	40.77	0.26	1955-2012	-7.5	2.4	···	···	3.17	19.94	0.65
(1620)	Geographos	1.25	0.34	13.34	2.56	5.22204	0.3258	1951-2012	-2.4	0.7	-2.5	0.6	3.85	18.15	0.48
(2340)	Hathor	0.84	0.45	5.85	0.30	···	···	1976-2012	-14.5	3.5	···	···	4.11	15.32	0.31
(1580)	Betulia	2.20	0.49	52.11	5.80	6.1324	0.08	1950-2010	-1.4	2.0	-1.3	0.9	1.46	13.45	0.53
(3361)	Orpheus	1.21	0.32	2.69	0.30	3.58	···	1982-2009	5.7	2.5	···	···	2.25	13.04	0.13
(1566)	Icarus	1.08	0.83	22.83	1.00	2.273	0.51	1949-2009	-3.2	2.0	···	···	1.62	11.86	0.14
(2063)	Bacchus	1.08	0.35	9.43	1.35†	14.90	···	1977-2007	-4.2	3.3	···	···	1.26	10.58	0.42
(887)	Alinda	2.48	0.57	9.36	4.20	73.97	0.31	1918-2008	4.0	2.5	···	···	1.59	9.42	1.12
(1865)	Cerberus	1.08	0.47	16.10	1.20	6.810	0.22	1971-2008	-5.1	2.7	···	···	1.90	9.20	0.44
(161989)	Cacus	1.12	0.21	26.06	1.90	3.7538	0.09	1978-2010	2.6	2.3	···	···	1.12	8.94	0.39
(3757)	1982 XB	1.83	0.45	3.87	0.50	9.0046	0.18	1982-2008	-13.7	6.8	···	···	2.04	8.82	0.49
(6037)	1988 EG	1.27	0.50	3.50	0.65†	2.760	···	1988-2007	-14.2	4.3	···	···	3.34	8.51	0.64
(2102)	Tantalus	1.29	0.30	64.01	2.04†	2.391	···	1975-2008	-3.8	3.6	···	···	1.08	8.31	0.60
(2100)	Ra-Shalom	0.83	0.44	15.76	2.30	19.797	0.13	1975-2009	-4.8	2.2	-5.4	1.5	3.67	8.30	0.90
(207945)	1991 JW	1.04	0.12	8.71	0.52†	···	···	1955-2009	-6.2	4.3	···	···	1.42	8.00	0.26
(67399)	2000 PJ6	1.30	0.35	14.69	0.96†	···	···	1951-2009	-19.4	7.2	···	···	2.71	7.34	1.40
(1036)	Ganymed	2.66	0.53	26.70	31.66	10.31	0.2926	1924-2012	-6.6	1.5	···	···	4.41	7.28	14.23
(14402)	1991 DB	1.72	0.40	11.42	0.60	2.266	0.14	1991-2009	-5.0	4.3	···	···	1.19	7.05	0.22
(3908)	Nyx	1.93	0.46	2.18	1.00	4.42601	0.23	1980-2009	9.8	3.2	12.9	2.7	4.71	5.52	0.92
(4660)	Nereus	1.49	0.36	1.43	0.33	15.1	0.55	1981-2010	7.3	5.6	10.9	4.8	2.29	5.46	0.27

Table 4.3 (cont'd)

NEA		a (AU)	e	i (deg)	D (km)	P (h)	p_V	Arc	$(da/dt)_{\rm o}$ (10^{-4} AU/Myr)	1σ	$(da/dt)_{\rm r+o}$ (10^{-4} AU/Myr)	1σ	SNR	s_Y	f_Y $\times 10^{-5}$
(5660)	1974 MA	1.79	0.76	38.06	2.57†	17.5	···	1974-2005	-20.1	10.4	···	···	1.92	5.46	2.68
(10302)	1989 ML	1.27	0.14	4.38	0.45†	19.	···	1989-2006	35.3	7.1	···	···	4.96	5.33	1.26
(2061)	Anza	2.26	0.54	3.77	2.60	11.50	···	1960-2012	10.7	9.0	···	···	1.19	5.00	1.88
(22753)	1998 WT	1.22	0.57	3.20	1.02†	10.24	···	1955-2009	-5.4	5.0	-6.1	4.9	1.26	4.95	0.41
(3753)	Cruithne	1.00	0.51	19.81	3.39†	27.4	···	1973-2010	-11.2	5.3	···	···	2.12	4.84	2.61
(4769)	Castalia	1.06	0.48	8.89	1.40	4.095	···	1989-2011	-17.2	11.7	···	···	1.47	4.59	1.69
(4947)	Ninkasi	1.37	0.17	15.65	0.65†	···	···	1978-2009	13.4	10.3	···	···	1.30	4.23	0.69
(241596)	1998 XM2	1.80	0.34	27.10	1.41†	···	···	1952-2011	-14.4	10.7	···	···	1.35	4.23	1.53
(4034)	Vishnu	1.06	0.44	11.17	0.42	···	0.52	1986-2009	-13.8	12.1	···	···	1.14	3.72	0.42
(7336)	Saunders	2.31	0.48	7.17	0.65†	6.423	···	1982-2010	10.3	8.3	···	···	1.25	3.50	0.47
(2059)	Baboquivari	2.64	0.53	11.04	2.46†	···	···	1963-2009	17.7	12.8	···	···	1.38	3.42	2.96
(15745)	1991 PM5	1.72	0.25	14.42	0.98†	···	···	1982-2007	-13.2	9.0	···	···	1.46	3.39	1.00
(138911)	2001 AE2	1.35	0.08	1.66	0.56†	···	···	1984-2012	-22.9	11.2	···	···	2.04	3.38	1.02
(18109)	2000 NG11	1.88	0.37	0.81	1.12†	4.2534	···	1951-2005	12.0	9.6	···	···	1.25	3.21	1.00
(2202)	Pele	2.29	0.51	8.74	1.07†	···	···	1972-2008	29.5	21.2	···	···	1.39	2.98	2.18
(68950)	2002 QF15	1.06	0.34	25.16	2.03†	29.	···	1955-2008	-11.6	6.5	···	···	1.80	2.96	1.78
(4197)	1982 TA	2.30	0.77	12.57	1.80	3.5380	0.37	1954-2010	30.9	9.2	···	···	3.36	2.88	2.84
(3362)	Khufu	0.99	0.47	9.92	0.70	···	0.21	1984-2004	-20.4	13.2	···	···	1.54	2.87	1.01
(99935)	2002 AV4	1.65	0.64	12.76	2.46†	···	···	1955-2011	-9.8	8.0	···	···	1.23	2.73	1.48
(68350)	2001 MK3	1.67	0.25	29.56	2.43†	3.24	···	1955-2007	-14.4	11.9	···	···	1.21	2.61	2.73
(54690)	2001 EB	1.63	0.26	35.36	1.18†	···	···	1952-2009	-14.4	13.3	···	···	1.08	2.56	1.31
(4179)	Toutatis	2.53	0.63	0.45	5.40	176.	···	1976-2011	-18.4	4.3	-5.0	0.6	8.33	2.44	1.68
(1864)	Daedalus	1.46	0.61	22.20	3.70	8.572	···	1971-2006	-16.9	8.2	···	···	2.06	2.44	3.97
(154330)	2002 VX94	1.48	0.41	7.16	0.90†	···	···	1986-2011	70.2	20.6	···	···	3.42	2.41	4.64

Table 4.3 (cont'd)

NEA		a (AU)	e	i (deg)	D (km)	P (h)	p_V	Arc	$(da/dt)_{\rm o}$ (10^{-4} AU/Myr)	1σ	$(da/dt)_{\rm r+o}$ (10^{-4} AU/Myr)	1σ	SNR	s_Y	f_Y $\times 10^{-5}$
(7753)	1988 XB	1.47	0.48	3.12	0.68†	···	···	1988-2012	18.9	12.9	···	···	1.46	2.39	0.90
(10563)	Izhdubar	1.01	0.27	63.46	1.48†	···	···	1991-2010	32.3	14.5	···	···	2.23	2.19	3.70
(13651)	1997 BR	1.34	0.31	17.25	1.07†	33.644	···	1980-2011	-12.4	11.8	···	···	1.06	2.18	1.02
(12923)	Zephyr	1.96	0.49	5.29	2.14†	3.891	···	1955-2012	-26.5	12.1	···	···	2.19	2.05	3.97
(3554)	Amun	0.97	0.28	23.36	2.48	2.530	0.1284	1986-2012	9.0	8.8	···	···	1.03	2.05	1.73
(88254)	2001 FM129	1.18	0.63	1.52	1.19†	···	···	1978-2008	-40.6	18.9	···	···	2.15	2.05	3.01

Orbital elements a, e, i are from the MPCORB database. Spin periods P and geometric albedos p_V are from the JPL Small-Body Database. Diameters D, when known, are from the same database, otherwise they are derived from the absolute magnitude with a $p_V = 0.14$ assumption and marked with †. Objects are listed in decreasing order of Yarkvosky sensitivity s_Y. Yarkosvky efficiencies f_Y are estimated for a bulk density $\rho = 1,200$ kg m^{-3}.

CHAPTER 5

Thermophysical Modeling

5.1 Introduction

We describe a new, detailed thermal model that combines the infrared flux measurements of near-Earth asteroid (29075) 1950 DA by the Wide-field Infrared Survey Explorer (WISE) spacecraft with the 2036- and 1016-facet models of its shape derived by Busch et al. (2007) from radar observations. This model constrains the best-fit thermal inertia for the body.

We have initiated a program of thermophysical modeling of asteroids detected by NEOWISE, beginning with the potentially hazardous asteroid (29075) 1950 DA. Potentially hazardous asteroids are a subset of near-Earth asteroids (NEAs) whose orbits come within 0.05 AU of Earth's orbit and have an absolute magnitude of 22.0 or less. 1950 DA was previously observed through the Ondřejov Asteroid Photometry Project (Pravec, 2013). These observations constrained its period and measured H and G of the object. Work by Rivkin et al. (2005) determined it had an albedo of ≤ 0.25.

This object was observed by the WISE spacecraft 16 times between 2010 July 12 and 2010 July 13. Two of these observations were unsuitable for use, as indicated by associated "qual_frame" flags. This study used 14 measurements in band W3 with an average signal-to-noise ratio (SNR) of ~ 7 (see Table 5.1). The corresponding detections in W4 were marginal and did not further constrain the results from the W3 analysis (see Section 5.2.5). The asteroid was not reliably detected in bands W1 or W2.

Data were extracted from the WISE All-Sky Single Exposure (Level 1b) source table following the methods described in Mainzer et al. (2011a). This data are from "second pass"

Table 5.1 NEOWISE observations of 1950 DA. Times are in Modified Julian Date (MJD). The distance between the asteroid and sun is R_{helio}, Δ is the distance between the asteroid and the WISE spacecraft. Mag is observed W3 magnitudes, with their 1σ errors.

reference stars. 10 seconds

Time (MJD)	R_{helio} (AU)	Δ (AU)	Phase angle (degrees)	Mag $\pm 1\sigma$
55389.8521	1.73889	1.40926	35.77	9.64 ± 0.12
55389.9844	1.73975	1.40856	35.75	9.371 ± 0.099
55390.1167	1.74062	1.40786	35.73	9.519 ± 0.119
55390.1828	1.74105	1.40780	35.72	9.927 ± 0.148
55390.2489	1.74148	1.40715	35.71	10.097 ± 0.188
55390.2490	1.74148	1.40715	35.71	9.901 ± 0.156
55390.3151	1.74191	1.40680	35.70	9.762 ± 0.134
55390.3812	1.74234	1.40645	35.69	9.859 ± 0.146
55390.5135	1.74320	1.40575	35.67	9.919 ± 0.151
55390.5797	1.74364	1.40539	35.66	9.551 ± 0.109
55390.7120	1.74450	1.40469	35.63	9.824 ± 0.145
55390.8443	1.74536	1.40398	35.61	9.521 ± 0.11
55390.9765	1.74622	1.40327	35.59	9.984 ± 0.171
55390.9766	1.74622	1.40327	35.59	9.789 ± 0.136

processing (as described in (Cutri et al., 2012)), and used different flat and dark frames than the preliminary data reported in Mainzer et al. (2011b). The single-frame images were visually inspected and compared to the WISE All-Sky Release images, which contain coadds of all exposures at a given location and are consequently much more sensitive to inertially-fixed (on the timescale of the observations) sources such as stars and galaxies (Cutri et al., 2012). Furthermore, asteroid catalog positions from the single-frame images were compared to sources extracted from the coadded source catalog to ensure that detections were free from confusion with inertial sources. Detections were considered when the photometric quality flag values (ph_qual) were either A, B, or C, indicating a detection with SNR > 2, and when the contamination and confusion flag values (cc_flags) indicated that the detections were not spurious values caused by artifacts.

Table 5.2 Pole direction, rotation period, and diameter of equal-volume sphere of radar shape models of 1950 DA (Busch et al., 2007).

Quantity	Prograde model	Retrograde model	Error
Ecliptic pole direction (λ,β)	(88.6°,77.7°)	(187.4°,−89.5°)	±5°
Diameter of equal-volume sphere (km)	1.16	1.30	±10%
Rotation period (h)	2.12160		±0.00004

5.1.1 Radar observations

Radar measurements of 1950 DA were obtained in 2001, when the object passed within 0.05 AU of Earth. These measurements indicated that this object had a small probability of impacting the earth in the year 2880 (Giorgini et al., 2002). The major source of uncertainty in this trajectory prediction is linked to the unknown strength of the Yarkovsky effect on this object. The object's shape was derived from these radar data by Busch et al. (2007), which produced two distinct possible shape models– one a prograde rotator, the other retrograde. Each model has an associated diameter and spin pole direction, values of which are reproduced in Table 5.2. A retrograde spin would yield a Yarkovsky drift away from the sun, precluding a 2880 Earth impact by this object. However, if this object is found to be spinning in a prograde direction, an impact is still possible.

5.2 Methods

We present a detailed thermophysical model of 1950 DA that combines the shape models of Busch et al. (2007) with the 14 W3 observations by NEOWISE. This model is based on the work of Spencer et al. (1989), which allows conduction of heat into and out of the surface via a series of slabs. Heat is not conducted laterally between facets, an approximation that is justified given that each facet is $\sim$ 1000 m^2 in area, much larger than the model's skin depth l_s which is at maximum $\sim$ 1 m and can be as small as $\sim 10^{-3}$ m. The constraints of shape and spin state from the radar shape model allow us to fit for thermal conductivity, diameter, and initial rotation phase.

5.2.1 Assumptions

We build on the thermal modeling foundation described in Spencer et al. (1989), which makes several assumptions. The possible subsurface penetration of sunlight is neglected. Thermal conductivity K and heat capacity C_p are assumed to be temperature-independent and uniform throughout the body. While radiation between grains has been shown to be important for porous media such as lunar regolith, asteroid regolith is less well-studied. However, if lunar regolith was used as a proxy, results from Jones et al. (1975) indicate that the radiative component would increase K by less than an order of magnitude, and therefore would not substantively change our result.

Although albedo variations across the surface of an asteroid could result in nonuniform surface heating, albedo variations are considered to be negligible for this object. The largest observed albedo variations (from 0.10 to 0.67) on an asteroid are observed on (4) Vesta by the DAWN spacecraft (Reddy et al., 2012), but the spatial scale of these variations (of order $\sim$10 km) were small relative to the asteroid's size. Additionally, albedo variations on Vesta may be expected due to its large size and thermal/collisional history. Spacecraft images of other asteroids have revealed $\sim$ 10% albedo variations to be more typical (Helfenstein et al., 1996; Abe et al., 2006), consistent with the conclusions of Lebofsky et al. (1988) that lightcurve amplitudes are mainly due to shape and not albedo variations. However, thermal conductivity values are expected to span orders of magnitude, so the effect of albedo variations across the surfaces of the asteroids are assumed to be negligible for 1950 DA.

As mentioned in Section 1.4, many thermophysical studies employ a beaming parameter or artificial craters to simulate surface roughness on spherical models. Our model described in this chapter does not employ such a parameter or the addition of craters. The radar-derived shape models used here are significantly more complex than spherical models, and they inherently allow for nonuniform beaming with phase angle. Comparisons between highly symmetric faceted models and the radar-based shape models showed improvements in fits when using radar-based shape models. For the best-fit thermal conductivity, a 32-facet shape

model has a SSR six times as large as the radar-based prograde shape model. Observations of 1950 DA by WISE were taken at a phase angle (sun-object-observer angle) of 35°, so we would not expect to observe the beaming that has been observed at low phase angles and is attributed to roughness on a smaller scale than our model's facets. Note that the best fit to WISE data by Mainzer et al. (2011b) with the NEATM gave a beaming parameter $\eta = 2.51 \pm 0.39$. In Mainzer et al. (2011c), it was shown that η is correlated with phase angle, building upon the work of Wolters et al. (2008) and Harris (2006).

The model uses the values for diameter, spin pole, and rotation rate derived by Busch et al. (2007). As the uncertainty on the rotation rate is small ($\pm$0.144 s) relative to our 15 s time step, this uncertainty does not contribute significantly to the total error. That time step was chosen because it minimized computing time while still allowing for values of K as low as 0.001 W m^{-1} K^{-1} to be considered.

This study varied the thermal conductivity K, while density was held constant at 2500 kg m^{-3}, and heat capacity was held constant at 500 J kg^{-1} K^{-1}, values comparable to those of meteorites (Opeil et al., 2010). The heat transfer equations (see Section 5.2.3) incorporate these three parameters in both thermal inertia and skin depth. While we cannot avoid the degeneracy between these parameters, thermal conductivity is taken to be the principal variable quantity, as reasonable values can vary over five orders of magnitude. Experiments with combinations of K (0.01 or 0.001), ρ (1000,3000) and C_p (500,1000) confirmed this behavior. For ease of comparison to other studies, we report both the fitted value of K and the equivalent values of Γ and Θ in Table 5.3.

5.2.2 Calculation of sun and observer vectors

The location of the WISE spacecraft and the Sun relative to 1950 DA were calculated from the asteroid's well-known orbit by the software suite developed for the NEOWISE mission. Instead of tilting the 1000+ facet shape models to the appropriate spin orientation, and continuously rotating the model over the time steps of a full rotation, we found it

computationally efficient to instead tilt the sun and observer vectors relative to the modeled shape, and then rotate those vectors around the stationary faceted model. We employ a asteroid-centric cartesian coordinate system, with the spin axis aligned with the z-axis. For each time step the sun and observer are rotated according to this reference system to simulate rotation of the body.

5.2.3 Modeling of heat transfer

Following Spencer et al. (1989), each facet of the radar shape model is divided into 32 slabs with thickness δX that link the surface temperature to the asteroid's core temperature. As $\delta X = x/l_s$, and we used $\delta X = 0.25$, we model the region $8l_s$ below the surface. The new temperature of a given slab ($T(X, t + \delta t)$) depends on the temperature at the previous time step (t) of its neighboring slabs as described in Equation (16) of Spencer et al. (1989), which is

$$T(X, t + \delta t) = T(X, t) + \left(\frac{\delta t}{(\delta X)^2 t_R}\right)(T(X + \delta X, t) - 2T(X, t) + T(X - \delta X, t)) \quad (5.1)$$

The unitless factor t_R is defined as $t_R = \frac{\Gamma}{\sqrt{\omega}\epsilon\sigma T_s^3}$, where ω is the rotation frequency, ϵ is the emissivity, σ is the Stefan-Boltzmann constant, and T_s is the surface temperature. We found that the combination of $\delta X = 0.25$, and 500 time steps per rotation of the object, for a $\delta t = 15$ s provided good stability over a range of K values.

Surface temperature is then given by Equation 17 in Spencer et al. (1989),

$$T(0, t+\delta t) = T(0, t)+2\left(\frac{\delta t\omega}{\delta X^2}\right)(T(\delta X, t)-T(0, t))-2\left(\frac{\delta t\sqrt{\omega}}{\Gamma\delta X}\right)(\epsilon\sigma T^4(0, t)-(1-A)F_s(t)) \quad (5.2)$$

where A is the bolometric albedo and F_s is the time-dependent flux of incident solar radiation.

We assume the asteroid's core is at equilibrium, and find the core temperature by bal-

ancing the power received by the object with the power emitted

$$\frac{4S_*}{R_{helio}^2}(1-A) = \sigma T_{core}^4 \tag{5.3}$$

here S_* is the solar flux at 1 AU, R_{helio} is the asteroid's heliocentric distance in AU, A is the object's Bond albedo, and σ is the Stefan-Boltzmann constant. The object's Bond albedo was derived from its geometric albedo p_V, which in turn depends on its absolute H magnitude of $H = 18 \pm 0.3$ mag, phase curve slope G (taken to be 0.15 ± 0.10), and effective spherical diameter; all of these values were varied according to their error bars. The relationship used between A and p_v is $A = p_v(0.29 + 0.684G)$, as given in Bowell et al. (1989).

This method of determining core temperature was compared to the more computationally intensive warm-up cycle described in Spencer et al. (1989), and found to be consistent within 1 K. This method of core temperature determination was chosen because it allows for values of $K > 10$ W m^{-1} K^{-1} to be explored. These values were relevant for 1950 DA, as it had been suggested this object may have a metal-rich composition (Busch et al., 2007). The method of iteratively setting core temperature equal to the average surface temperature was found to be unsuitable for $K > 10$ W m^{-1} K^{-1}, as the surface quickly equilibrated to the initial core temperature, and therefore a convergence of final core temperatures was not achieved over a range of initial core temperatures.

The model undergoes several full rotation cycles until the surface temperature stabilizes, which is defined by the average surface temperature at a given phase of rotation being within 0.1 K of the average surface temperature at the same phase during the previous rotation cycle. Surface temperature stabilized after as few as 2 rotations for runs with low values of K to > 50 for very high values of K. Monte Carlo trial runs with low values of K lead surface temperatures to respond quickly to incident sunlight, and so equilibrium is quickly reached. Runs with high K result in a surface that strongly interacts with the core, requiring more iterations before equilibrium is achieved.

5.2.4 Modeled flux

Temperature is determined as a function of time for each facet, and the intensity of radiation emitted from a single facet at each wavelength band is determined from its temperature using Planck's law:

$$I_\lambda = \frac{2hc^2}{\lambda^5} \frac{1}{e^{\frac{hc}{\lambda k_B T}} - 1} \tag{5.4}$$

Here h is the Planck constant, c is the speed of light, and k_B is the Boltzmann constant. Emission is assumed to be a blackbody for each facet. Numerous studies of asteroids in the IR have shown that this approximation is accurate.

The spectral flux from each facet depends on the facet's area A, the cosine of the angle between the facet normal and the vector between the asteroid and the observer ($cos\theta$), and the distance d between the observer and the asteroid.

$$F_\lambda = \frac{I_\lambda A}{d^2} \max(\cos\theta, 0) \tag{5.5}$$

Total observed flux at a given time step is then computed by integrating the radiation emitted by each facet visible to the observer. A color correction factor is applied to the total observed flux (Wright et al., 2010; Mainzer et al., 2011a) to correct for the difference between stellar spectral energy distributions used in the determination of the WISE zero point magnitudes and cooler objects such as asteroids.

This modeled total flux due to thermal emission (F_m) is added to the calculated reflected flux (F_r) from the sun in the same wavelength (which we note is very small at these wavelengths), and is divided by the zero point flux (F_{zp}) for that band.

To calculate F_r, the intensity of the radiation form the sun I_s is computed using Equation 5.4, except in this case $T = 5778$ for the wavelength of interest. The flux from the sun F_s is computed from

$$F_s = \frac{4\pi I_s r_s^2}{4\pi d_s^2} \tag{5.6}$$

Here r_s^2 is the radius of the sun, and d_s is the distance from the sun. F_r is computed by

summing the flux from each facet following Equation 5.5 for each illuminated facet. This is then corrected by the phase angle, so that the facet illumination and the viewing angle of that facet by the observer are accounted for.

Apparent magnitude m is then computed via

$$m = -2.5\ log_{10}\left(\frac{F_m + F_r}{F_{zp}}\right) \tag{5.7}$$

5.2.5 Comparison to Observations

As the observations of 1950 DA span slightly more than one Earth day, there is negligible change in sun-object-observer geometry between observations. During the course of the observations, 1950 DA's distance from the sun did not change significantly ($\Delta r = 0.008$ AU, a difference that would lead to a core temperature change of ~ 0.5 K using Equation 5.3). Accordingly, observed flux is computed at 500 equally-spaced times over the final rotation to produce a modeled infrared lightcurve, which is then duplicated to cover the span of 1950 DA's observations.

The sum of squares of residuals (SSR) is the difference between the modeled flux and the observed flux, weighted by the error associated with the observed flux ($\sigma_{observed}$).

$$\text{SSR} = \sum_{i=0}^{n}\left(\frac{F_{i,observed} - F_{i,modeled}}{\sigma_{i,observed}}\right)^2 \tag{5.8}$$

This is computed for each observation i, and the thermal conductivity and phase associated with the fit with the lowest SSR is considered to be the best fit.

Observations of 1950 DA in band W4 were very faint, and close to the $\sim 7.0 - 7.5$ magnitude single-pass sensitivity limit. The average signal to noise of the W4 observations was $\sim 3\sigma$, and were not detected in 3 cases. The inclusion of these data in our fits had a negligible impact on the results and SSR.

5.2.6 Errors

Our Monte Carlo trials involved running the thermophysical model as the following measured parameters were varied by their reported error bars: uncertainties in the shape models' effective spherical diameter, uncertainties in their spin axis positions, and uncertainties in H and G values. The effect of these errors on the resulting derived thermophysical parameters were tested by comparing the model magnitudes to the observed magnitudes using the SSR.

The spin axis locations reported by Busch et al. (2007) had an associated uncertainty of $\pm 5^{\circ}$ (Table 5.2). We generated a list of dozens of spin axis locations centered around the best-fit spin axis location, with a Gaussian distribution such that 1σ of all tested spin axes were within 5°. We then re-ran the thermal model with these spin axes to determine their impact on the resulting fits. This impact was a $< 10\%$ change in SSR, which is minimal when compared to the errors introduced by the diameter uncertainty.

As there is a simple relationship between diameter and observed magnitude, it was unnecessary to run the full thermal model to determine the uncertainties due to diameter. A change in diameter ΔD would result in a change of facet area A in Equation 5.5. Therefore, total modeled flux F_m and the reflected flux F_r from the object are scaled as $D^2/(D+\Delta D)^2$, which gives the following new magnitude

$$m_{new} = m_{bestfit} - 5\ log_{10}\left(\frac{D}{D+\Delta D}\right) \tag{5.9}$$

5.3 Results

We modeled the thermophysical environment on the prograde and retrograde models of 1950 DA for K between 0.001 and 1000 W m^{-1} K^{-1}. Although we report our values in terms of K, to facilitate comparisons to other models, Table 5.3 gives the equivalent values of Γ and Θ for our models.

Temperature maps for $K = 0.001$, 0.01, and 0.1 W m^{-1} K^{-1} are shown in Figures 5.1,

Table 5.3 Equivalences between K, Γ and Θ for results in this chapter, assuming $\rho = 2500$ kg m $^{-3}$, and $C_p = 500$ J kg^{-1} K^{-1}

K	Γ	Θ
W m^{-1} K^{-1}	J s$^{-1/2}$ m^{-2} K^{-1}	
0.001	35	0.7
0.01	110	2.3
0.1	350	7.2
1	1100	22
10	3500	71
100	11000	226
1000	35000	716

5.2 and 5.3. These three cases represent the transition between a regime where low thermal inertia allows surface temperature to respond quickly to incident sunlight, evidenced by $\Theta < 1.0$ (Figures 5.1 and 5.2), to a body with a more uniform temperature (Figure 5.3). The low K bodies display sharp temperature changes across the terminator, and surface temperature reacts quickly to the amount of incident solar radiation. For these cases, total emitted flux is highly dependent on surface facet geometry, and the angle between a facet and the sun at any given time. As K increases and surface temperature becomes more uniform, total emitted flux depends less on surface topography and more on the observed-cross section of the object. This transition can be seen in Figure 5.4.

Thermal infrared lightcurves generally have lower amplitudes than lightcurves collected in wavelengths dominated by reflected sunlight for the same body, as they are less subject to phase effects (one is generally able to detect more flux from the nightside and shadowed areas in thermal emission than reflected sunlight). Over a single rotation, the observer is viewing from a fixed phase angle, equivalent to the same local time of day on the surface. The temperature at that same local time of day has few variations, resulting in only small changes in emitted flux, as seen in Figure 5.4. Another example of this behavior can be seen in the observations of (1865 Cerebus) in Figure 10 of Mainzer et al. (2011c). However, infrared lightcurves are still subject to shape effects.

Comparison between modeled lightcurves and NEOWISE observations is shown in Figure

5.5. The retrograde model with a 60° rotation phase and a 1.5 km diameter gives the best fit to observations, with an SSR=31.3. Our best-fit diameters give modeled lightcurves that match twelve (prograde) and thirteen (retrograde) observations to within 2σ. Visually, the retrograde model appears to offer a superior match to data than the prograde model, however, this apparent improvement in fit is not statistically significant to 1σ.

Figure 5.6 shows the goodness of fit (measured by SSR) as a function of given model K and diameter. Best fits are obtained for diameters larger than diameter associated with the radar shape models and K$<$ 0.01 W m^{-1} K^{-1}.

We set an upper bound of $K < 0.01$ W m^{-1} K^{-1} for this object, consistent with other measurements of K on NEAs. These values are also consistent with measured thermal inertias of powdered rock and lunar regolith, and inconsistent with the thermal inertias of bare rock or metal. We therefore infer that this body has some surface regolith or contains fractured rock. Combining this K range with the bulk density bounds (which assumed the asteroid is strengthless) given in Busch et al. (2007), we produced a revised estimate of modeled diurnal Yarkovsky drift following the procedure in Nugent et al. (2012a), which gives a value of $(1.74 \pm 0.21) \times 10^{-4}$ AU Myr^{-1}.

This range of K could be further constrained with thermal infrared observations at an additional epoch that observed the asteroid at a different phase angle. As seen in Figures 5.1 and 5.2, although the sunlight sides of models with $K = 0.001$ and 0.01 W m^{-1} K^{-1} display a similar temperature range, the nightsides vary by ~ 55 K. Therefore, new observations at a phase angle $> 60°$ would provide improved constraints on K.

5.4 Conclusions

We present a thermophysical model that combines detailed radar shape measurements and thermal observations from NEOWISE. We are able to constrain this object's $K < 0.01$ W m^{-1} K^{-1}, indicating that the surface of this body is not solid rock. This corresponds to $\Gamma = 110$ J m^{-2} s$^{-0.5}$ K^{-1}.

Future observations of 1950 DA would allow for a more constrained fit of K. Additionally, we are in the process of applying this thermophysical model to the other objects observed by NEOWISE that have well- constrained shapes and rotational states, in order to expand our understanding of the thermal properties of asteroids.

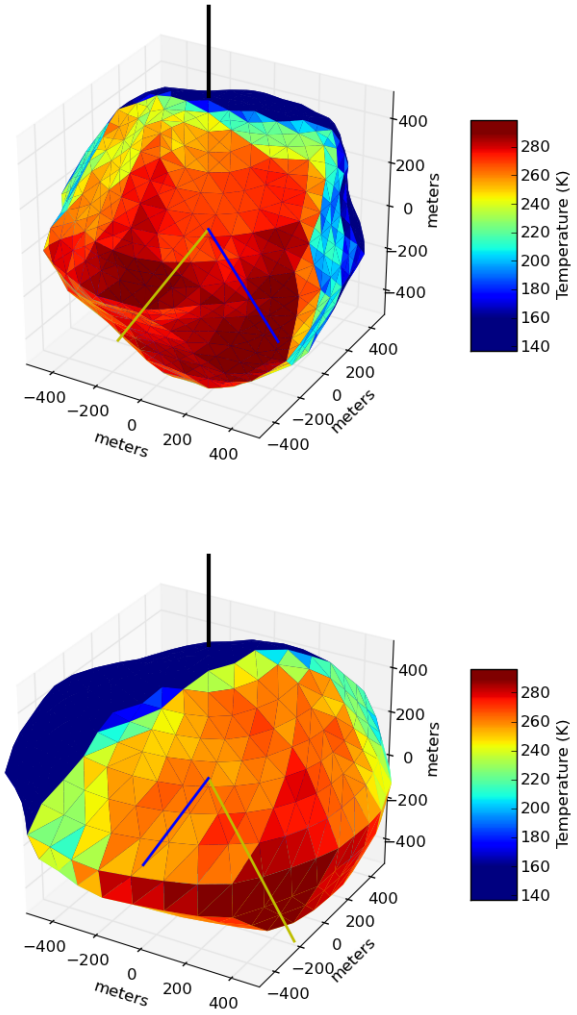

Figure 5.1 Prograde (top) and retrograde (bottom) shape models for $K = 0.001$ W m^{-1} K^{-1} (for equivalent Γ and Θ values, see Table 5.3). Coordinate system is in the frame of reference of the asteroid: black line is the object's spin axis (positive angular momentum), yellow line is direction to the Sun, blue line is direction to the observer. Colors correspond to temperature in K, see legend for scale. Due to this object's low thermal inertia, temperature drops off sharply across the terminator, and surface temperatures are dictated by current incident solar radiation.

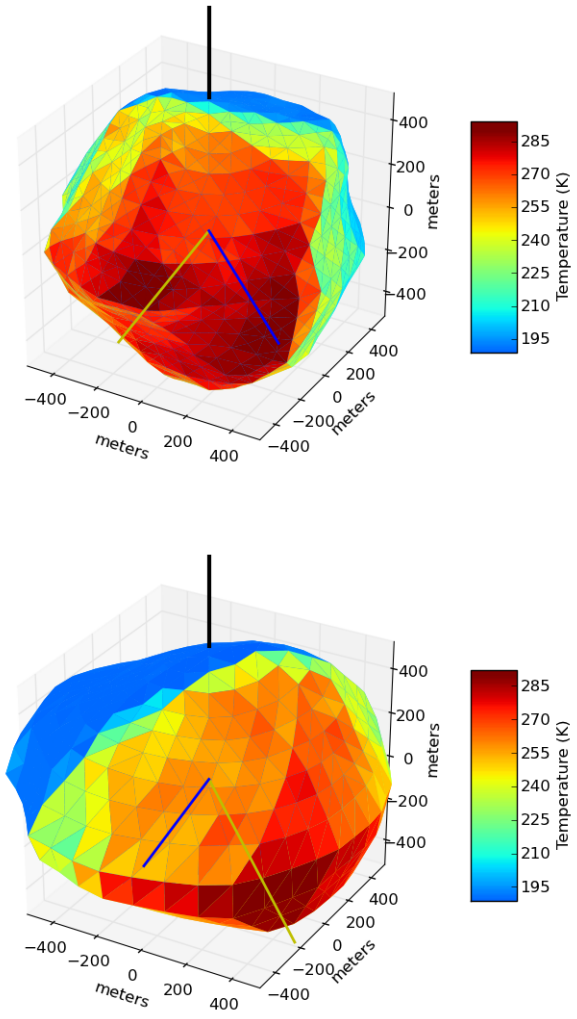

Figure 5.2 Companion to Figure 5.1: prograde (top) and retrograde (bottom) shape models for $K = 0.01$ W m^{-1} K^{-1}, an order of magnitude increase from the case in Figure 5.1. Definition of the lines is the same as in Figure 5.1. Particularly noticeable in the retrograde model is a thermal lag– the hottest portion of the surface is behind the sun-object vector (yellow). Although there still exists a sharp change in temperature across the terminator, the night side of this model is ~ 55 K warmer.

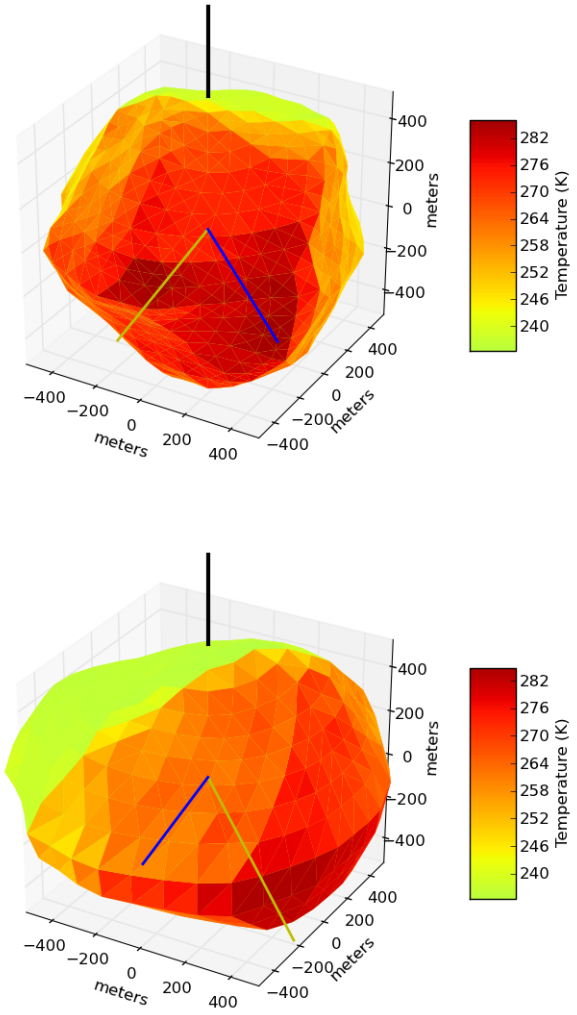

Figure 5.3 Companion to Figures 5.1 and 5.2: prograde (top) and retrograde (bottom) shape models for $K = 0.1$ W m^{-1} K^{-1}, an order of magnitude increase from the case in Figure 5.2. Here the model begins to transition away from the regime of temperature quickly adjusting with incident sunlight, as this object's higher thermal inertia allows for a relatively warmer night side.

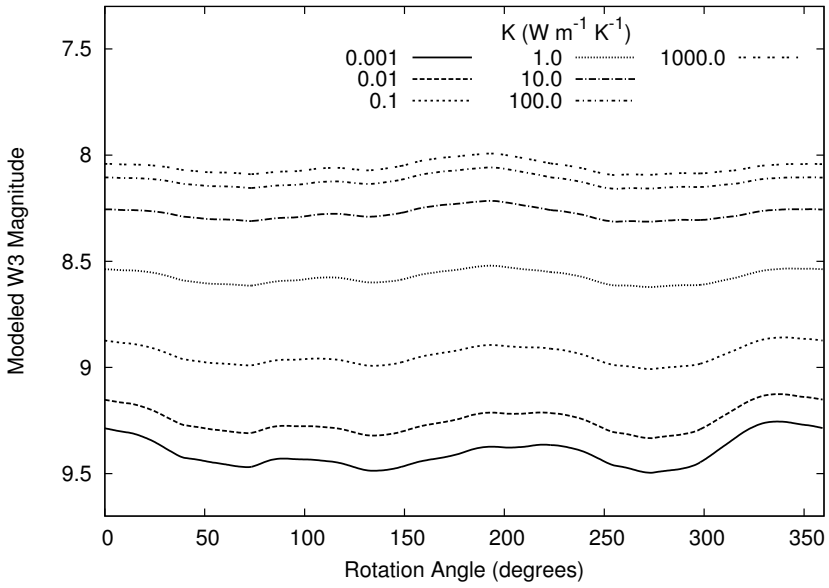

Figure 5.4 Modeled lightcurves in W3 band for the retrograde shape model of 1950 DA. Generally, higher thermal conductivity leads to a brighter observed magnitude, due to more uniform surface temperature. Low thermal conductivities result in extreme temperature variations across the surface, and resulting magnitudes are sensitive to surface geometry and display higher amplitudes. As thermal conductivity exceeds $K = 10.0$ W m^{-1} K^{-1}, surface temperature becomes highly uniform, leading to modeled lightcurves of similar magnitudes with small amplitude. For these high K cases, amplitude variations are due to the changing cross-section of the object as viewed by the observer.

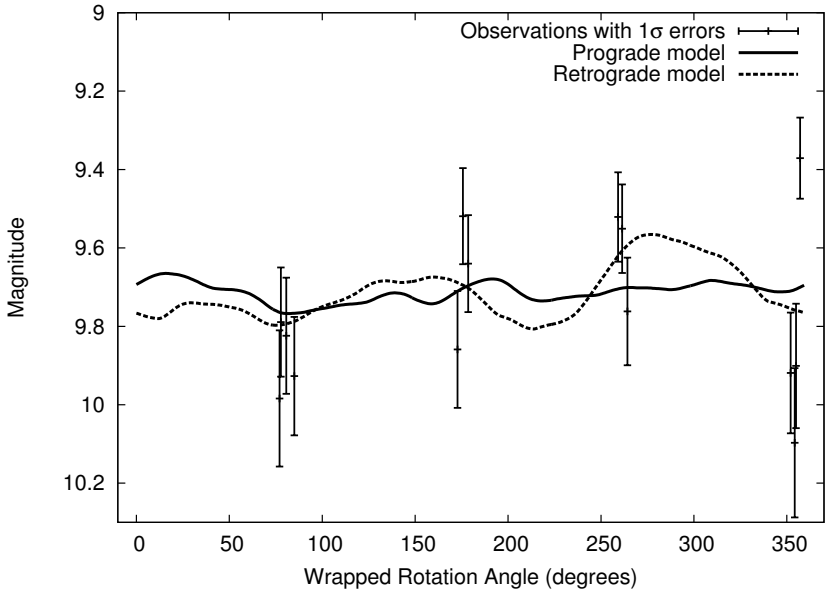

Figure 5.5 Comparison between observations and modeled flux for best-fit prograde model (solid curve) and best-fit retrograde model (dashed curve). The observations have been wrapped over one rotation period. The prograde model shown here represents $K = 0.001$ W m^{-1} K^{-1}, a 310° rotation phase and 1.31 km diameter. The retrograde model shown represents $K = 0.001$ W m^{-1} K^{-1}, a 60° rotation phase and a 1.5 km diameter. Visually, the retrograde model appears to offer a better fit than the prograde model. However, the improvement in fit offered by the retrograde model is not statistically significant.

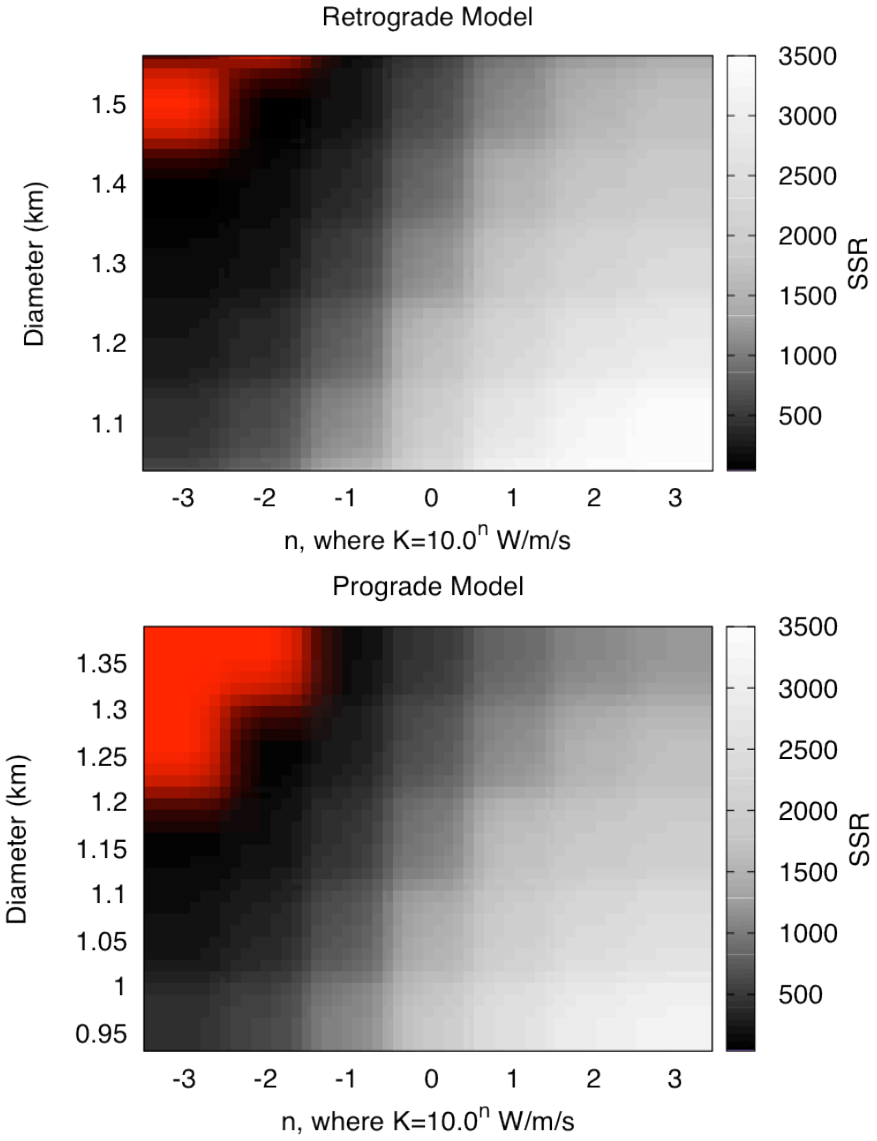

Figure 5.6 Fits of data as a function of K and diameter, prograde model (top) and retrograde model (bottom). Best fit region highlighted in red represents the 1σ boundary of errors as defined by chi square statistics. Both prograde and retrograde models show a best fit with K$<$ 0.01 W m^{-1} K^{-1} and a diameter larger than the quoted best fit diameter of the shape models, but within 2σ of that value.

CHAPTER 6

Concluding Remarks

This dissertation represents a new and original contribution to the study of NEAs. We increased the number of published predicted Yarkovsky drifts by an order of magnitude, increased the number of Yarkovsky detections by a factor of four, and developed new code to derive thermophysical parameters of asteroids.

The first chapter gave an introduction to near-Earth asteroids. Various types of data, including ground-based optical astrometry, radar observations, and space-based infrared observations, were discussed. The WISE mission and resulting data products was introduced. Radiation effects were described, with an emphasis on the diurnal Yarkovsky effect, which was examined in several later chapters of this dissertation. Finally, the history of thermophysical modeling was covered.

The second chapter of this dissertation described how a model of Yarkovsky drift was combined with measurements of albedo and diameter to predict Yarkovsky drift magnitudes for 540 NEAs. Upcoming apparitions of the 12 objects with the largest drifts were given, in an effort to encourage future observations of these objects and eventual Yarkovsky detections. Detections are estimated to be possible after 10 years of observations for most of these objects, unless radar observations over three epochs are obtained. Since the publication of the work discussed in this chapter, Robert McMillan of the Spacewatch project has added these 12 objects to their targeting scripts, ensuring that astrometry will be obtained by that facility if possible.

In the third chapter, we introduce a novel method for detecting semimajor axis drifts in asteroid astrometry. The fourth chapter describes the results of the application of this

method, which resulted in the detection of 54 drifts, 42 of which matched well with Yarkovsky predictions. This represents an increase in Yarkovsky measurements by an order of magnitude. Several consequences of these findings were discussed, including constraints on physical properties, spin states and their relationship to the transfer of asteroids from main belt to near-Earth space, and the consequences these drifts may have on asteroid trajectory predictions. Several individual cases, such as (1862) Apollo, and (1036) Ganymed, were examined. We concluded with a discussion processes other than Yarkovsky that may cause semimajor axis drifts.

The fifth chapter describes a new thermophysical model, which was applied to the potentially hazardous object (29075) 1950 DA. This model combined a high-resolution radar-based shape model with fourteen observations of the object at 12 μm by the WISE spacecraft. This model allowed conduction of heat into and out of each facet of the asteroid's surface via a series of slabs that link the surface of the asteroid to its core. The constraints on diameter, spin state, and spin rate provided by the radar shape model allowed us to more precisely fit for thermal conductivity (K) and rotation phase. The observations were taken at a single phase angle, constraining K to less than 0.01 W m^{-1} K^{-1}. Using density = 2500 kg m^{-3}, and heat capacity C_p = 500 J kg^{-1} K^{-1}, this gives an upper limit of thermal inertia Γ = 110 J m^{-2} s$^{-0.5}$ K^{-1}, consistent with other measurements of thermal conductivity and inertia for near-Earth asteroids.

Future work on this thermophysical model will be completed by C. R. Nugent during her postdoctoral appointment via the NASA Postdoctoral Program. The thermophysical model will be expanded in scope, and applied to hundreds of objects with both shape models and NEOWISE thermal infrared measurements.

References

Abe, M., Takagi, Y., Kitazato, K., et al. 2006, Science, 312, 1334

Alvarez, L. W., Alvarez, W., Asaro, F., & Michel, H. V. 1980, Science, 208, 1095

Bottke, W. F., Morbidelli, A., Jedicke, R., et al. 2002a, Icarus, 156, 399

Bottke, Jr., W. F., Vokrouhlický, D., Rubincam, D. P., & Broz, M. 2002b, Asteroids III, 395

Bottke, Jr., W. F., Vokrouhlický, D., Rubincam, D. P., & Nesvorný, D. 2006, Annual Review of Earth and Planetary Sciences, 34, 157

Bowell, E., Hapke, B., Domingue, D., et al. 1989, in Asteroids II (The University of Arizona Press), 524–556

Brown, R. H. 1985, Icarus, 64, 53

Burbine, T. H., McCoy, T. J., Meibom, A., Gladman, B., & Keil, K. 2002, in Asteroids III, ed. W. F. Bottke, A. Cellino, P. Paolicchi, & R. P. Binzel (University of Arizona Press), 395–408

Busch, M. W., Giorgini, J. D., Ostro, S. J., et al. 2007, Icarus, 190, 608

Capaccioni, F., de Sanctis, M. C., Filacchione, G., et al. 2009, in EGU General Assembly Conference Abstracts, Vol. 11, EGU General Assembly Conference Abstracts, ed. D. N. Arabelos & C. C. Tscherning, 12214

Capria, M. T., Titus, T. N., Tosi, F., et al. 2011, AGU Fall Meeting Abstracts, B7

Chamberlin, A. B. 2008, Bulletin of the American Astronomical Society, 40

Chapman, C. R. 1993, Nature, 363, 492

Chesley, S., Ostro, S., Vokrouhlicky, D., et al. 2003, Science, 302, 1739

Chesley, S. R. 2006, Asteroids, Comets, and Meteors, 215

Chesley, S. R., Baer, J., & Monet, D. G. 2010, Icarus, 210, 158

Chesley, S. R. & Milani, A. 1999, in AAS/Division for Planetary Sciences Meeting Abstracts, Vol. 31, AAS/Division for Planetary Sciences Meeting Abstracts, 28.06

Chesley, S. R., Nolan, M. C., Farnocchia, D., et al. 2012, LPI Contributions, 1667, 6470

Chesley, S. R., Vokrouhlický, D., Ostro, S. J., et al. 2008, LPI Contributions, 1405, 8330

Coradini, A., Capaccioni, F., Erard, S., et al. 2011, Science, 334, 492

Cutri, R. M., Wright, E. L., Conrow, T., et al. 2012, Explanatory Supplement to the WISE All-Sky Data Release Products, Tech. rep.

Danby, J. M. A. 1992, Fundamentals of Celestial Mechanics (Willmann-Bell, Inc)

Delbó, M., dell'Oro, A., Harris, A. W., Mottola, S., & Mueller, M. 2007, Icarus, 190, 236

Delbó, M., Harris, A. W., Binzel, R. P., Pravec, P., & Davies, J. K. 2003, Icarus, 166, 116

Delbó, M., Ligori, S., Matter, A., Cellino, A., & Berthier, J. 2009, The Astrophysical Journal, 694, 1228

Delbó, M. & Tanga, P. 2009, Planetary and Space Science, 57, 259

Delsemme, A. H. 1982, in Comets, ed. L. L. Wilkening, 85–130

Emery, J. P., Kelley, M. S., Fernandez, Y. R., et al. 2012, in AAS/Division for Planetary Sciences Meeting Abstracts, Vol. 44, AAS/Division for Planetary Sciences Meeting Abstracts, #102.05

Emery, J. P., Sprague, A. L., Witteborn, F. C., et al. 1998, Icarus, 136, 104

Farquhar, R., Kawaguchi, J., Russell, C. T., et al. 2002, in Asteroids III, ed. W. F. Bottke, A. Cellino, P. Paolicchi, & R. P. Binzel (University of Arizona Press), 367–376

Giorgini, J., Ostro, S., Benner, L., et al. 2002, Science, 296, 132

Giorgini, J. D., Benner, L. A. M., Ostro, S. J., Nolan, M. C., & Busch, M. W. 2008, Icarus, 193, 1

Goldreich, P. & Sari, R. 2009, The Astrophysical Journal, 691, 54

Gordon, W. E. 1964, Science, 146, 26

Gulkis, S., Keihm, S., Kamp, L., et al. 2010, Planetary and Space Science, 58, 1077

Hansen, O. L. 1977, Icarus, 31, 456

Harris, A. 2008, Nature, 453, 1178

Harris, A. W. 1998, Icarus, 131, 291

Harris, A. W. 2006, in IAU Symposium, Vol. 229, Asteroids, Comets, Meteors, ed. L. Daniela, M. Sylvio Ferraz, & F. J. Angel, 449–463

Harris, A. W., Mueller, M., Delbó, M., & Bus, S. J. 2005, Icarus, 179, 95

—. 2007, Icarus, 188, 414

Helfenstein, P., Veverka, J., Thomas, P. C., et al. 1996, Icarus, 120, 48

Hildebrand, A. R., Penfield, G. T., Kring, D. A., et al. 1991, Geology, 19, 867

Horner, J., Müller, T. G., & Lykawka, P. S. 2012, Monthly Notices of the Royal Astronomical Society, 3018

Hsieh, H. H., Jewitt, D. C., & Fernández, Y. R. 2004, The Astronomical Journal, 127, 2997

Hütter, E. S. & Kömle, N. I. 2008, in 5th European Thermal-Sciences Conference, The Netherlands

Ishiguro, M., Sarugaku, Y., Ueno, M., et al. 2007, Icarus, 189, 169

Jedicke, R., Larsen, J., & Spahr, T. 2002, in Asteroids III, ed. W. F. Bottke, A. Cellino, P. Paolicchi, & R. P. Binzel (University of Arizona Press), 71–87

Jenniskens, P. 2008, Earth Moon and Planets, 102, 505

Jewitt, D. 2012, The Astronomical Journal, 143, 66

Jewitt, D. & Li, J. 2010, The Astronomical Journal, 140, 1519

Jewitt, D. & Matthews, H. 1999, The Astronomical Journal, 117, 1056

Jones, W. P., Watkins, J. R., & Calvert, T. A. 1975, Moon, 13, 475

Kaiser, N. 2004, in Society of Photo-Optical Instrumentation Engineers (SPIE) Conference Series, Vol. 5489, Society of Photo-Optical Instrumentation Engineers (SPIE) Conference Series, ed. J. M. Oschmann, Jr., 11–22

Kaula, W. M. 1966, Theory of satellite geodesy. Applications of satellites to geodesy

Kitazato, K., Yamamoto, Y., & Okada, T. 2008, in Bulletin of the American Astronomical Society, Vol. 40, AAS/Division for Planetary Sciences Meeting Abstracts #40, 436

Konopliv, A. S., Asmar, S. W., Folkner, W. M., et al. 2011, Icarus, 211, 401

Kubica, J., Denneau, L., Grav, T., et al. 2007, Icarus, 189, 151

La Spina, A., Paolicchi, P., Kryszczynska, A., & Pravec, P. 2004, Nature, 428, 400

Lagerros, J. S. V. 1996a, Astronomy and Astrophysics, 310, 1011

—. 1996b, Astronomy and Astrophysics, 315, 625

—. 1997, Astronomy and Astrophysics, 325, 1226

—. 1998, Astronomy and Astrophysics, 332, 1123

Larson, S. 2007, in Near Earth Objects, our Celestial Neighbors: Opportunity and Risk, Proceedings if IAU Symposium 236, ed. A. M. G. B. Valsecchi, D. Vokrouhlický (Cambridge University Press), 323–328

Lebofsky, L. A., Greenberg, R., Tedesco, E. F., & Veeder, G. J. 1988, Icarus, 75, 518

Lebofsky, L. A., Sykes, M. V., Tedesco, E. F., et al. 1986, Icarus, 68, 239

Levy, D. H., Shoemaker, E. M., & Shoemaker, C. S. 1995, Scientific American, 273, 85

Lim, L. F., Emery, J. P., Moskovitz, N. A., et al. 2012, in AAS/Division for Planetary Sciences Meeting Abstracts, Vol. 44, AAS/Division for Planetary Sciences Meeting Abstracts, #305.01

Mainzer, A., Bauer, J., Grav, T., et al. 2011a, The Astrophysical Journal, 731, 53

Mainzer, A., Grav, T., Bauer, J., et al. 2011b, The Astrophysical Journal, 743, 156

Mainzer, A., Grav, T., Masiero, J., et al. 2011c, The Astronomical Journal, 736

—. 2011d, The Astrophysical Journal Letters, 737, L9

Margot, J. L. & Giorgini, J. D. 2009a, Bulletin of the American Astronomical Society, 41, 882

Margot, J.-L. & Giorgini, J. D. 2009b, American Astronomical Society, IAU Symposium #261. Relativity in Fundamental Astronomy: Dynamics, Reference Frames, and Data Analysis 27 April - 1 May 2009 Virginia Beach, VA, USA, #7.01; Bulletin of the American Astronomical Society, Vol. 41, p.882, 261, 701

Margot, J. L., Nolan, M. C., Benner, L. A. M., et al. 2002, Science, 296, 1445

Masiero, J. R., Mainzer, A. K., Grav, T., et al. 2012, The Astrophysical Journal, 749, 104

Matter, A., Delbó, M., Ligori, S., Crouzet, N., & Tanga, P. 2011, Icarus, 215, 47

McMillan, R. S. 2007, in Near Earth Objects, our Celestial Neighbors: Opportunity and Risk, Proceedings if IAU Symposium 236, ed. A. M. G. B. Valsecchi, D. Vokrouhlický (Cambridge University Press), 329–340

Milani, A., Chesley, S. R., Sansaturio, M. E., et al. 2009, Icarus, 203, 460

Milani, A. & Gronchi, G. 2009, Theory of Orbit Determination (Cambridge University Press)

Morbidelli, A., Bottke, Jr., W. F., Froeschlé, C., & Michel, P. 2002, Asteroids III, 409

Morbidelli, A., Levison, H. F., Tsiganis, K., & Gomes, R. 2005, Nature, 435, 462

Morbidelli, A. & Vokrouhlický, D. 2003, Icarus, 163, 120

Müeller, T. G. & Lagerros, J. S. V. 1998, Astronomy and Astrophysics, 338, 340

Müller, T. G. 2002, Meteoritics and Planetary Science, 37, 1919

Müller, T. G., Sekiguchi, T., Kaasalainen, M., Abe, M., & Hasegawa, S. 2005, Astronomy and Astrophysics, 443, 347

Müller, T. G., Sterzik, M. F., Schütz, O., Pravec, P., & Siebenmorgen, R. 2004, Astronomy and Astrophysics, 424, 1075

Müller, T. G., Ďurech, J., Hasegawa, S., et al. 2011, Astronomy and Astrophysics, 525, A145

Nugent, C. R., Mainzer, A., Masiero, J., Grav, T., & Bauer, J. 2012a, The Astronomical Journal, 144, 75

Nugent, C. R., Margot, J. L., Chesley, S. R., & Vokrouhlický, D. 2012b, The Astronomical Journal, 144, 60

Okada, T., Yamamoto, Y., Inoue, T., et al. 2006, in Lunar and Planetary Inst. Technical Report, Vol. 37, 37th Annual Lunar and Planetary Science Conference, ed. S. Mackwell & E. Stansbery, 1965

Opeil, C., Consolmagno, G., & Britt, D. 2010, Icarus, 208, 449

O'Rourke, L., Müller, T., Valtchanov, I., et al. 2011, in EPSC-DPS Joint Meeting 2011, 1464

Ostro, S. J., Benner, L. A. M., Giorgini, J. D., et al. 2005, IAU Circular, 8627

Ostro, S. J. & Giorgini, J. D. 2003, in Mitigation of Hazardous Impacts due to Comets and Asteroids, ed. M. J. S. Belton, T. H. Morgan, N. H. Samarasinha, & D. K. Yeomans (Cambridge University Press), 527–544

Peebles, C. 2000, Asteroids: a history (Smithsonian Institution Press)

Pravdo, S. H., Rabinowitz, D. L., Helin, E. F., et al. 1999, The Astronomical Journal, 117, 1616

Pravec, P. 2013, Ondřejov Asteroid Photometry Project, http://www.asu.cas.cz/ ppravec/neo.html

Pravec, P. & Harris, A. 2000, Icarus, 148, 12

Pravec, P. & Harris, A. W. 2007, Icarus, 190, 250

Pravec, P. et al. 2006, Icarus, 181, 63

Press, W. H., Teukolsky, S. A., Vetterling, W. T., & Flannery, B. P. 1992, Numerical Recipes in C (2nd ed.): The Art of Scientific Computing (New York, NY, USA: Cambridge University Press)

Reddy, V., Nathues, A., Le Corre, L., et al. 2012, Science, 336, 700

Renzetti, N. A., Thompson, T. W., & Slade, M. A. 1988, in The Telecommunications and Data Acquisition Report, ed. E. C. Posner, 287–293

Rivkin, A. S., Binzel, R. P., & Bus, S. J. 2005, Icarus, 175, 175

Rozitis, B. & Green, S. F. 2011, Monthly Notices of the Royal Astronomical Society, 415, 2042

Rubincam, D. 1995, Journal of Geophysical Research, 100, 1585

Scheeres, D. J., Durda, D. D., & Geissler, P. E. 2002, Asteroids III, 527

Seares, F. H. 1930, Publications of the Astronomical Society of the Pacific, 42, 5

Sekanina, Z. 1976, Icarus, 27, 265

Shepard, M. K., Clark, B. E., Nolan, M. C., et al. 2008, Icarus, 193, 20

Sitarski, G. 1992, The Astronomical Journal, 104, 1226

—. 1998, Acta Astronomica, 48, 547

Spencer, J. R., Lebofsky, L. A., & Sykes, M. V. 1989, Icarus, 78, 337

Spitale, J. & Greenberg, R. 2001, Icarus, 149, 222

Stokes, G. H., Evans, J. B., Viggh, H. E. M., Shelly, F. C., & Pearce, E. C. 2000, Icarus, 148, 21

Taylor, P. A., Margot, J.-L., Vokrouhlický, D., et al. 2007, Science, 316, 274

Tedesco, E. F., Noah, P. V., Noah, M., & Price, S. D. 2002, The Astronomical Journal, 123, 1056

Turyshev, S. G., Toth, V. T., Ellis, J., & Markwardt, C. B. 2011, Physical Review Letters, 107, 081103

Vokrouhlický, D., Capek, D., Chesley, S., & Ostro, S. 2005, Icarus, 173, 166

Vokrouhlický, D., Chesley, S., & Milani, A. 2001, Celestial Mechanics & Dynamical Astronomy, 81, 149

Vokrouhlický, D., Chesley, S. R., & Matson, R. D. 2008, Astronomical Journal, 135, 2336

Vokrouhlický, D., Milani, A., & Chesley, S. R. 2000, Icarus, 148, 118

Wolters, S. D., Green, S. F., McBride, N., & Davies, J. K. 2008, Icarus, 193, 535

Wright, E. L. 2007, ArXiv Astrophysics e-prints

Wright, E. L., Eisenhardt, P. R. M., Mainzer, A. K., et al. 2010, The Astronomical Journal, 140, 1868

Yeomans, D. K. 1991, The Astronomical Journal, 101, 1920

Yeomans, D. K. 1992, The Astronomical Journal, 104, 1266

Ziolkowski, K. 1983, in Asteroids, Comets, and Meteors, ed. C.-I. Lagerkvist, H. Rickman, 171–174